Probing strongly correlated phases in moiré heterostructures with quantum twisting microscopes

Fabian Pichler

Submitted in partial fulfillment of the requirements for the degree of Master of Science in the program Theoretical and Mathematical Physics, jointly awarded by Ludwig-Maximilians-Universität München and Technische Universität München in cooperation with the Elitenetwork of Bavaria.

Supervisor:	Prof. Dr. Michael Knap
Second examiner:	Prof. Dr. Johannes Knolle
Submitted by:	Fabian Pichler
Submission date:	May 24, 2024

Abstract

Probing strongly correlated phases in moiré heterostructures with quantum twisting microscopes

Moiré heterostructures serve as a novel solid-state platform, hosting a wide range of strongly correlated quantum phases, including generalized Wigner crystals and quantum anomalous Hall states. Being challenging to probe in experiments, the theoretical understanding of these states remains incomplete despite extensive investigation. Here, we propose that the quantum twisting microscope, which provides direct access to the energy-momentum resolved spectrum of single-particle and collective excitations, can be used as a novel tool to improve our understanding of strongly correlated phases. To this end, we calculate the single-particle spectral function and the dynamical spin-structure factor for both a ferromagnetic and antiferromagnetic generalized Wigner crystal formed in fractionally filled moiré superlattices of transition metal dichalcogenide heterostructures. We demonstrate that magnetic order can be identified in these response functions. Furthermore, we analyze the response of the quantum twisting microscope in an external magnetic field and explore signatures of quantum phase transitions. We focus on the specific case of triangular moiré lattices at half filling, which have been proposed to host a topological phase transition between a chiral spin liquid and a 120-degree ordered state. Finally, we compute the single-particle and collective spectra of integer and fractional quantum anomalous Hall states. We show that the spectral function of fractional quantum anomalous Hall states contains clear signs of electron fractionalization. Our work demonstrates the potential for quantum twisting microscopes to characterize strongly correlated quantum phases in moiré heterostructures.

Contents

Chapter 1

Introduction

This thesis is, to a large extent, based on Ref. [1]

- *Probing magnetism in moiré heterostructures with quantum twisting microscopes.* **Fabian Pichler**, Wilhelm Kadow, Clemens Kuhlenkamp, Michael Knap. arXiv:2402.04311 (2024)

Text, figures, and structure have been modified for this thesis.

With the emergence of transition metal dichalcogenides (TMDs) heterostructures as a new, highly tunable solid-state platform, a multitude of strongly correlated quantum phases of matter, such as generalized Wigner crystals (GWC) [2–9] and quantum anomalous Hall states [10–17] have been observed. TMD bilayers form moiré superlattices when the two layers are twisted by a small twist angle with respect to each other or when there is an intrinsic lattice mismatch in hetero-bilayer structures. These moiré superlattices can effectively simulate extended Hubbard models or topologically nontrivial Kane-Mele models on a honeycomb or triangular lattice [18–24], which allows for the experimental realization of strongly correlated electron phases. Due to their large lattice constants on the order of ~ 10 nm, moiré materials allow for tuning through a wide range of fillings. We briefly overview key experiments that have detected strongly correlated phases relevant to this thesis. They can be grouped into two classes: generalized Wigner crystals and quantum anomalous Hall states.

1.1 Generalized Wigner crystals

Generalized Wigner crystals have been observed at several fractional fillings of moiré lattices [2–9]. These states are correlated insulators breaking the discrete translation symmetry of the moiré lattice. They form due to long-range interactions between electrons. Long-range interactions are relevant in moiré superlattices [25] because the Wannier orbitals of the electrons are less localized compared to atomic lattices, and the charge density is low [18, 19, 21, 22]. Although the charge order of the GWC states has been firmly established in experiments, their spin order remains an open question. This is due to competing contributions to the effective spin coupling, primarily consisting of antiferromagnetic superexchange and ferromagnetic direct exchange [25–31]. Current methods to probe magnetic order are mainly based on magneto-optical methods measuring the magnetic susceptibility, suggesting a weak antiferromagnetic coupling at half-filling [9, 20]. Moreover, in another sample, almost vanishing magnetic couplings have been found [32]. These experimental findings are in stark contrast to theoretical predictions, suggesting large ferromagnetic interactions [25, 29, 31].

1.2 Quantum anomalous Hall states

In contrast to the topologically trivial generalized Wigner crystals, quantum anomalous Hall states are correlated bulk insulators with nontrivial topology characterized by a quantized Hall conductivity. While conventional quantum Hall states require strong external magnetic fields, the quantum anomalous Hall states spontaneously break time-reversal symmetry and survive down to zero magnetic fields. This requires bands with nontrivial Chern numbers since the Hall conductivity is proportional to the Chern number of all filled bands [33]. As discussed in Sec. 1.4.2, moiré heterostructures offer a promising platform to realize a Kane-Mele model [19, 21, 23, 24]. Numerous theoretical studies, primarily relying on exact diagonalization, have found evidence for both integer and fractional anomalous quantum Hall states in TMD heterostructures [34–41]. Experimentally, both integer [10, 15–17] and fractional [11–14] quantum anomalous Hall states have been observed. Graphene-based heterostructures have also been shown to host quantum anomalous Hall states [42–45]. Furthermore, a quantum spin Hall effect has been detected [46, 47], sparking theoretical speculation about its nature, including the possibility of vortex spin liquids [48] or Halperin states [49]. At present, experimentally characterizing quantum anomalous Hall states relies on electronic compressibility measurements and magneto-optical spectroscopy techniques [11, 12, 15]. While direct transport measurements have been performed [10, 13, 14], they still pose a significant experimental challenge in TMD heterostructures.

1.3 Quantum twisting microscope

To gain deeper insight into generalized Wigner crystals and quantum anomalous Hall states in TMD heterostructures, novel experimental tools are required to complement existing techniques. To reliably determine the fate of spin order in GWCs, developing more direct experimental probes of quantum magnetism is crucial. One proposed method uses the Zeeman splitting in circularly polarized exciton Umklapp resonances to detect magnetic order [50, 51]. Using such exciton Umklapp resonances, signatures of Wigner crystals in TMDs have been detected [52, 53]. Another approach to characterize the magnetic states is to use spin-polarized scanning tunneling spectroscopy or noise magnetometry [54–56].

In this work, we propose that a Quantum Twisting Microscope (QTM) [57] can be used to distinguish between antiferromagnetic (AFM) and ferromagnetic (FM) spin order by measuring the energy and momentum resolved single-particle and collective-excitation spectrum. The QTM is designed for studying the dynamical response of two-dimensional moiré materials [57, 58]. Placing a layer of graphene on a capped pyramid on the edge of an atomic force microscope cantilever makes it possible to continuously twist two sheets of 2D materials with respect to each other, see Fig. 2.1a). By applying a voltage between the top layer on the cantilever and the bottom sample layer and measuring the tunneling current as a function of the relative twist angle between the two layers, one obtains the momentum-resolved single-particle spectral function of the sample [57]. This is a form of elastic tunneling spectroscopy. In this work, we show that the expected spectral function for the GWC is qualitatively different for antiferromagnetic (AFM) and ferromagnetic (FM) interactions. An even more striking difference between the AFM and FM state can be seen in the dynamical spin-structure factor, which is accessible using inelastic tunneling spectroscopy [58, 59]. For that, the original setup of the QTM has to be modified

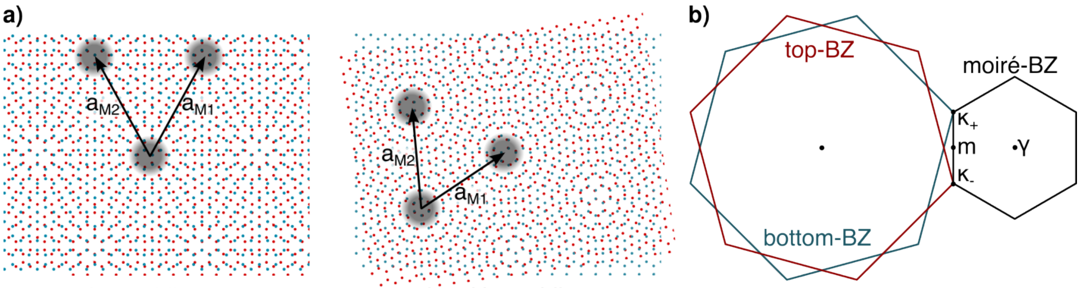

heterobilayer twisted homobilayer

FIGURE 1.1: **Moiré superlattice. a)** Left: TMD heterobilayer with zero twist angle forming a moiré superlattice due to a mismatch of the lattice constants of the two layers. Right: Moiré superlattice in a homobilayer due to a finite twist angle. The moiré lattice vectors $\mathbf{a}_{M_i}$ spanning a unit cell are highlighted. **b)** Twisting in real space also twists the Brillouin zones in momentum space. The corresponding smaller moiré Brillouin zone is also shown.

to a three-layer structure, with graphene contacts on both sides of the sample, see Fig. 2.4a). Applying a bias voltage between the graphene sheets, the spin response of the sample layer, which acts as a tunneling barrier, can be measured. Electrons tunneling from the top to the bottom layer interact with low-energy excitations of the sample layer, thus measuring its collective excitation spectrum. Using both elastic and inelastic tunneling spectroscopy to directly probe the momentum-resolved excitation spectrum of two-dimensional materials, such as TMD heterostructures, provides new insight into the strongly correlated states of these systems, not accessible using conventional optical measurements.

1.4 Moiré superlattices

Before proceeding to the main part of this work, we give a brief overview of moiré superlattices in bilayers of TMDs. A monolayer of TMD forms a honeycomb lattice, with transition metal atoms $\mathrm{M} \in \{\mathrm{W}, \mathrm{Mo}\}$ on one sublattice and chalcogen atoms $\mathrm{X} \in \{\mathrm{S}, \mathrm{Se}, \mathrm{Te}\}$ on the other sublattice. In contrast to graphene, another prominent two-dimensional material forming a honeycomb lattice, spin-orbit coupling in TMDs is strong, and the inversion symmetry $\mathcal{P} = \sigma^x$ of the lattice, acting on the sublattice degree of freedom, is broken since the two sublattices physically correspond to different atoms. Based on these symmetry considerations, the low-energy description of a TMD monolayer in the K valley is be given by [60]

$$H = at(k_x\sigma^x + k_y\sigma^y) + \frac{\Delta}{2}\sigma^z - \lambda_{\mathrm{SO}}\frac{\sigma^z - 1}{2}s^z \tag{1.1}$$

where the σ^α matrices act on the sublattice degree of freedom, while s^α act on spin. Here, a is the lattice constant of the TMD monolayer, and t is an effective hopping parameter. The low-energy Hamiltonian in the $K' = -K$ valley is given by the time reversal of Eq. (1.1). The mass term $\Delta \neq 0$ is allowed only due to inversion symmetry breaking, opening a gap at the K and K' points. The spin-orbit coupling λ_{SO} leads to spin splitting of the valence band, which is opposite in the two valleys. This implies that the spin and valley are locked at low energies, such that there is only one effective pseudospin degree of freedom.

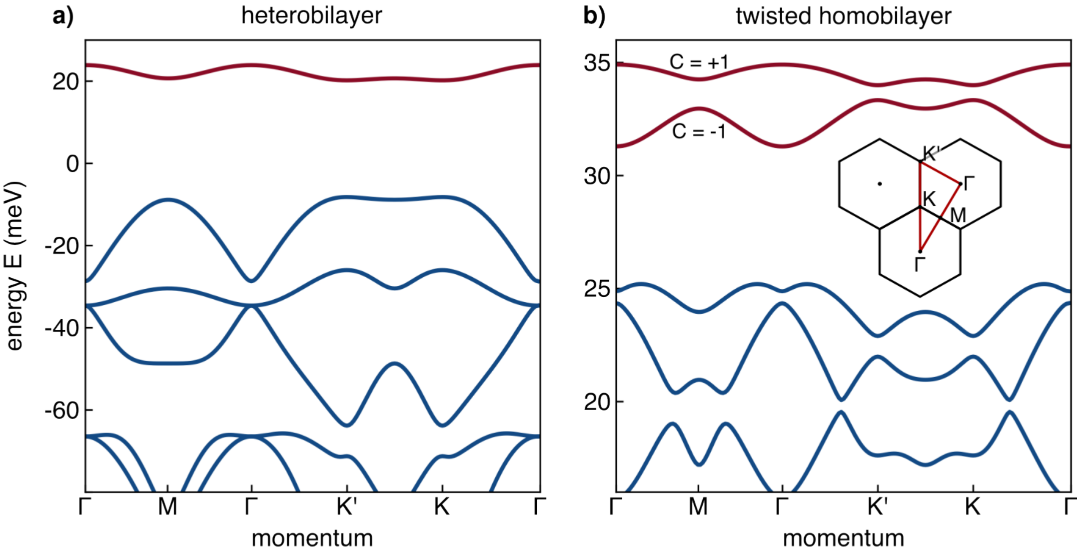

FIGURE 1.2: **Single-particle band structure from continuum model.** Topmost bands of holes in a moiré superlattice formed by a TMD **a)** heterobilayer **b)** twisted homobilayer ($\theta = 1^\circ$). In **a)**, the isolated band highlighted in red can be fitted to a tight-binding Hamiltonian, simulating Hubbard-model physics. In **b)**, the two topmost bands are topologically nontrivial, with Chern numbers $C = \pm 1$. They can be fitted to a Haldane-like model. The inset shows the chosen cut through the moiré Brillouin zone.

Consider two generically different monolayer TMDs stacked on top of each other with a relative twist angle θ. There will be regions in space where sites in different layers overlap, which we denote by XM, MX, MM, or XX, depending on which type of atom in the top overlaps with an atom in the bottom layer. Remarkably, these special points repeat periodically in space, thus forming a new lattice, dubbed a moiré lattice. If the two layers have lattice constants a_1 and a_2 and are twisted by an angle θ, then the moiré superlattice has a lattice constant [61]

$$a_M = \left(\frac{1}{a_1^2} + \frac{1}{a_2^2} - \frac{2\cos\theta}{a_1 a_2} \right)^{-1/2}. \tag{1.2}$$

For a heterobilayer with vanishing twist angle and a lattice mismatch $a_2 = (1-\delta)a_1$, this reduces to $a_M = a_2/\delta$. In a twisted homobilayer, one has $a_1 = a_2 = a$, in which case Eq. 1.2 simplifies to $a_M = a/\theta$ for small twist angles. We see that either a slight lattice mismatch or a small twist angle leads to a moiré lattice constant, which is orders of magnitude larger than the original atomic lattice constant. A visual example of this is shown in Fig. 1.1a). A larger lattice constant in real space leads to a smaller Brillouin zone in momentum space, as illustrated in Fig. 1.1b).

1.4.1 Hubbard model physics in heterobilayer

Holes in a TMD heterobilayer such as WSe_2/WS_2 simulate an extended Hubbard model on a triangular lattice [18, 20, 22]. This can be understood using the following considerations: The particles in the moiré lattice are attracted to the high-symmetry regions, where sites of the two layers overlap. This can be described by an effective moiré potential $\Delta(\mathbf{r})$ with minima at the aforementioned high symmetry points. Expanding in the reciprocal lattice vectors of the moiré lattice, the moiré potential can be expressed as

$$\Delta(\mathbf{r}) = \sum_{\mathbf{G}} V_{\mathbf{G}} e^{i\mathbf{G}\cdot\mathbf{r}}. \tag{1.3}$$

Restricting the sum to the first shell of reciprocal lattice vectors is already sufficient to model the moiré potential [18]. Demanding that $\Delta(\mathbf{r})$ must be real implies $V_{\mathbf{G}} = V^*_{-\mathbf{G}}$ and using the C_3 rotational symmetry of the TMD monolayer, we find the additional constraint $V_{\mathbf{G}_n} = V_{\mathbf{G}_{n+2}}$, where $\mathbf{G}_n = \mathrm{R}_{n\pi/3}\mathbf{G}_0$ and $\mathbf{G_0} = 4\pi/\sqrt{3}a_M(1,0)$. Here R_θ is a rotation matrix. Applying the constraint to Eq. (1.3), we get that $\Delta(\mathbf{r})$ is fully determined by two real parameters (V, ψ), such that $V_{\mathbf{G}_0} = Ve^{i\psi}$. These two parameters can be fit to ab initio calculations using density-functional theory [18].

Since we are working with a heterobilayer, the valence band of the top layer is shifted in energy relative to the valance band of the bottom layer. Consequently, in our low-energy description, only one layer is an active degree of freedom. The whole purpose of the inactive layer is that the particles in the active layer feel a moiré potential. Consequently, we can describe each valley on a single-particle level by a low-energy continuum model

$$\mathcal{H} = -\frac{\mathbf{k}^2}{2m^*} + \Delta(\mathbf{r}). \tag{1.4}$$

The large effective hole mass $m^* \sim m_e$, of the same order as the bare electron mass, leads to the quenching of the kinetic energy and the formation of flat bands. In Fig. 1.2a), the bandstructure resulting from Eq. (1.4) with parameters $(m^* = 0.35m_e, V = 8meV, \psi = 4\pi/9)$, adapted from Ref. [18], is shown. The topmost band is flat and isolated by a large gap from lower-lying bands. By constructing localized Wannier orbitals $W_{\mathbf{R}}(\mathbf{r})$, it can be fit to a tight binding Hamiltonian on a triangular lattice [18, 21]. An extended Hubbard model

$$H = \sum_{ij,\sigma}(t_{ij}c^\dagger_{\sigma i}c_{\sigma j} + \text{h.c.}) + U\sum_i n_{\uparrow i}n_{\downarrow i} + V\sum_{\substack{\langle ij\rangle \\ \sigma\sigma'}} n_{\sigma i}n_{\sigma' j} + X\sum_{\substack{\langle ij\rangle \\ \sigma\sigma'}} c^\dagger_{\sigma i}c^\dagger_{\sigma' j}c_{\sigma' i}c_{\sigma j} \tag{1.5}$$

is obtained by projecting the screened Coulomb interaction $V(\mathbf{r})$ onto Wannier orbitals. The parameters of the extended Hubbard model are given by

$$t_{ij} = \int d^2x\ W^*_{\mathbf{R}_i}(\mathbf{x})\mathcal{H}(\mathbf{x})W_{\mathbf{R}_j}(\mathbf{x}) \tag{1.6}$$

$$U = \int d^2x\ d^2y\ |W_{\mathbf{R}_i}(\mathbf{x})|^2 V(\mathbf{x}-\mathbf{y})|W_{\mathbf{R}_i}(\mathbf{y})|^2 \tag{1.7}$$

$$V = \int d^2x\ d^2y\ |W_{\mathbf{R}_i}(\mathbf{x})|^2 V(\mathbf{x}-\mathbf{y})|W_{\mathbf{R}_{i+1}}(\mathbf{y})|^2 \tag{1.8}$$

$$X = \int d^2x\ d^2y\ W^*_{\mathbf{R}_i}(\mathbf{x})W_{\mathbf{R}_{i+1}}(\mathbf{x})V(\mathbf{x}-\mathbf{y})W_{\mathbf{R}_i}(\mathbf{y})W^*_{\mathbf{R}_{i+1}}(\mathbf{y}). \tag{1.9}$$

We have included an on-site interaction U, nearest-neighbor interaction V, and a direct-exchange term X.

1.4.2 Topological bands in homobilayer

In twisted homobilayers, such as $MoTe_2$ or WSe_2, the valence bands of the top and bottom layers are at the same energy. Consequently, both layers are active, and we must include an additional layer-pseudospin degree of freedom. This can lead to the formation of topologically nontrivial bands [19, 23]. The single-particle continuum model for the K valley is given by

$$\mathcal{H} = \begin{pmatrix} -\frac{(\mathbf{k}-\boldsymbol{\kappa}_+)^2}{2m^*} + \Delta_\mathfrak{b}(\mathbf{r}) & \Delta_T(\mathbf{r}) \\ \Delta_T^\dagger(\mathbf{r}) & -\frac{(\mathbf{k}-\boldsymbol{\kappa}_-)^2}{2m^*} + \Delta_\mathfrak{t}(\mathbf{r}) \end{pmatrix} \tag{1.10}$$

with an layer $\ell \in \{\mathfrak{t} = -1, \mathfrak{b} = +1\}$ dependent moiré potential

$$\Delta_\ell(\mathbf{r}) = \sum_{n\in\{0,2,4\}} 2V\cos(\mathbf{G}_n \cdot \mathbf{r} + \ell\psi) \tag{1.11}$$

and interlayer hopping term

$$\Delta_T(\mathbf{r}) = w(1 + e^{-i\mathbf{G}_1\cdot\mathbf{r}} + e^{-i\mathbf{G}_2\cdot\mathbf{r}}) \tag{1.12}$$

whose form is a consequence of symmetry considerations of the lattice [19, 62]. Since the model Eq. (1.10) describes a homobilayer, the amplitude of the moiré potential (1.11) is the same in both layers. The bandstructure arising from Eq. (1.10) with parameters ($m^* = 0.43m_e, V = 8$ meV$, w = 18$ meV$, \psi = 32\pi/45, \theta = 1°$) adopted from Ref. [23] is shown in Fig. 1.2b). The two topmost bands are isolated and have Chern number $C = \pm 1$ for small twist angles $\theta \lesssim 1.5°$. They can be accurately described by a Haldane-like tight-binding model on a honeycomb lattice [19, 23]. The Wannier orbitals corresponding to the two sublattices are localized in different layers on the XM and MX sites respectively [23, 24]. Consequently, hopping between nearest-neighbor sites corresponds to inter-layer tunneling and is purely real. In contrast, next-nearest-neighbor hopping is an intra-layer process, which can acquire a complex phase of $\phi = 2\pi/3$ due to the C_3 symmetry of the monolayer [61]. The time-reversal symmetric tight-binding Hamiltonian, including both valleys/spin, is a Kane-Mele model

$$H_{\mathrm{KM}} = -t_1 \sum_{\langle ij\rangle\sigma} c_{i\sigma}^\dagger c_{j\sigma} + t_2 \sum_{\langle\langle ij\rangle\rangle\sigma} e^{i\phi\sigma\nu_{ij}} c_{i\sigma}^\dagger c_{j\sigma} \tag{1.13}$$

with $\nu_{ij} = \pm 1$ depending on the direction of the hopping. By including short-range interaction terms, the model can spontaneously break time-reversal symmetry hosting both the integer and fractional quantum anomalous Hall effect [11, 13, 21, 23, 36–38, 40]. The mapping to a Kane-Mele model is only valid for small twist angles $\theta \lesssim 1.5°$. At the critical angle $\theta_c \sim 1.5°$ the gap between the second and third band closes, and the Chern numbers of the first three bands change from $(+1, -1, 0)$ to $(+1, +1, -2)$. In this regime, the first three bands can be described by a $\pi/3$-Hofstadter model on a triangular lattice [24]. Note that the precise value of the critical twist angle θ_c depends on the model parameters obtained from first principle calculations. Values ranging from $\theta_c = 1.5°$ to above 3° are found in the literature [23, 24]. Experimentally, fractional quantum anomalous Hall states have been observed for twist angles in the range 3° to 4° [11–14].

The rest of this thesis is structured as follows: In Sec. 2.1, we review elastic tunneling spectroscopy, and in Sec. 2.2, we calculate the expected signal for both an AFM and FM GWC. In Sec. 2.3, we review inelastic tunneling spectroscopy, and in Sec. 2.4, we show the qualitative differences in the dynamical spin-structure factor between the AFM and FM GWC. In Sec. 3, we propose that the QTM can also be used to probe quantum phase transitions, in particular focusing on a possible transition between a chiral spin liquid (CSL) and the ordered 120° state in the half-filled

Hubbard model on a triangular lattice, where the onset of order manifests itself in a softening of a collective mode at the ordering wave vector. In Sec. 4, we explore the effect of an external magnetic field on the response of the QTM. In Sec. 5.1 and 5.2, we show how the QTM can be used to characterize integer and fractional quantum anomalous Hall states, respectively. We conclude in Sec. 6 with an outlook. Technical details are deferred to the appendices.

Secs. 1.1, 1.3, 2, 3, and 6 are based on Ref. [1], while the remaining Secs. 1.2, 1.4, 4, and 5, have not been published yet.

Chapter 2

Probing generalized Wigner crystals

2.1 Single-particle spectral function from elastic tunneling

The schematic setup for the QTM, realized experimentally in Ref. [57], is shown in Fig. 2.1a). The idea is similar to a conventional scanning tunneling microscope, but an extended sheet of graphene replaces the tip of the microscope. The tunneling current $I(\theta, \phi)$ between the graphene layer and the bottom layer, which one wants to examine, is measured as a function of the applied voltage ϕ and the relative twist angle θ. Compared to a scanning tunneling microscope, spatial resolution is lost. Instead, the QTM has a momentum space resolution given by the linear size of the graphene layer $\delta k \sim L^{-1}$. As we show in the following, the tunneling current is a convolution of the spectral functions $\mathcal{A}_\ell(\mathbf{k}, \omega)$ of the top and bottom layer [57]

$$I(\theta, \phi) = 4\pi e |\Gamma_0|^2 \int \mathrm{d}\varepsilon \, \left(f_\mathfrak{t}(\varepsilon - \phi) - f_\mathfrak{b}(\varepsilon) \right) \sum_\mathbf{k} \mathcal{A}_\mathfrak{b}(\mathbf{k}, \varepsilon) \mathcal{A}_\mathfrak{t}(\mathbf{k}, \varepsilon - \phi) \tag{2.1}$$

where $f_\ell(\omega)$ is the Fermi-Dirac distribution, $\ell \in \{\mathfrak{t}, \mathfrak{b}\}$ is the layer index and $|\Gamma_0|^2$ is the elastic tunneling amplitude. The dependence of the tunneling current on the twist angle θ is implicitly contained in the momentum of the top layer, which is rotated with respect to the bottom layer. One can effectively scan through the Brillouin zone of the bottom layer by varying the twist angle θ. This is illustrated in the lower panel of Fig. 2.1a), where the Dirac point of the graphene layer traces a path through momentum space. Since the lattice constant for the moiré lattice $a_M \sim 10$ nm is much larger than the lattice constant of graphene $a_{\mathrm{gr}} \sim 0.25$ nm, a small twist angle θ is already sufficient to cross the entire moiré Brillouin zone. Generically, the Brillouin zones of the top and bottom layer will be incommensurate with respect to each other, which implies that there is no guarantee that the path traced by the top layer's Dirac point will cross high symmetry points of interest in the bottom layer's Brillouin zone. Nevertheless, it is possible to explore several different cuts and approximately reach high symmetry points by varying the twist angle over a wide enough range.

Our derivation of Eq. (2.1) is based on Refs. [58, 59, 63]. We calculate the tunneling current between two layers, described by the independent Hamiltonians $H_\mathfrak{t}$ and $H_\mathfrak{b}$ for the top and bottom layer respectively. The two layers are separated by a third intermediate layer, serving as a tunneling barrier. The top layer is the graphene sheet, the bottom layer is the sample, and the middle layer is an insulating spacer layer that prevents hybridization between the top and bottom layers. The total Hamiltonian of the system can be written as

$$H = H_\mathfrak{t} + H_\mathfrak{b} + H_{\mathrm{barr}} + H_{\mathrm{tun}}. \tag{2.2}$$

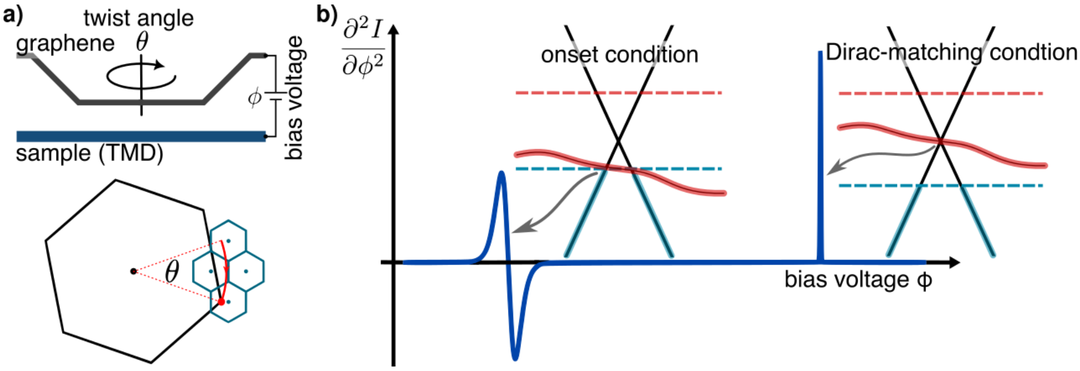

FIGURE 2.1: **Quantum twisting microscope. a)** Top: Illustration of the QTM with a graphene layer on top of the sample layer. The top layer is twisted by an angle θ with respect to the bottom layer, and a voltage ϕ is applied between the two layers. Bottom: By changing the twist angle θ, the Dirac points of graphene, located at the corners of its Brillouin zone, trace a path through momentum space (shown in red). For moiré lattices, the Brillouin zone of the bottom layer (blue) is much smaller than the one of graphene (black), such that a small twist angle already cuts through the entire Brillouin zone of the sample. **b)** Illustration of the second derivative of the tunneling current as a function of the applied voltage ϕ for fixed twist angle. There are two main features: a sharp temperature-independent peak at the Dirac-matching condition, arising when the Dirac point of graphene touches an energy surface of the bottom layer, and a resonance peak at the onset condition when tunneling becomes energetically allowed. The tunneling current is proportional to the intersection length between the energy surfaces within the allowed energy interval set by the chemical potentials.

We assume that $H_\mathfrak{t}$, $H_\mathfrak{b}$, and H_{barr} all commute with each other and are only coupled through the tunneling Hamiltonian

$$H_{\text{tun}} = \sum_{i,j} \sum_{ab,\sigma\sigma'} \left(T^{ab}_{\sigma\sigma'}(\mathbf{x}_i, \mathbf{x}_j) c^\dagger_{\sigma a \mathfrak{t} i} c_{\sigma' b \mathfrak{b} j} e^{i\phi t} + \text{h.c.} \right) \tag{2.3}$$

where $c^\dagger_{\sigma a \ell i}$ ($c_{\sigma a \ell i}$) creates (destroys) an electron in layer $\ell \in \{\mathfrak{t}, \mathfrak{b}\}$ on lattice site $\mathbf{x}_i$ with spin σ and sublattice a. Generically, the (sub-)lattice structure of the top and bottom layers are not assumed to be the same. The bias voltage ϕ between the top and bottom layer appears as a time-dependent phase. Assuming that the top and bottom layers are separated by a distance d and that a constant potential Φ can approximate the tunneling barrier, a WKB approximation yields a tunneling amplitude of

$$T \sim \exp\left[-\sqrt{\frac{\Phi - E}{\Phi_0}} \right] \tag{2.4}$$

with $\Phi_0 := \frac{8md^2}{\hbar^2}$ and E being the energy of the electron. We assume that the electron can couple to spin excitations of the intermediate layer, see Fig. 2.4a), leading to $E = J\mathbf{s} \cdot \boldsymbol{\sigma}$, where $\mathbf{s}$ is the local magnetic moment in the intermediate layer and J is an effective coupling. For small couplings $J/\Phi \ll 1$, the tunneling amplitude Eq. (2.4) can be expanded [64, 65]:

$$T = \Gamma_0 \mathbb{1} + \Gamma_1 \hat{\mathbf{s}} \cdot \boldsymbol{\sigma} \tag{2.5}$$

with

$$\frac{\Gamma_1}{\Gamma_0} = \tanh \frac{J|\mathbf{s}|}{2\Phi} \simeq \frac{J|\mathbf{s}|}{2\Phi} \ll 1. \tag{2.6}$$

We see two contributions to the tunneling amplitude: a dominating term without spin-flips and a term coupling to spin excitations, suppressed by a relative factor of $\sim J/\Phi$. This motivates the following matrix elements in our tunneling Hamiltonian

$$T^{ab}_{\sigma\sigma'}(\mathbf{x}_i, \mathbf{x}_j) = \Gamma_0(\Delta\mathbf{r}^{ab}_{ij})\delta_{\sigma\sigma'} + \Gamma_1(\Delta\mathbf{r}^{ab}_{ij})\sigma^{\mu}_{\sigma\sigma'}s^{\mu}(\mathbf{R}^{ab}_{ij}) \tag{2.7}$$

where $\Delta\mathbf{r}^{ab}_{ij} := (\mathbf{x}_i + \mathbf{r}_a) - (\mathbf{x}_j + \mathbf{r}_b)$ is the relative distance between site i on sublattice a of the top layer and site j on sublattice b of the bottom layer, while $\mathbf{R}^{ab}_{ij} := (\mathbf{x}_i + \mathbf{r}_a + \mathbf{x}_j + \mathbf{r}_b)/2$ is their midpoint. Note that the first term in Eq. (2.7) only depends on the relative distance between the two sites and hence only contributes to elastic tunneling. Inelastic contributions stem from the second term. By taking a Fourier transform

$$c_{\sigma a \ell i} = \frac{1}{\sqrt{N}}\sum_{\mathbf{k}} e^{i\mathbf{k}\cdot(\mathbf{x}_i+\mathbf{r}_a)}c_{\sigma a \ell \mathbf{k}} \tag{2.8}$$

$$T^{ab}_{\sigma\sigma'}(\Delta\mathbf{r}, \mathbf{R}) = \frac{1}{N}\sum_{\mathbf{q},\mathbf{q}'} e^{-i\mathbf{q}\cdot\mathbf{R}}e^{-i\mathbf{q}'\cdot\Delta\mathbf{r}}T^{ab}_{\sigma\sigma'}(\mathbf{q}, \mathbf{q}') \tag{2.9}$$

we can rewrite the tunneling Hamiltonian as follows

$$H_{\text{tun}} = \sum_{ab,\sigma\sigma'}\sum_{\mathbf{k}\mathbf{k}'}\sum_{\mathbf{g}_{\mathfrak{t}}\mathbf{g}_{\mathfrak{b}}}\left(T^{ab}_{\sigma\sigma'}(\mathbf{q}, \mathbf{q}')e^{-i(\mathbf{r}_{\mathfrak{t}a}\cdot\mathbf{g}_{\mathfrak{t}} - \mathbf{r}_{\mathfrak{b}b}\cdot\mathbf{g}_{\mathfrak{b}})}c^{\dagger}_{\sigma a \mathfrak{t}\mathbf{k}}c_{\sigma' b \mathfrak{b}\mathbf{k}'}e^{i\phi t} + \text{h.c.}\right) \tag{2.10}$$

where $\mathbf{r}_{\ell a}$ is the position of sublattice a within the unit cell of layer ℓ and $\mathbf{g}_{\ell}$ are reciprocal lattice vectors of layer ℓ. Furthermore, we have $\mathbf{q} = \mathbf{k} - \mathbf{k}' + \mathbf{g}_{\mathfrak{t}} - \mathbf{g}_{\mathfrak{b}}$ and $\mathbf{q}' = (\mathbf{k} + \mathbf{k}' + \mathbf{g}_{\mathfrak{t}} + \mathbf{g}_{\mathfrak{b}})/2$. The tunneling matrix elements in momentum space can be explicitly written as

$$T_{\sigma\sigma'}(\mathbf{q}, \mathbf{q}') = \Gamma_0(\mathbf{q}')\delta_{\mathbf{q},0}\delta_{\sigma\sigma'} + \Gamma_1(\mathbf{q}')\sigma^{\mu}_{\sigma\sigma'}s^{\mu}_{\mathbf{q}} \tag{2.11}$$

with

$$s^{\mu}_{\mathbf{q}} = \frac{1}{N}\sum_{\mathbf{R}} e^{i\mathbf{R}\cdot\mathbf{q}}s^{\mu}(\mathbf{R}). \tag{2.12}$$

Next, we calculate the tunneling current $I(t) := -e\langle \dot{N}_{\mathfrak{t}}(t)\rangle$ with $N_{\ell} := \sum_{\mathbf{k}\sigma a} c^{\dagger}_{\sigma \ell a \mathbf{k}}c_{\sigma \ell a \mathbf{k}}$. Time-dependent perturbation theory yields

$$I(t) = -ie\int_{-\infty}^{\infty} \mathrm{d}t'\theta(t - t')\langle [H_{\text{tun}}(t'),\ \dot{N}_{\mathfrak{t}}(t)]\rangle \tag{2.13}$$

with $\dot{N}_{\mathfrak{t}} = i[H_{\text{tun}},\ N_{\mathfrak{t}}]$. By introducing the bilinear operator

$$A(t) := \sum_{ab,\sigma\sigma'}\sum_{\mathbf{k}\mathbf{k}'}\sum_{\mathbf{g}_{\mathfrak{t}}\mathbf{g}_{\mathfrak{b}}} T^{ab}_{\sigma\sigma'}(\mathbf{q}, \mathbf{q}')e^{-i(\mathbf{r}_{\mathfrak{t}a}\cdot\mathbf{g}_{\mathfrak{t}} - \mathbf{r}_{\mathfrak{b}b}\cdot\mathbf{g}_{\mathfrak{b}})}c^{\dagger}_{\sigma a \mathfrak{t}\mathbf{k}}(t)c_{\sigma' b \mathfrak{b}\mathbf{k}'}(t) \tag{2.14}$$

one can compactly write

$$\begin{aligned} H_{\text{tun}} &= A(t)e^{i\phi t} + A^{\dagger}(t)e^{-i\phi t} \\ \dot{N}_{\mathfrak{t}}(t) &= -i\left[A(t)e^{i\phi t} - A^{\dagger}(t)e^{-i\phi t}\right], \end{aligned} \tag{2.15}$$

which yields the single-particle contribution I_S to the tunneling current

$$\begin{aligned} I_S(\phi) &= e\int_{-\infty}^{\infty} \mathrm{d}t'\theta(t-t')\left[e^{i\phi(t-t')}\left\langle[A(t),\,A^{\dagger}(t')]\right\rangle - e^{-i\phi(t-t')}\left\langle[A^{\dagger}(t),\,A(t')]\right\rangle\right] \\ &= -2e\,\operatorname{Im} U_{\mathrm{ret}}(\phi). \end{aligned} \tag{2.16}$$

To obtain the tunneling current I_S, we have to calculate the retarded Green's function defined by

$$U_{\mathrm{ret}}(\omega) = -i\int_{-\infty}^{\infty} \mathrm{d}t\; e^{i\omega t}\theta(t)\left\langle[A(t),\,A^{\dagger}(0)]\right\rangle. \tag{2.17}$$

This can be achieved by first computing the Green's function in the imaginary time formalism

$$\mathcal{U}(i\omega_n) = -\int_0^{\beta} \mathrm{d}\tau\; e^{i\omega_n\tau}\left\langle\mathcal{T}A(\tau)A^{\dagger}(0)\right\rangle \tag{2.18}$$

and then taking the analytical continuation $i\omega_n \to \omega + i\eta$ to obtain the retarded Green's function. Here $\mathcal{T}$ is the imaginary time ordering operator. To proceed, we make some simplifying assumptions. First, we set $\Gamma_1 = 0$ since, in this section, we are only interested in the elastic contribution to the tunneling current. Furthermore, we assume that the typical in-plane length scale is very small compared to the layer-to-layer distance d, which implies that $\Gamma_0(\mathbf{q}')$ decays rapidly as a function of $|\mathbf{q}'|$ [66]. Hence, we can assume it to be constant for the first shell of reciprocal lattice vectors and vanishing otherwise. As in the main text, we focus on the special case where the top layer is a monolayer graphene. For simplicity, we only consider tunneling around a single Dirac point. Thus, for convenience, we redefine momentum to be measured with respect to the K point of the top layer Brillouin zone. Making use of Wick's theorem and defining the single-particle Green's function as $\mathcal{G}_{\ell}(\mathbf{k}, i\nu_n) := -\int_0^{\beta} \mathrm{d}\tau\; e^{i\nu_n\tau}\langle\mathcal{T}c_{\sigma\ell\mathbf{k}}(\tau)c^{\dagger}_{\sigma\ell\mathbf{k}}(0)\rangle$, we arrive at the following result

$$\mathcal{U}^{(0)}(i\omega_n) = \frac{2|\Gamma_0|^2}{\beta}\sum_{\mathbf{k},\nu_l}\mathcal{G}_{\mathfrak{b}}(\mathbf{k}, i\nu_l + i\omega_n)\mathcal{G}_{\mathfrak{t}}(\mathbf{k}, i\nu_l). \tag{2.19}$$

The Matsubara sum can be performed by making use of the Lehman representation

$$\mathcal{G}_{\ell}(\mathbf{k}, i\omega_n) = \int_{-\infty}^{\infty} \mathrm{d}\varepsilon\;\frac{\mathcal{A}_{\ell}(\mathbf{k},\varepsilon)}{i\omega_n - \varepsilon} \tag{2.20}$$

where $\mathcal{A}_{\ell}(\mathbf{k},\varepsilon) = -\operatorname{Im}\mathcal{G}(\mathbf{k},\varepsilon)/\pi$ is the single-particle spectral function of layer ℓ. After taking the analytical continuation $i\omega_n \to \omega + i\eta$, we arrive at the final result for the elastic tunneling current Eq. (2.1).

We assume tunneling only occurs near the K and K' points of the top layer's Brillouin zone, where we can describe graphene as a gas of massless Dirac fermions. To develop an intuitive understanding of the QTM, focus on one K point with its corresponding Dirac cone. If we assume that the spectral functions define a sharp energy surface in momentum space, then the convolution in Eq. (2.1) can be understood by a simple geometric picture: The tunneling current is proportional to the length of the intersection between the Dirac cone and the energy surfaces defined by the spectral function of the bottom layer. A given intersection only contributes to the current if it lies within the energy interval defined by the chemical potentials μ_{ℓ}, such that one of the energy bands is filled while the other is empty. Since we assume the filling of the sample layer to be constant, we fix its chemical potential $\mu_{\mathfrak{b}}$, while $\mu_{\mathfrak{t}}$ can be varied. This allows for measuring both the particle and hole part of the spectral function. Assuming $\mu_{\mathfrak{t}} < \mu_{\mathfrak{b}}$, one measures electrons tunneling from the bottom to the top layer, effectively determining the hole spectrum of the sample. The situation is reversed for $\mu_{\mathfrak{t}} > \mu_{\mathfrak{b}}$, where the particle spectrum is measured. In the geometric picture, the position of the Dirac point can be tuned vertically by changing the electrostatic bias potential ϕ between the layers and horizontally by varying the twist angle θ. If the Dirac point lies exactly on an energy surface of the bottom layer, there will be no contribution to the current since the density of states at this point vanishes (in the geometric picture described above, the length of the intersection between the surfaces is zero). This condition, dubbed *Dirac-matching condition*, leads to a sharp peak in the second derivative of the tunneling current with respect to ϕ. Compared to the typical energy scales $\varepsilon_{\mathfrak{b}}$ within a moiré lattice with lattice constant a_M, the graphene's Fermi velocity v_F is very large $\hbar v_F / a_M \gg \varepsilon_{\mathfrak{b}}$. In this limit, the Dirac cone forms a very sharp momentum-resolved tip, which scans the spectral function of the bottom layer. The latter is generically written as

$$\mathcal{A}_{\mathfrak{b}}(\mathbf{k},\omega) = \sum_{\alpha} Z^{\alpha}_{\mathbf{k}} \delta(\omega - \varepsilon^{\alpha}_{\mathfrak{b}}(\mathbf{k})) + \text{continuum} \tag{2.21}$$

with a band index α and spectral weight $Z^{\alpha}_{\mathbf{k}}$. This leads to the tunneling current

$$I(\mathbf{q}(\theta),\phi) \propto \sum_{\alpha} Z^{\alpha}_{\mathbf{q}} |\varepsilon^{\alpha}_{\mathfrak{b}}(\mathbf{q}) - \phi| \left[f_{\mathfrak{t}}(\varepsilon^{\alpha}_{\mathfrak{b}}(\mathbf{q}) - \phi) - f_{\mathfrak{b}}(\varepsilon^{\alpha}_{\mathfrak{b}}(\mathbf{q})) \right] \tag{2.22}$$

with $\mathbf{q}(\theta) = \mathrm{R}(\theta)\mathbf{K} - \mathbf{g}$, where $\mathrm{R}(\theta)$ is a rotation matrix, and $\mathbf{g}$ is a reciprocal lattice vector, ensuring that $\mathbf{q}$ lies within the first Brillouin zone of the bottom layer. Here, we have no longer explicitly written the contribution from the continuum part of the spectral function.

More direct information is contained in the second derivative of the tunneling current

$$\begin{aligned} \frac{\partial^2 I}{\partial \phi^2} &= \gamma_1 \sum_{\alpha} Z^{\alpha}_{\mathbf{q}} \delta(\varepsilon^{\alpha}_{\mathfrak{b}}(\mathbf{q}) - \phi) \left[f_{\mathfrak{t}}(\varepsilon^{\alpha}_{\mathfrak{b}}(\mathbf{q}) - \phi) - f_{\mathfrak{b}}(\varepsilon^{\alpha}_{\mathfrak{b}}(\mathbf{q})) \right] \\ &\quad + \gamma_2 \sum_{\alpha} Z^{\alpha}_{\mathbf{q}} \frac{\partial}{\partial \phi} \left(|\varepsilon^{\alpha}_{\mathfrak{b}}(\mathbf{q}) - \phi| \frac{\partial}{\partial \phi} f_{\mathfrak{t}}(\varepsilon^{\alpha}_{\mathfrak{b}}(\mathbf{q}) - \phi) \right) \end{aligned} \tag{2.23}$$

with some constants $\gamma_1 \sim \gamma_2$. In Fig. 2.1b), a typical example of $\partial^2_{\phi} I$ for fixed twist angle is sketched. There are two contributions: a distinct peak for $\varepsilon^{\alpha}_{\mathfrak{b}}(\mathbf{q}) = \phi$ corresponding to the Dirac-matching condition discussed above and a second feature stemming from the ϕ-dependence of the energy-interval in which tunneling is allowed. This second feature manifests as a maximum followed immediately by a minimum of the second derivative of the current at the point where tunneling first becomes allowed energetically. This resonance peak is dubbed the *onset condition* [57]. Note that the strength of the peak of the Dirac-matching condition is based solely on density of states arguments and hence does not significantly depend on temperature. In contrast, the peaks associated with the onset condition get less pronounced with higher temperatures. Furthermore, by choosing the chemical potential of the top layer to be sufficiently large compared to the bias voltage $|\mu_{\mathfrak{t}}| \gg \phi$, one can neglect the contribution from the onset condition. In that case, $\partial^2_{\phi} I$ directly measures the spectral function of the bottom layer.

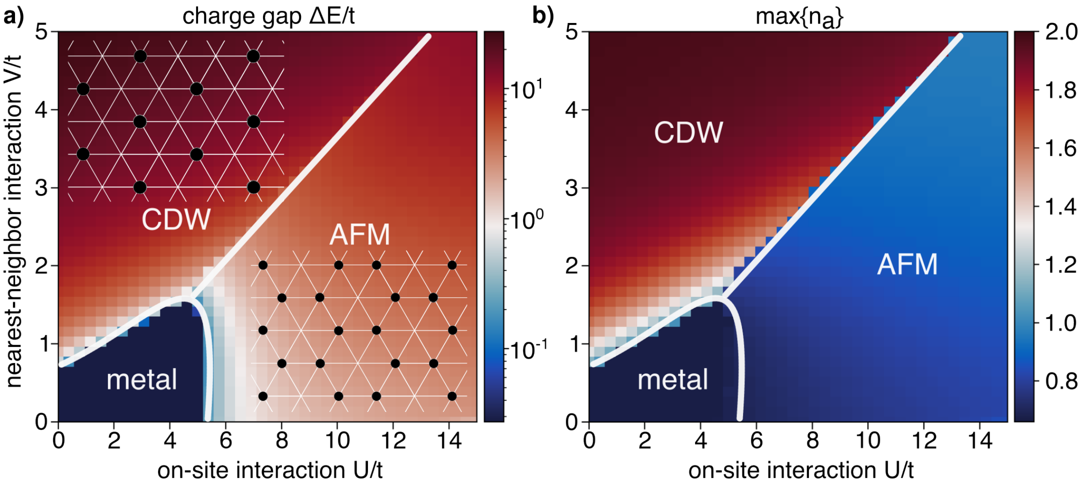

FIGURE 2.2: **Mean-field phase diagram at ν=2/3 filling.** For $X = 0$ we find three distinct phases as a function of the on-site interaction U/t and nearest-neighbor interaction V/t: a metallic phase for small interaction strengths, an antiferromagnetic phase (AFM) with honeycomb charge order for $V < 3U$ and a charge density wave (CDW) with $\sqrt{3} \times \sqrt{3}$ charge order for $V > 3U$. **a)** Charge gap. The charge order for the CDW and AFM phases is shown. We use a logarithmic color scale to more easily distinguish visually between the phases. To plot the vanishing charge gap in the metallic phase, we have replaced it with a finite value of $10^{-8}t$. **b)** Maximum average occupation number over the three sublattices. In the CDW phase, one sublattice is doubly occupied, while the other two are empty. In the AFM phase, two sublattices are singly occupied, while the third is empty, and in the metallic phase, all three sublattices have an average occupation number of $n = 2/3$.

2.2 Probing single-particle excitations of generalized Wigner crystals

The QTM can be used to identify different magnetic correlations. We explicitly calculate the single-particle spectral function for GWCs with antiferromagnetic and ferromagnetic spin order and show that the different states have distinct signatures.

2.2.1 Mean-field phase diagram of the extended Hubbard model

We describe the TMD heterobilayer moiré superlattice with an extended Hubbard model [18, 25]

$$\begin{aligned} H &= -t \sum_{\langle i,j\rangle \sigma} (c^\dagger_{\sigma i} c_{\sigma j} + \text{h.c.}) + U \sum_i n_{\uparrow i} n_{\downarrow i} + V \sum_{\substack{\langle ij \rangle \\ \sigma,\sigma'}} n_{\sigma i} n_{\sigma' j} + X \sum_{\substack{\langle ij \rangle \\ \sigma\sigma'}} c^\dagger_{\sigma i} c^\dagger_{\sigma' j} c_{\sigma' i} c_{\sigma j} \\ &= H_t + H_u + H_v + H_x \end{aligned} \tag{2.24}$$

with the number operator $n_{\sigma,i} = c^\dagger_{\sigma,i} c_{\sigma,i}$. Both the on-site interaction U and the nearest-neighbor interaction strength V are repulsive. Additionally, an intersite-exchange term X is included, which gives a negative contribution to the energy when two neighboring spins are aligned and a positive contribution when misaligned, thus favoring ferromagnetism. We perform a mean-field decoupling of the interaction terms of the Hamiltonian. To this end, we introduce the following notation for the order parameter $\chi^{ij}_{\sigma\sigma'} := \langle c^\dagger_{\sigma i} c_{\sigma' j} \rangle$. The resulting mean-field Hamiltonian reads:

$$H_u \simeq U \sum_{i,\sigma} (\chi^{ii}_{\sigma\sigma} c^\dagger_{\bar{\sigma}i} c_{\bar{\sigma}i} - \chi^{ii}_{\sigma\bar{\sigma}} c^\dagger_{\bar{\sigma}i} c_{\sigma i}) - U \sum_i (\chi^{ii}_{\uparrow\uparrow}\chi^{ii}_{\downarrow\downarrow} - \chi^{ii}_{\uparrow\downarrow}\chi^{ii}_{\downarrow\uparrow}) \tag{2.25}$$

$$\begin{aligned} H_v \simeq V \sum_{\langle ij\rangle} \sum_{\sigma\sigma'} \big(&\chi^{ii}_{\sigma\sigma} c^\dagger_{\sigma' j} c_{\sigma' j} + \chi^{jj}_{\sigma'\sigma'} c^\dagger_{\sigma i} c_{\sigma i} - \chi^{ji}_{\sigma'\sigma} c^\dagger_{\sigma i} c_{\sigma' j} \\ &- \chi^{ij}_{\sigma\sigma'} c^\dagger_{\sigma' j} c_{\sigma i} - \chi^{ii}_{\sigma\sigma}\chi^{jj}_{\sigma'\sigma'} + \chi^{ji}_{\sigma'\sigma}\chi^{ij}_{\sigma\sigma'}\big) \end{aligned} \tag{2.26}$$

$$\begin{aligned} H_x \simeq X \sum_{\langle ij\rangle} \sum_{\sigma\sigma'} \big(&\chi^{ii}_{\sigma\sigma'} c^\dagger_{\sigma' j} c_{\sigma j} + \chi^{jj}_{\sigma'\sigma} c^\dagger_{\sigma i} c_{\sigma' i} - \chi^{ij}_{\sigma\sigma} c^\dagger_{\sigma' j} c_{\sigma' i} \\ &- \chi^{ji}_{\sigma'\sigma'} c^\dagger_{\sigma i} c_{\sigma j} - \chi^{jj}_{\sigma'\sigma}\chi^{ii}_{\sigma\sigma'} + \chi^{ij}_{\sigma\sigma}\chi^{ji}_{\sigma'\sigma'}\big). \end{aligned} \tag{2.27}$$

In the following, we focus on a filling of $\nu = 2/3$ electrons per site, where the formation of GWCs is expected [31, 67–69]. We introduce a three-site unit cell, which is sufficient to accommodate the expected spin and charge order at this filling. The corresponding fermionic creation (annihilation) operator for site i on sublattice $a \in \{A, B, C\}$ and spin $\sigma \in \{\uparrow, \downarrow\}$ is denoted by $c^\dagger_{a\sigma i}$ ($c_{a\sigma i}$). By translation invariance, the mean-field parameters only depend on the relative distance between sites i and j. Consequently, we can rewrite them as matrices in sublattice space: $\chi^{ab}_{\sigma\sigma'} := \langle c^\dagger_{a\sigma i} c_{b\sigma' i}\rangle$. Next, we Fourier transform to momentum space

$$c_{a\sigma i} = \frac{1}{\sqrt{N}} \sum_{\mathbf{k}} e^{i\mathbf{k}\cdot\mathbf{x}_i} c_{a\sigma\mathbf{k}}, \tag{2.28}$$

where N is the number of unit cells, and the momentum sum is over the reduced Brillouin zone obtained by increasing the unit cell to contain three sites. We bring the mean-field Hamiltonian into bilinear form

$$H = \sum_{\mathbf{k}} \Psi^\dagger_{\mathbf{k}} h_{\mathbf{k}} \Psi_{\mathbf{k}} + E_0 \tag{2.29}$$

with some constant energy E_0, the sublattice spinor $\Psi_{\mathbf{k}} = (c_{A\uparrow\mathbf{k}}, c_{A\downarrow\mathbf{k}}, c_{B\uparrow\mathbf{k}}, c_{B\downarrow\mathbf{k}}, c_{C\uparrow\mathbf{k}}, c_{C\downarrow\mathbf{k}})^T$ and a 6×6 matrix $h_{\mathbf{k}}$. The matrix $h_{\mathbf{k}}$ depends on the mean-field parameters $\chi^{ab}_{\sigma\sigma'}$, which must be self-consistently determined. To find a self-consistent mean-field solution, we iteratively diagonalize the Hamiltonian of Eq. (2.29) and use the resulting ground state to compute $\chi^{ab}_{\sigma\sigma'}$. The explicit form for the matrix $h_{\mathbf{k}}$ and the energy shift E_0 is given in Appendix A.1. The chemical potential is determined implicitly by fixing the electron density ν, given by the number of electrons per site.

Our mean-field calculations for $\nu = 2/3$ are in good agreement with previous mean-field [67, 68, 70, 71] and exact-diagonalization studies [31]. The mean-field phase diagram for $X = 0$ is shown in Fig. 2.2. We find a disordered metallic phase for small interactions U and V. Increasing the onsite-interaction U, the ground state undergoes a crystallization transition and forms an antiferromagnetic spin state, where one sublattice is empty. Hence, the electrons arrange themselves in an effective honeycomb lattice as shown in Fig. 2.2a). Remarkably, the phase survives on a mean-field level down to $V = 0$, where one would naively no longer expect the stabilization of honeycomb charge order. This configuration is favored due to an interplay between spin and charge ordering. By crystallizing in a honeycomb lattice, the electrons can access an unfrustrated antiferromagnetic spin configuration, lowering their energy. For very strong nearest-neighbor interactions $V > U/3$, it becomes energetically favorable to doubly occupy one sublattice while leaving

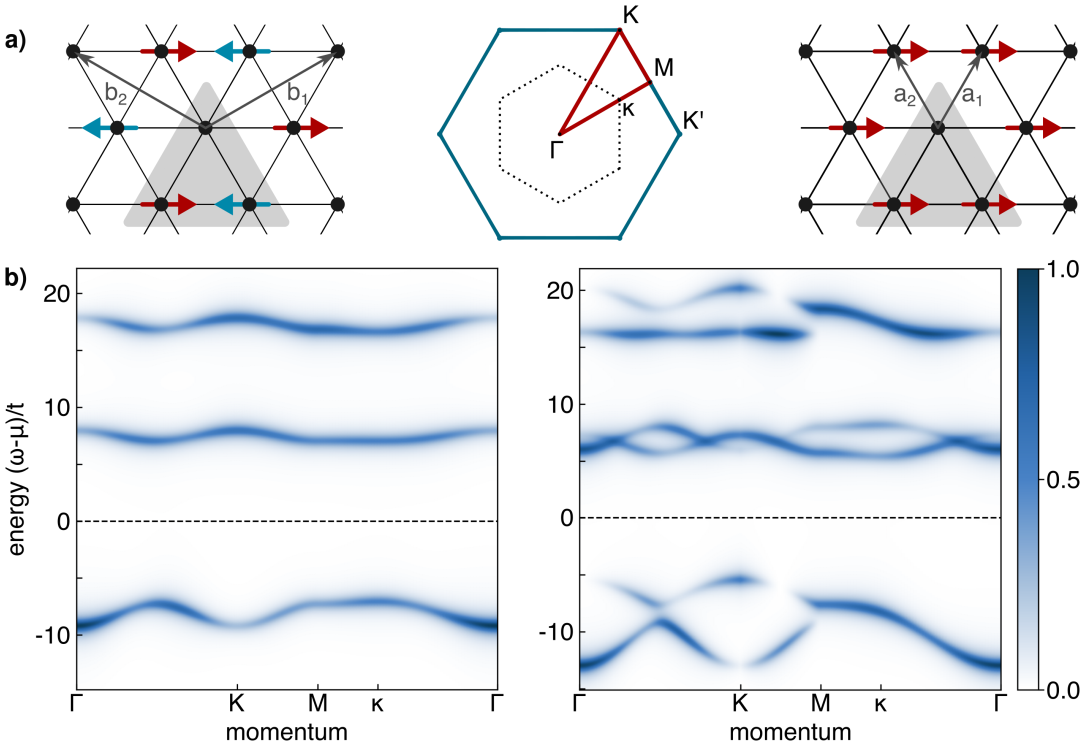

FIGURE 2.3: **Single-particle spectral function for generalized Wigner crystals. a)** Schematics of antiferromagnetic (left) and ferromagnetic (right) generalized Wigner crystal states. The chosen unit cell is highlighted in grey. The central panel shows the Brillouin zone of the sample (blue), including the reduced Brillouin zone (dashed) and the path used to plot the spectral functions. **b)** Spectral function $\mathcal{A}(\mathbf{k}, \omega)$ for the antiferromagnetic (left, $U = 25t$, $V = 5t$, $X = 0$) and ferromagnetic phase (right, $U = 25t$, $V = 5t$, $X = 0.3t$).

the other two sublattices empty, thus avoiding the nearest-neighbor energy penalty completely. In Fig. 2.2a), the charge order for this $\sqrt{3} \times \sqrt{3}$ charge density wave is shown as an inset. We plot the charge gap as a function of on-site interaction U and nearest-neighbor interaction V in Fig. 2.2a). In agreement with an exact diagonalization study [72], we find the charge gap to open continuously at the transition from the metal to both generalized Wigner crystal phases. We discuss the possible nature of this transition in some more detail in Chapter 3. In Fig 2.2b), we use the maximum average occupation over the three sublattices max $\langle n_a \rangle$ for $a \in \{A, B, C\}$, as an order parameter. In the metallic phase, all three sublattices have the same average occupation number of $\langle n \rangle = 2/3$. In the antiferromagnetic phase, two sublattices have an average occupation number of one, while the third is empty. In the charge density wave phase, one sublattice has $\langle n \rangle = 2$, while the other two are empty. For the remainder of this work, we focus on the experimentally more relevant regime with $U > 3V$, where generalized Wigner crystals with honeycomb charge order are stabilized. The corresponding spin order depends on the intersite direct exchange term X. By increasing $X > 0.2t - 0.4t$, the effective nearest-neighbor spin coupling Eq. (2.45) changes sign [31], and we find a ferromagnetic ground state instead of an antiferromagnetic one. The corresponding real-space spin configuration is shown in the right panel of Fig. 2.3a).

2.2.2 Single-particle excitations

Excitations on top of the antiferromagnetic and ferromagnetic phases differ strongly, leading to distinct experimental signatures. We present theoretical predictions for the QTM response of the different GWCs and how these signatures can be used to distinguish between the different phases. First, we calculate the single-particle spectral function

$$\mathcal{A}(\mathbf{k},\omega) = -\frac{1}{\pi}\,\mathrm{Im}\,\mathcal{G}(\mathbf{k},\omega) \tag{2.30}$$

with the retarded Green's function defined as

$$\mathcal{G}(\mathbf{k},\omega) = -i\sum_{\sigma}\int_0^{\infty} \mathrm{d}t\; e^{i\omega t}\big\langle\{c_{\sigma\mathbf{k}}(t), c^{\dagger}_{\sigma\mathbf{k}}(0)\}\big\rangle \tag{2.31}$$

and the expectation value taken with respect to the ground state. Since our main goal is to show how the QTM can distinguish different GWCs, we are only interested in a qualitative description. To characterize the main features of the spectral function, we focus on the bare mean-field response [73]. Computational details are given in Appendix A.1. In Fig. 2.3b), we present representative results for the spectral functions in the AFM (left panel) and FM (right panel) phases.

In the antiferromagnetic GWC phase, we observe one hole band and two independent particle bands. The two distinct particle bands can be understood intuitively: there are two different ways to add an electron onto the AFM ground state, either by putting it on an empty site or by putting it on an occupied site. The gap and the bandwidth can be calculated using second-order perturbation theory. The gap between the two particle bands is approximately $\Delta E = U - 3V$ while the bandwidth is of order $t_1^{(\mathrm{eff})} \sim t_2^{\mathrm{eff}} \sim \mathcal{O}(t^2/U)$, assuming $U \gg V, t$. Detailed expressions for $t^{\mathrm{eff}}_{1/2}$ are given in Appendix A.2. Similar arguments can be made for the hole band, leading to a gap of $\Delta E = 3V$ between the hole band and the lower particle band. The bandwidth for the hole band is of the same order as for the particle bands.

The spectral function in the ferromagnetic GWC is qualitatively different. The most significant difference is that the number of mean-field bands doubles. This can be understood as a Zeeman splitting due to the non-vanishing overall magnetization. The individual bands can again be interpreted as a particle or hole moving in a mean-field background: the two topmost particle bands result from putting a particle on an already occupied site. It can freely hop on an effective hexagonal lattice, leading to a graphene-like dispersion. The closing of the gap between the two bands at the corners κ of the reduced Brillouin zone is not visible in Fig. 2.3b), as only one band has spectral weight at κ. The bandwidth of these two bands is of order $\mathcal{O}(t)$. The other two particle bands in the FM can be understood by putting a particle on an empty site. There are two possibilities: either the spin of the additional particle is aligned with its neighbors, or it is misaligned. This results in a separation of $\Delta E = 6X$, which is of a similar order as the bandwidth $\mathcal{O}(t^2/U)$, leading to several crossings. Also, the hole spectrum in the ferromagnet is graphene-like since a single hole on top of the ground state can freely hop on the effective hexagonal lattice. In contrast to the AFM-hole band, the ferromagnetic one has a bandwidth of order $\mathcal{O}(t)$.

In real materials, additional features will be present in the spectral function, which cannot be captured by mean-field theory. Nevertheless, we expect that the most prominent bands are the ones discussed above. We have shown that by directly measuring these bands using the QTM, different magnetic states in GWCs can

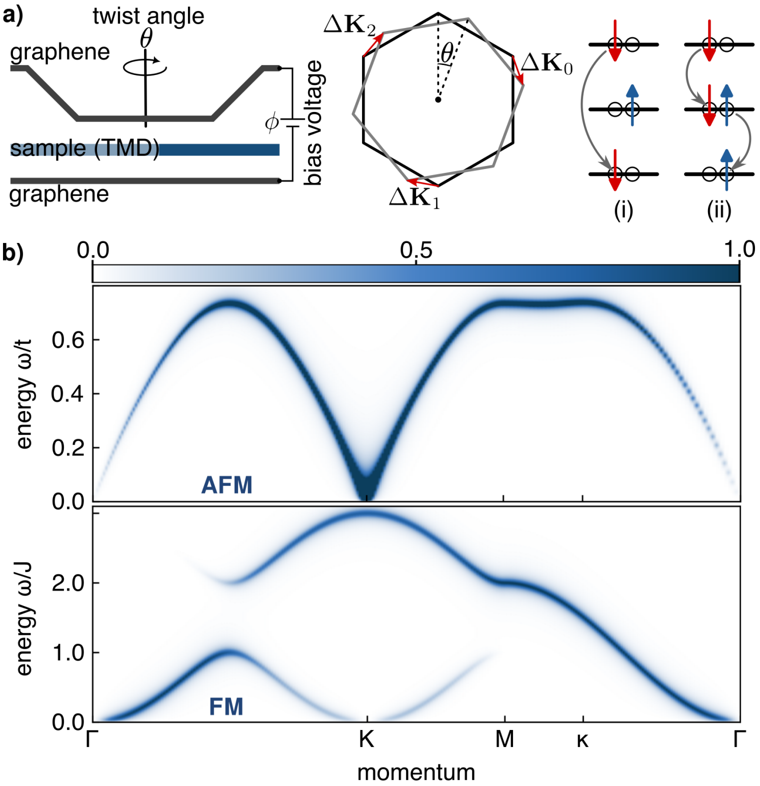

FIGURE 2.4: **Dynamical spin-structure factor for generalized Wigner crystals. a)** Left: QTM with an intermediate sample layer sandwiched between two graphene layers. The top layer is twisted by an angle θ with respect to the bottom layer, and a voltage ϕ is applied between the two graphene layers. Middle: Brillouin zones of the top and bottom layer graphene twisted by an angle θ. The measured dynamical spin-structure factor is a function of $\Delta\mathbf{K}_n$. Right: Different processes contributing to the total tunneling current: (i) elastic tunneling from top to bottom layer; (ii) inelastic tunneling where the electron virtually tunnels to the intermediate layer, effectively interacting with spin excitations of that layer. **b)** Dynamical spin-structure factor $\mathcal{S}(\mathbf{k},\omega)$ of the antiferromagnetic (top) and ferromagnetic phase (bottom).

be distinguished. In particular, the spin degenerate single-particle bands in the AFM split due to a non-vanishing overall magnetization in the FM state. This has the potential to resolve an outstanding puzzle in the field: Simple theoretical estimates yield large values for the exchange coupling X [29, 31]. In stark contrast, susceptibility measurements do not reveal the expected strong ferromagnetism [9, 20, 32]. The QTM response may provide useful insight into this puzzle.

2.3 Collective excitation spectrum from inelastic tunneling

Inelastic tunneling spectra can be measured with a QTM by sandwiching the sample in between two graphene layers [58, 59], as illustrated in Fig. 2.4a). Momentum resolution is again obtained by twisting the top layer by an angle θ. When a bias voltage ϕ is applied between the two graphene layers, electrons can tunnel directly from the top to the bottom layer. This results in an elastic contribution to the tunneling current similar to the one discussed in Sec. 2.1. In addition, the electron can also scatter off the intermediate layer, which results in an inelastic contribution to the current. Through these inelastic tunneling processes, one can probe the collective excitation spectrum of the intermediate layer. Heuristically, the electron interacts with the low-energy excitations of the sample layer, allowing for contributions to the current in regimes where elastic tunneling is forbidden by energy-momentum conservation. We calculate the inelastic contributions to the tunneling current following Refs. [58, 59]. In contrast to Sec. 2.1, we assume that the inelastic contribution to the tunneling current is finite, i.e. $\Gamma_1 \neq 0$ in Eq. (2.11). Both the top and bottom layers are taken to be monolayer graphene, while the insulating barrier is the probe of interest. We again assume that the distance between layers is large compared to the typical length scale of graphene, such that we can restrict ourselves to the first shell of reciprocal lattice vectors and take Γ_1 to be constant. We only consider contributions from the K valley of graphene for simplicity. The contributions from the K' valley are related by time-reversal symmetry. Under these assumptions, the sum over reciprocal lattice vectors in Eq. (2.14) reduces to a sum $n \in \{0,1,2\}$ over the three different K_n points as defined in Fig. 2.4a). We introduce the following matrices in sublattice space

$$T_{ab}^{(n)} = e^{-i(\mathbf{r}_{\mathfrak{t}a}\cdot\mathbf{g}_{\mathfrak{t}}^{(n)} - \mathbf{r}_{\mathfrak{b}b}\cdot\mathbf{g}_{\mathfrak{b}}^{(n)})} \tag{2.32}$$

$$\mathcal{G}_{\ell}^{ab}(\mathbf{k},\tau) = -\langle \mathcal{T} c_{\sigma a \ell \mathbf{k}}(\tau) c^{\dagger}_{\sigma b \ell \mathbf{k}}(0)\rangle \tag{2.33}$$

which allows us to write the inelastic contribution to Eq. (2.18) as

$$\begin{aligned}\mathcal{U}(i\omega_n) = -|\Gamma_1|^2 \int_0^{\beta} \mathrm{d}\tau \sum_{\mathbf{kp}} \sum_{\alpha\beta} \sum_{n=0}^{2} e^{i\omega_n \tau}\, \mathrm{Tr}\left[T^{(n)} \mathcal{G}_{\mathfrak{b}}(\mathbf{k}-\mathbf{p},\tau) T^{(n)} \mathcal{G}_{\mathfrak{t}}(\mathbf{k},-\tau)\right] \sigma^{\mu}_{\alpha\beta}\sigma^{\nu}_{\beta\alpha} \\ \times \langle \mathcal{T} s^{\mu}_{\mathbf{p}+\Delta\mathbf{K}_n}(\tau) s^{\nu}_{-\mathbf{p}-\Delta\mathbf{K}_n}(0)\rangle\end{aligned} \tag{2.34}$$

where we have made use of Wick's theorem. The twist angle dependence is implicitly contained in the difference between the K points of the top and bottom layer's Brillouin zone $\Delta\mathbf{K}_n = (\mathrm{R}(\theta) - \mathbb{1})\mathbf{K}_n$. To make further progress, we perform a unitary transformation from sublattice space to band space, where the single-particle Green's functions are diagonal by construction

$$\mathcal{G}_{\ell}^{\lambda}(\mathbf{k},\tau)\delta_{\lambda\lambda'}\delta_{\mathbf{kk}'} = \langle \mathbf{k},\lambda | \mathcal{G}_{\ell}^{ab}(\mathbf{k},\tau) | \mathbf{k}',\lambda'\rangle \tag{2.35}$$

$$T^{(n)}_{\mathbf{kk}',\lambda\lambda'} = \langle \mathbf{k},\lambda | T^{(n)} | \mathbf{k}',\lambda'\rangle . \tag{2.36}$$

Here $|\mathbf{k},\lambda\rangle$ is the Bloch-function for graphene in band $\lambda \in \{\pm 1\}$. Inserting all of this back into Eq. (2.34), performing the Matsubara sums, and taking the imaginary part after an analytical continuation, we arrive at the following result for the inelastic tunneling current

$$I^{(2)}(\phi) = 2\pi e |\Gamma_1|^2 \sum_{n=0}^{2} \int \mathrm{d}\varepsilon \sum_{\mathbf{k}} \left(n_{BE}(\varepsilon+\phi) - n_{BE}(\varepsilon)\right) \mathcal{S}(\mathbf{k}+\Delta\mathbf{K}_n, \varepsilon+\phi) \mathcal{A}^{(n)}_{\mathfrak{tb}}(\mathbf{k},\varepsilon) \tag{2.37}$$

where $n_{BE}(\varepsilon)$ is the Bose-Einstein distribution, the dynamical spin-structure factor is defined as

$$\mathcal{S}(\mathbf{q}, i\omega_n) = -\frac{1}{\pi} \mathrm{Im} \sum_{\mu} \int_0^{\beta} \mathrm{d}\tau\, e^{i\omega_n \tau} \left\langle \mathcal{T} s^{\mu}_{\mathbf{q}}(\tau) s^{\mu}_{-\mathbf{q}}(0)\right\rangle \tag{2.38}$$

and

$$\mathcal{A}^{(n)}_{\mathfrak{tb}}(\mathbf{k},\varepsilon) = \sum_{\mathbf{q},\lambda\lambda'} \int \mathrm{d}\omega \left(f_{\mathfrak{t}}(\omega) - f_{\mathfrak{b}}(\omega-\varepsilon)\right) |T^{(n)}_{\mathbf{q},\mathbf{q}+\mathbf{k},\lambda\lambda'}|^2 \mathcal{A}^{\lambda}_{\mathfrak{t}}(\mathbf{q},\varepsilon) \mathcal{A}^{\lambda'}_{\mathfrak{b}}(\mathbf{q}+\mathbf{k},\omega-\varepsilon). \tag{2.39}$$

Here $\mathcal{A}_\ell^\lambda(\mathbf{q},\varepsilon) = -\operatorname{Im}\mathcal{G}_\ell^\lambda(\mathbf{q},\varepsilon)/\pi$ is again the single-particle spectral function of graphene for layer ℓ and band λ. To further simplify the convolution of Eq. (2.37), we follow the same steps as outlined in Ref. [58]. Taking the zero-temperature limit, both the difference between Bose-Einstein and Fermi-Dirac distributions, in Eq. (2.37) and (2.39), reduce to theta-functions limiting the integration boundaries. Next, we make use of the fact that the Fermi-velocity v_F in graphene is very large compared to typical moiré scales $\hbar v_F a_{\text{gr}} \gg \mu\theta$, where a_{gr} is the lattice constant of graphene and θ is the twist angle between the top and bottom layer. Under this assumption, we can approximate $\mathcal{S}(\mathbf{k}+\Delta\mathbf{K}_n,\varepsilon) \approx \mathcal{S}(\Delta\mathbf{K}_n,\varepsilon)$. Furthermore, we assume that the chemical potentials of the top and bottom layers are large compared to the bias voltage between them $\mu_{\mathfrak{t}} = \mu_{\mathfrak{b}} \equiv \mu \gg \phi$. This allows us to assume that the density of states $\rho(\varepsilon) = \sum_{\mathbf{k}\lambda}\mathcal{A}^\lambda(\mathbf{k},\varepsilon)/N \sim |\mu+\varepsilon| \approx |\mu|$ in graphene is nearly constant for $\varepsilon < \phi$. Finally, we replace the matrix elements $|T^{(n)}_{\mathbf{q},\mathbf{q}+\mathbf{k},\lambda\lambda'}|^2$ by their average, which is unity. Under these assumptions, all momentum sums and one of the energy integrals can be carried out explicitly, leading to

$$I^{(2)}(\theta,\phi) = \gamma \sum_{n=0}^{2} \int_0^\phi \mathrm{d}\omega\ (\phi-\omega)\mathcal{S}(\Delta\mathbf{K}_n,\omega) \tag{2.40}$$

with some constant γ. Within this approximation, the second derivative of the current directly measures the dynamical spin-structure factor of the intermediate layer

$$\frac{\partial^2 I^{(2)}}{\partial\phi^2} = \gamma \sum_{n=0}^{2} \mathcal{S}(\Delta\mathbf{K}_n,\phi). \tag{2.41}$$

Note that there are additional contributions from tunneling around the K' valley, which are related to the ones from the K valley by time-reversal symmetry. Concretely, there are additional contributions in Eq. (2.40) with $\Delta\mathbf{K}_n$ replaced by $-\Delta\mathbf{K}_n$ [58]. While tunneling through the intermediate layer, the electrons may not only couple to spin excitations but also to density excitations. If t is the hopping term from the top layer to the intermediate layer and U the on-site interaction cost in the intermediate layer, then the effective spin coupling will be of order $J \sim t^2/U$ while the coupling to the density excitations will be of order U. In the insulating phase, $U/t \gg 1$ is large, and therefore, spin and density excitations lie at very different energy scales. Hence, they can be probed independently. For the contribution to the current obtained by coupling to density excitations, the result is the same as in Eq. (2.41), but with the spin structure factor replaced by the density response

$$\mathcal{S}_{\text{den}}(\mathbf{q},i\omega_n) = -\frac{1}{\pi}\operatorname{Im}\int_0^\beta \mathrm{d}\tau\ e^{i\omega_n\tau}\left\langle \mathcal{T}\rho_{\mathbf{q}}(\tau)\rho_{-\mathbf{q}}(0)\right\rangle. \tag{2.42}$$

In the kinematic region where elastic tunneling is allowed, its contribution dominates over the inelastic tunneling current, which is suppressed by a relative factor of $|J/\Phi|^2$. Here, Φ is the strength of the tunneling barrier between the top and bottom layers. Consequently, the QTM can only probe the dynamical structure factor in the absence of elastic tunneling. The condition for elastic tunneling, given by [58],

$$\phi < \hbar v_F|\Delta\mathbf{K}_n| < \phi + 2\mu \tag{2.43}$$

can be tuned in an experiment by changing the chemical potential μ of the two graphene sheets. There are also mixed contributions to the current, proportional to $\Gamma_0\Gamma_1$, but when coupling to spin excitations, they vanish since the sum over spins is zero because $\operatorname{Tr} \sigma^\mu = 0$.

2.4 Collective Magnetic Excitations of generalized Wigner crystals

We have already discussed in Sec. 2.2 how the QTM can distinguish between GWCs with ferro- and antiferromagnetic spin order by measuring the single-particle spectral function. An even more decisive difference between the two states can be seen in the spin-spin response, accessible through inelastic tunneling as described in Sec. 2.3. Collective modes can be captured by studying fluctuations around the mean-field state. Therefore we employ an RPA calculation [74–77], see Appendix B.

In the top panel of Fig. 2.4b), a representative dynamical spin-structure factor as defined in Eq. (2.38) is shown for an antiferromagnetic GWC. We note that on top of the gapless spin-wave modes, with bandwidth $\mathcal{O}(J)$, there is a gapped particle-hole continuum at an energy scale $U \gg J$. The spin-wave modes become gapless at the K and K' points of the Brillouin zone, which correspond to reciprocal lattice vectors of the extended lattice with a three-site unit cell. We observe only a single mode, which is twofold degenerate. As expected for an antiferromagnet, the spin-wave dispersion is linear in the long-wavelength limit. Deep within the AFM phase ($U \gg V, t$), the spin-wave modes can be described using an antiferromagnetic Heisenberg model on a hexagonal lattice and applying a Holstein-Primakoff transformation. The resulting spin-wave dispersion is given by

$$\varepsilon_{\mathbf{k}} = \frac{3J}{2}\sqrt{1 - |\gamma_{\mathbf{k}}|^2} \tag{2.44}$$

with $\gamma_{\mathbf{k}} = (1 + e^{i\mathbf{k}\cdot\mathbf{b}_1} + e^{i\mathbf{k}\cdot(\mathbf{b}_1+\mathbf{b}_2)})/3$. The effective nearest-neighbor spin coupling

$$J = \frac{4t^2}{U - V} - 2X \tag{2.45}$$

contains the usual superexchange term and contributions from direct exchange processes X [31]. Note that because the underlying lattice is triangular, there are also contributions to the spin coupling from spin-flip processes where an electron virtually hops to an empty site. Both the RPA formalism used to compute the spin waves in the top panel of Fig. 2.4b) and the linear spin-wave theory, which yields Eq. (2.44), do not take interactions between the collective modes into account. Such interactions would lead to a finite lifetime and renormalization of the energy [78]. Moreover, since the spin order is collinear, there are no cubic interaction terms for the spin waves, which is why we do not expect interaction effects between spin waves to influence their dispersion significantly [79, 80].

In agreement with our mean-field calculation, it is clear from Eq. (2.45) that a large intersite direct exchange term X leads to a ferromagnetic spin coupling. A representative dynamical spin-structure factor for a ferromagnetic GWC is shown in the bottom panel of Fig. 2.4b). It was calculated using linear spin-wave theory, see Appendix C.1. The magnon spectrum can again be described using a Holstein-Primakoff transformation [81], yielding

$$\varepsilon^{\pm}_{\mathbf{k}} = \frac{3J}{2}(1 \pm |\gamma_{\mathbf{k}}|). \tag{2.46}$$

The lower magnon branch is gapless at the Γ, K, and K' points of the Brillouin zone. In contrast to the antiferromagnetic case, the long wavelength behavior is quadratic instead of linear. Furthermore, the two modes are no longer degenerate. Instead, we have a second band, which is gapped at zero momentum. The upper and lower magnon bands touch at the corners κ of the reduced Brillouin zone with linear dispersion, forming bosonic Dirac cones. Note, however, that only one band has spectral weight at the κ point. We again emphasize that magnon-magnon interactions renormalize the energy of the two bands and introduce a finite lifetime to the magnons [81]. Still, the qualitative differences to the AFM case will remain.

Since the effective hexagonal lattice of the GWC requires a two-site unit cell independent of the spin order, there is no unit-cell doubling when going from the ferromagnetic to the antiferromagnetic phase. This is different at half-filling, with $\nu = 1$ electron per site. Here, the ferromagnetic state does not require an extended unit cell, while the competing antiferromagnetic 120° state requires a three-site unit cell. The QTM can also be applied to the case of half-filling to determine the dominant spin coupling. In that case, the larger unit cell of the AFM leads to a smaller periodicity in momentum space of both the single-particle spectral function and the dynamical spin-structure factor. This is an additional qualitative difference between the two types of spin-order, which is present at $\nu = 1$ and $\nu = 1/3$, which both stabilize triangular charge order, but not at $\nu = 2/3$, which stabilizes honeycomb charge order.

Chapter 3

Characterizing Quantum Criticality

3.1 Characterizing Quantum Criticality

So far, we have characterized the QTM response of spin orders in generalized Wigner crystals. Here, we discuss the QTM response in the vicinity of quantum phase transitions and demonstrate its potential as a new tool to explore critical phenomena in two-dimensional materials. As a concrete example, we focus on the half-filled Hubbard model on a triangular lattice. For simplicity, we assume $V = X = 0$. For large U/t, the ground state is the 120°-ordered state, while for small interaction strengths, we find a metallic phase. In between an intermediate Kalmeyer-Laughlin type chiral spin liquid (CSL) phase has been predicted [73, 82–86].

The charge and spin gap in the three phases are schematically shown in Fig. 3.1a). The spin gap closes at the transition from the CSL to the 120° state. At the transition from the CSL to the metal, both the spin and charge gap must close. While the former is directly observable through inelastic tunneling spectroscopy, the closing of the charge gap can be measured using elastic tunneling spectroscopy with a QTM, where the single-particle spectral function is obtained. On the metallic side of the transition, one should be able to directly observe the vanishing of the quasiparticle residue $Z \sim |U - U_c|^{2\beta}$, as predicted for a second order Mott transition [87], with a critical exponent β. Furthermore, the zero sound velocity is expected to diverge. This is, in principle, also accessible through inelastic tunneling spectroscopy by measuring the density response in the metal. Here, we consider only one possible scenario for a transition between the CSL and the 120° state, where a continuous softening of a sharp roton mode at the K point is observed, see Fig. 3.1b). We emphasize that other transitions are conceivable, e.g., via an intermediate Dirac spin liquid [88]. Crucially, we argue that the QTM response would provide important information on the phases and their transitions.

We calculate the dynamical spin-structure factor of Eq. (2.38), which is experimentally accessible through inelastic tunneling spectroscopy in both the CSL and 120° phase. We employ the RPA formalism discussed in Appendix B in both cases. The resulting spin-wave dispersion deep within the 120° phase is shown in panel (3) of Fig. 3.1b). Due to the three-sublattice structure of the ordered state, there are three distinct modes, which become soft at the Γ, K, and K' points of the Brillouin zone. Far from the transition, the three modes can again be understood using linear spin-wave theory. A Holstein-Primakoff transformation yields the following dispersion

$$\varepsilon_{\mathbf{k}} = \frac{3J}{2}\sqrt{(1+\gamma_{\mathbf{k}})(1+2\gamma_{\mathbf{k}})} \tag{3.1}$$

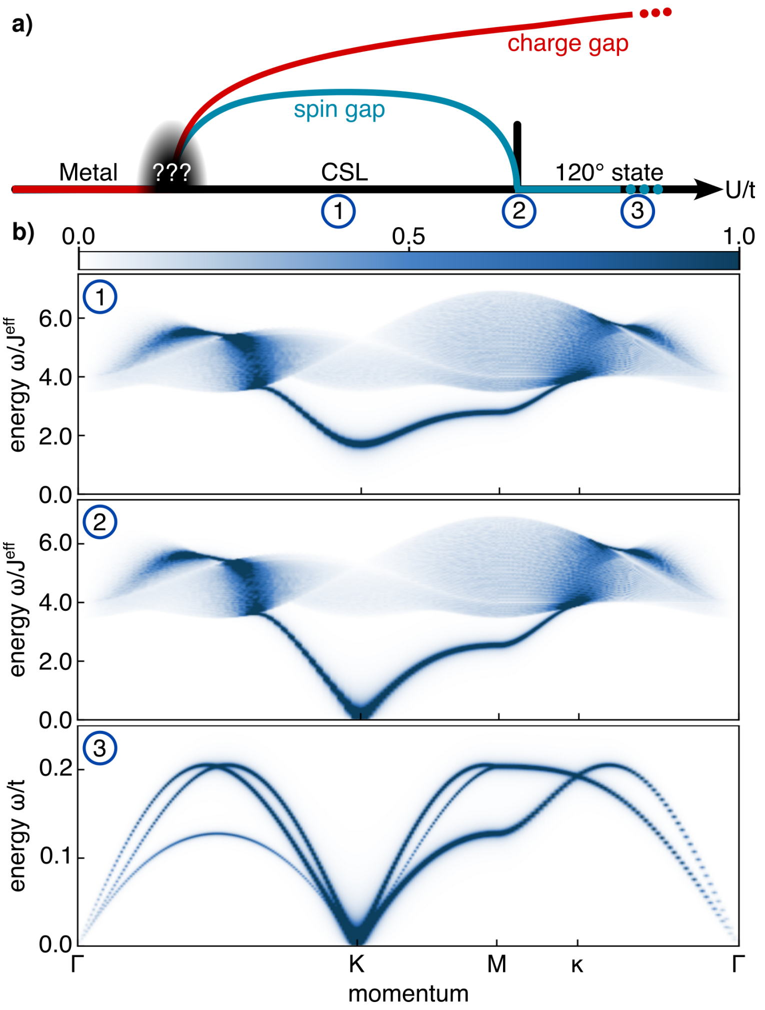

FIGURE 3.1: **Spin response across a quantum phase transition. a)** Proposed zero temperature phase diagram of the half-filled triangular Hubbard model [82, 83]. The charge and spin gap are schematically drawn as a function of interaction strength U/t. **b)** Dynamical spin-structure factor $\mathcal{S}(\mathbf{k}, \omega)$ in the chiral spin liquid (CSL) phase (1), at the critical point (2) and in the ordered 120° phase (3). The roton in the CSL becomes soft at the K point of the Brillouin zone at the critical point, indicating a transition to an ordered state.

where $\gamma_{\mathbf{k}} = 1/6 \sum_{\delta=1}^{6} e^{i\mathbf{k}\cdot\delta}$ is a geometric factor resulting from a sum over all nearest-neighbors δ of the triangular lattice. This dispersion corresponds to a longitudinal mode in the long-wavelength limit [75]. The remaining two modes, which are transversal for small momenta, are obtained from $\varepsilon_{\mathbf{k}+\mathbf{K}}$ and $\varepsilon_{\mathbf{k}+\mathbf{K}'}$. Note that along the high-symmetry line connecting the Γ to the M-point in the Brillouin zone, two of the three modes become degenerate. Close to the transition, one of the three modes develops a roton-like minimum around the M-point (not shown), which becomes soft at a critical value of $U_c/t \simeq 6.8$ [75, 77]. This indicates an instability of the ordered 120° phase, driven by out-of-plane fluctuations.

In the CSL phase, we also calculate the dynamical spin-structure factor. We describe the CSL by the Hamiltonian

$$H = -\frac{J}{2} \sum_{\substack{\langle ij \rangle \\ \alpha\beta}} f^{\dagger}_{i\alpha} f^{\dagger}_{j\beta} f_{i\beta} f_{j\alpha} \tag{3.2}$$

which is up to a constant simply the antiferromagnetic Heisenberg Hamiltonian expressed in terms of Abrikosov fermions $f_{i\sigma}$. In this parton description, spin liquids appear when the Abrikosov fermions propagate freely. This can be understood in terms of a mean-field decoupling, which yields the free spinon Hamiltonian [86, 89]

$$H_{\mathrm{sp}} = \sum_{\langle ij \rangle \sigma} J^{\mathrm{eff}}_{ij} f^{\dagger}_{i\sigma} f_{j\sigma}. \tag{3.3}$$

In the chiral spin liquid, the hopping $J^{\mathrm{eff}}_{ij} = -J \sum_{\sigma} \langle f^{\dagger}_{i\sigma} f_{j\sigma} \rangle$ is chosen such that each triangle of the lattice encloses a flux of $\pi/2$, which can be interpreted as a self-generated emergent magnetic field spontaneously breaking time-reversal symmetry. Due to the mean-field decoupling, there are two energy scales: the effective spinon hopping $J^{\mathrm{eff}} = |J^{\mathrm{eff}}_{ij}|$, which we keep fixed in our calculation, and the interaction energy between spinons given by Eq. (3.2). Both energies scale with $J \sim t^2/U$ and hence decrease with increasing U. Still, the relative value of the interaction strength between spinons compared to their effective kinetic energy, J/J^{eff}, increases as we approach the transition to the 120° state, implying more fluctuations around the mean-field state.

We again employ the RPA formalism to describe collective modes, describing quantum fluctuations around the mean-field spinon state through interactions given by Eq. (3.2). Similar approaches were recently applied in Refs. [90–93]. Including quantum fluctuations, we find a sharp collective mode below the continuum of two spinon excitations, as shown in panel (1) of Fig. 3.1b). The mode decays into the continuum close to the κ point and has a pronounced roton minimum at the K point, indicating short-range 120° antiferromagnetic correlations. By increasing the effective interaction strength J relative to the spinon hopping J^{eff}, the roton minimum becomes more pronounced and finally softens at a critical value of J_c, as seen in panel (2) of Fig. 3.1b). The closing of the spin gap at the K point indicates an instability towards an ordered phase with ordering wave vector K, which is precisely the ordering wave vector for the 120° phase. Therefore, the excited states of the chiral spin liquid not only carry information about the phase itself but also encode information about competing ordered phases. Using inelastic tunneling spectroscopy, as outlined in Sec. 2.3, we can directly study the mode softening at the transition between the CSL and the 120° phase. The critical exponent of the gap can hence be directly measured. Experimental observation of the roton mode and its softening would be strong evidence for the spin liquid phase and will reveal correlations relevant for a better understanding of the transition to the ordered state.

Note that by fixing the spinon hopping J_{ij}^{eff}, such that there is $\pi/2$ flux per triangle, we assume that the spin liquid remains gapped and neglect modifications of the spinon dispersion as the roton mode closes at the K point. For example, a Dirac spin liquid [88] might appear at the critical point or even as an extended critical phase. The Dirac spin liquid is characterized by Dirac cones in the spinon dispersion. In this case, the dynamical spin-structure factor exhibits a continuum of states down to zero frequency at the three distinct M points [94] due to the two Dirac cones, which are separated by lattice momentum M. This indicates the fractionalization of spin excitations, while a well-defined roton mode at the K point remains.

One possible challenge for inelastic tunneling spectroscopy is that only the portion of the Brillouin zone, where elastic tunneling is forbidden by energy-momentum conservation, can be measured, see Eq. (2.43). For the closing of the spin gap, which we predict will occur at the K and K' points, it should always be possible to experimentally tune the chemical potential such that only inelastic tunneling is possible at the points of interest. However, this may not be achievable when the relevant region is closer to the center of the Brillouin zone.

In a similar spirit, the QTM can be used to clarify the nature of the transition between the metallic phase and the GWC at fractional filling $\nu = 2/3$ discussed in the previous sections. In Refs. [95, 96], a continuous metal-insulator transition, driven either by doping or a displacement field, at half-filling was reported. In agreement with Ref. [67], we find that the transition from metal to GWC is first order on a mean-field level. The first derivative of the energy and the compressibility, which vanishes for the ordered phase, show a discontinuity at the transition to the metallic phase. By contrast, we observe the charge gap to open continuously, similarly to what was found in an exact diagonalization study [72], indicating that the transition from metal to insulator is not strongly first order. Further experimental and theoretical studies may help to clarify the situation.

Chapter 4

Tunneling in an external magnetic field

The chiral spin liquid phase discussed in the previous chapter can be stabilized by an external magnetic field [86]. This makes it interesting to explore the response of the QTM in finite magnetic fields, which has to account for Landau-level formation in the probing graphene layers. We consider a similar setup to the one discussed in Sec. 2.3: The tunneling current between two graphene sheets is measured as a function of the applied bias voltage and the relative twist angle, with the probe of interest sandwiched between the two graphene layers. Additionally, we now apply an external perpendicular magnetic field. This introduces a new length scale into our system: the magnetic length $\ell_B = \sqrt{\hbar/eB}$, which limits momentum resolution by $\delta k \sim 1/\ell_B \sim \sqrt{B}$. Consequently, we expect that for large enough magnetic fields, when the magnetic length is of the same order as the typical length scale of our probe, the quantum twisting microscope completely loses its momentum resolution. Intuitively, this can be understood as a consequence of the flattening of the Dirac cones in graphene due to the formation of relativistic Landau levels. Ideally, there will be an intermediate regime where the momentum space resolution is still sufficiently good to uniquely characterize the dynamical response functions of the probe while already stabilizing the phase of interest.

The low energy description of the $K = K^+$ ($K' = K^-$) valley of a monolayer graphene in an external gauge potential $\mathbf{A}(\mathbf{r})$ is given by [97, 98]

$$H_{K^\pm} = v_F(\pm\Pi_x\sigma^x + \Pi_y\sigma^y) \quad \text{with} \quad \mathbf{\Pi} = \mathbf{p} + e\mathbf{A} \tag{4.1}$$

Following Ref. [98], we introduce the relative twist angle θ between the two layers by a constant pseudo vector potential, which rotates the momenta. We adopt the following gauge

$$\mathbf{A}_\ell(\mathbf{r}) = \frac{1}{e}\left(\ell\Delta K_x^\pm, -eBx + \ell\Delta K_y^\pm, 0\right)^T \tag{4.2}$$

with the layer index $\ell \in \{\mathfrak{b}\hat{=}0, \mathfrak{t}\hat{=}1\}$. The eigenvalues of Eq. (4.1) are given by

$$\varepsilon_n = \mathrm{sgn}(n)\omega_c\sqrt{n} \tag{4.3}$$

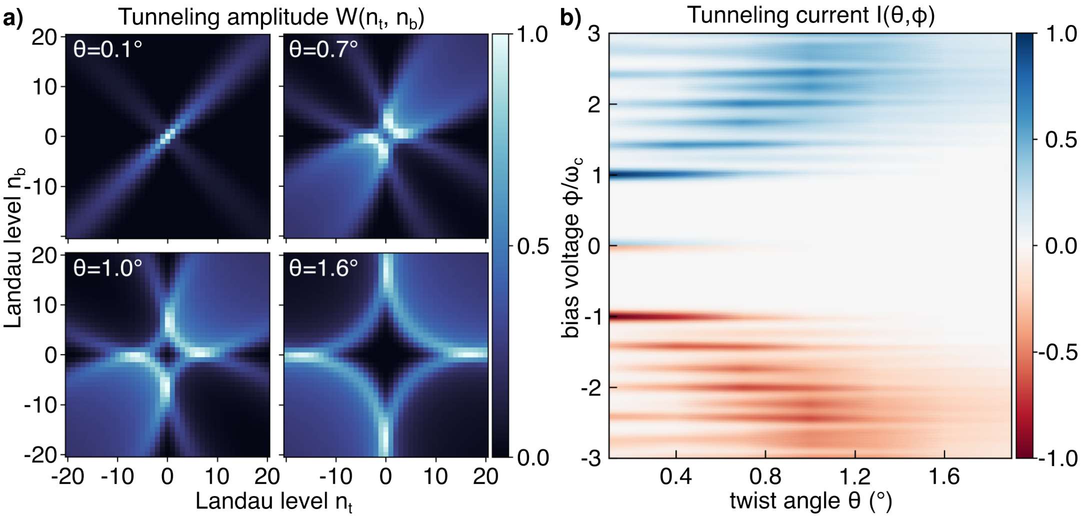

FIGURE 4.1: **Elastic tunneling in a magnetic field.** An external magnetic field (here $B = 4\text{T}$) leads to the formation of relativistic Landau levels in the top and bottom layer graphene. **a)** Normalized tunneling amplitudes between Landau level $n_\mathfrak{t}$ in the top layer and $n_\mathfrak{b}$ in the bottom layer for different twist angles. **b)** We consider elastic tunneling between two sheets of graphene separated by an insulating barrier. A bias voltage is applied between the graphene layers, and the system is placed in a perpendicular magnetic field. We show the elastic tunneling current as a function of the bias voltage ϕ and the twist angle θ. Both graphene layers are at charge neutrality.

with cyclotron frequency $\omega_c = \sqrt{2eB}v_F$ and the relativistic Landau-level index $n \in \mathbb{Z}$. The corresponding eigenstates are [98]

$$\begin{aligned}
\psi^+_{n,k_y}(\mathbf{r}) &= \frac{C_n}{\sqrt{L}} e^{ik_y y} \begin{pmatrix} \phi^{(\ell)}_{|n|}(x) \\ -\text{sgn}(n) i \phi^{(\ell)}_{|n|-1}(x) \end{pmatrix} \\
\psi^-_{n,k_y}(\mathbf{r}) &= \frac{C_n}{\sqrt{L}} e^{ik_y y} \begin{pmatrix} \text{sgn}(n) i \phi^{(\ell)}_{|n|-1}(x) \\ \phi^{(\ell)}_{|n|}(x) \end{pmatrix}
\end{aligned} \tag{4.4}$$

with $C_n = \sqrt{(1+\delta_{n,0})/2}$ and

$$\phi^{(\ell)}_n(x) = \frac{1}{\sqrt{2^n n! \sqrt{\pi} \ell_B}} \exp\left[-\frac{(x-X_\ell)^2}{2\ell_B^2} - i\ell\Delta K^\pm_x (x - X_\ell)\right] H_n(\frac{x - X_\ell}{\ell_B}) \tag{4.5}$$

where $H_n(x)$ are Hermite polynomials and $X_\ell = \ell_B^2(k_y + \ell\Delta K_y^\pm)$ is the x-component of the orbit center for the semiclassical cyclotron orbits. The quantum number k_y is indexing the degeneracy of each Landau level. The derivation of the tunneling current is analogous to the one presented in Sec. 2.1 and Sec. 2.3. We again assume that all layers are separated by some insulating barrier and only coupled through a tunneling Hamiltonian

$$H_{\text{tun}} = \sum_{\mathbf{r}_\mathfrak{t}, \mathbf{r}_\mathfrak{b}} \sum_{ab} \left(T_{ab}(\mathbf{r}_\mathfrak{t}, \mathbf{r}_\mathfrak{b}) c^\dagger_{\mathfrak{t}a}(\mathbf{r}_\mathfrak{t}) c_{\mathfrak{b}a}(\mathbf{r}_\mathfrak{b}) e^{i\phi t} + \text{h.c.}\right). \tag{4.6}$$

We take a tunneling matrix elements of the form

$$T_{ab}(\mathbf{r}_\mathfrak{t}, \mathbf{r}_\mathfrak{b}) = \hat{T}_{ab} \delta(\mathbf{r}_\mathfrak{t} - \mathbf{r}_\mathfrak{b}) \left[\Gamma_0 + \Gamma_1 \hat{O}(\mathbf{r}_\mathfrak{t})\right] \tag{4.7}$$

where $\hat{O}(\mathbf{r})$ is some operator that the electrons couple to when tunneling through the intermediate layer. Concretely, this operator might be the local magnetic moment or the local density, as discussed in Chapter 2. For simplicity, we take the tunneling amplitude between all sublattices to be equal, i.e., $\hat{T}_{ab} \sim \delta_{ab} + \sigma^x_{ab}$. First, we focus on the elastic contribution to the tunneling current, setting $\Gamma_1 = 0$. In the following, we restrict ourselves to the K valley. Analogous expressions can be derived for the K' valley. In the basis of the Landau level eigenfunction given by Eq. 4.4, the elastic tunneling Hamiltonian can be expressed as

$$H^{(0)}_{\text{tun}} = \sum_{n_\mathfrak{t},n_\mathfrak{b}} \sum_{k_\mathfrak{t},k_\mathfrak{b}} \left(T_{n_\mathfrak{t}n_\mathfrak{b}k_\mathfrak{t}k_\mathfrak{b}} c^\dagger_{\mathfrak{t}n_\mathfrak{t}k_\mathfrak{t}} c_{\mathfrak{b}n_\mathfrak{b}k_\mathfrak{b}} e^{i\phi t} + \text{h.c.} \right) \tag{4.8}$$

with

$$T_{n_\mathfrak{t}n_\mathfrak{b}k_\mathfrak{t}k_\mathfrak{b}} = \Gamma_0 \sum_{\mathbf{r}} \psi^*_{n_\mathfrak{t},k_\mathfrak{t}}(\mathbf{r}) \hat{T} \psi_{n_\mathfrak{b},k_\mathfrak{b}}(\mathbf{r}). \tag{4.9}$$

A similar calculation to the one presented in Sec. 2.1, yields an elastic tunneling current given by

$$I^{(0)}(\phi) = -2\pi e \sum_{n_\mathfrak{t},n_\mathfrak{b}} \sum_{k_\mathfrak{t},k_\mathfrak{b}} |T_{n_\mathfrak{t}n_\mathfrak{b}k_\mathfrak{t}k_\mathfrak{b}}|^2 \int \mathrm{d}\varepsilon \, \left[f_\mathfrak{t}(\varepsilon) - f_\mathfrak{b}(\varepsilon + \phi) \right] \mathcal{A}_\mathfrak{t}(\varepsilon, n_\mathfrak{t}) \mathcal{A}_\mathfrak{b}(\varepsilon + \phi, n_\mathfrak{b}). \tag{4.10}$$

where $\mathcal{A}_\ell(\varepsilon, n)$ is the spectral function of layer ℓ and Landau level n. In the disorder-free limit we can take $\mathcal{A}_\ell(\varepsilon, n) \sim \delta(\varepsilon - \varepsilon_n)$, which results in a current

$$I^{(0)}(\phi) = -2\pi e \sum_{n_\mathfrak{t},n_\mathfrak{b}} W(n_\mathfrak{t}, n_\mathfrak{b}) \left[f_\mathfrak{t}(\varepsilon_{n_\mathfrak{t}}) - f_\mathfrak{b}(\varepsilon_{n_\mathfrak{t}} + \phi) \right] \delta(\varepsilon_{n_\mathfrak{t}} - \varepsilon_{n_\mathfrak{b}} + \phi). \tag{4.11}$$

The dependence on the twist angle is implicitly contained in the tunneling amplitudes

$$W(n_\mathfrak{t}, n_\mathfrak{b}) = \frac{L^4}{(2\pi)^2} \int \mathrm{d}k_\mathfrak{t} \mathrm{d}k_\mathfrak{b} \, |T_{n_\mathfrak{t}n_\mathfrak{b}k_\mathfrak{t}k_\mathfrak{b}}|^2 \tag{4.12}$$

which describe the probability for an electron in the top layer in Landau level $n_\mathfrak{t}$ to tunnel to Landau level $n_\mathfrak{b}$ in the bottom layer. Explicit expressions for $W(n_\mathfrak{t}, n_\mathfrak{b})$ are given in Appendix D. In Fig. 4.1a), we plot $W(n_\mathfrak{t}, n_\mathfrak{b})$ for four different twist angles at a fixed magnetic field. For very small twist angles, the tunneling amplitude is peaked at transitions between the same Landau levels $|n_\mathfrak{t}| = |n_\mathfrak{b}|$. As we move to higher twist angles, the maxima of $W(n_\mathfrak{t}, n_\mathfrak{b})$ are shifted towards transitions between increasingly more separated Landau levels. This observation can be explained by a simple semiclassical picture [98]: the massless Dirac fermions of graphene perform cyclotron orbits in the presence of a magnetic field. The circular motion in real space induces orbital motion also in momentum space, with an orbital radius of $\kappa_n = \sqrt{2|n|}/\ell_B$. Due to the relative twist angle, the orbital center of the top layer is shifted by $\Delta K = 2K_D \sin(2\theta)$, where $K_D = |\mathbf{K}|$ is the position of the Dirac point of graphene. In this semiclassical picture, the tunneling amplitude between Landau levels is maximized if the fermion orbits touch each other, leading to the condition $\kappa_{n_\mathfrak{t}} \pm \kappa_{n_\mathfrak{b}} = \Delta K$. As the twist angle increases, the difference between the Landau levels must also increase to fulfill the condition. Increasing the magnetic field has the opposite effect since $\kappa_n \sim \sqrt{B}$.

In Fig. 4.1b) we show the elastic tunneling current as a function of the applied bias voltage and the twist angle, assuming both graphene layers are at charge neutrality. Pronounced plateaus corresponding to transitions between different Landau levels can be seen. The width of the plateaus scales inversely with the magnetic

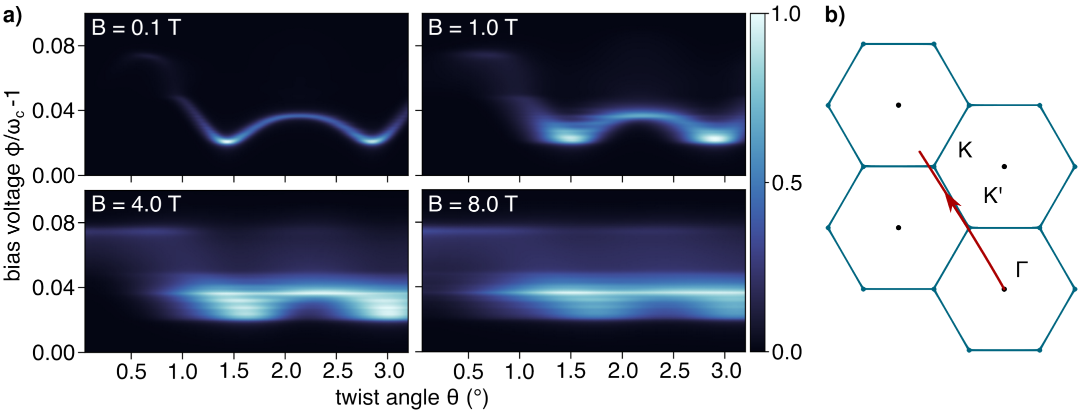

FIGURE 4.2: **Inelastic tunneling in a magnetic field.a)** Inelastic contribution to the tunneling current for an intermediate layer in the CSL phase, measuring the dynamical spin-structure factor $\mathcal{S}(\mathbf{k},\omega)$. We show $\mathcal{S}_{01}(\omega)$ for different magnetic fields as a function of the twist angle. Due to the formation of Landau levels in the top and bottom graphene layer, momentum space resolution decreases with increasing external field strength. Since $\mathcal{S}_{01}(\omega)$ corresponds to a tunneling process from the zeroth to the first Landau level, we shift the bias voltage by ω_c. In general, $\mathcal{S}_{nm}(\omega)$ gives contributions around a bias voltage of $(\sqrt{n}-\sqrt{m})\omega_c$. **b)** Cut through the Brillouin zone achieved by twisting from $\theta = 0°$ to $3.2°$, assuming a moiré lattice constant of $a_M = 10$ nm and $J_{\text{eff}} = 1$ meV.

length. Since the energy of Landau levels scales with $\varepsilon_n \sim \sqrt{|n|}$, the separation between consecutive Landau levels decreases as n increases. Consequently, only transitions between the first few Landau levels, where the separation $\Delta E = \varepsilon_{n_\mathfrak{t}} - \varepsilon_{n_\mathfrak{b}}$ is larger than the energy resolution, give a clean and unique signal to the tunneling current.

Information regarding collective excitations of the probe, sandwiched between the two graphene layers, can be extracted from the inelastic contribution to the tunneling current, proportional to $|\Gamma_1|^2$. An analogous derivation to the one presented in Sec. 2.3 leads to an inelastic tunneling current given by

$$I^{(2)}(\phi) = 2\pi e\Gamma_1^2 \sum_{n_\mathfrak{t} n_\mathfrak{b}} \left[n_\mathfrak{b}(\varepsilon_{n_\mathfrak{t}} - \varepsilon_{n_\mathfrak{b}} + \phi) - n_\mathfrak{b}(\varepsilon_{n_\mathfrak{t}} - \varepsilon_{n_\mathfrak{b}})\right]\left[f(\varepsilon_{n_\mathfrak{t}}) - f(\varepsilon_{n_\mathfrak{b}})\right] \times \mathcal{S}_{n_\mathfrak{t} n_\mathfrak{b}}(\varepsilon_{n_\mathfrak{t}} - \varepsilon_{n_\mathfrak{b}} + \phi) \tag{4.13}$$

with

$$\mathcal{S}_{n_\mathfrak{t} n_\mathfrak{b}}(\omega) = \frac{L^4}{(2\pi)^2 N} \int \mathrm{d}k_\mathfrak{t} \mathrm{d}k_\mathfrak{b} \sum_{\mathbf{k}} |\Psi_{\mathbf{k}}^{n_\mathfrak{t} k_\mathfrak{t}, n_\mathfrak{b} k_\mathfrak{b}}|^2 \mathcal{S}(\mathbf{k},\omega) \tag{4.14}$$

and

$$\Psi_{\mathbf{k}}^{n_\mathfrak{t} k_\mathfrak{t}, n_\mathfrak{b} k_\mathfrak{b}} = \frac{1}{L^2} \int \mathrm{d}^2 r\, \psi^*_{n_\mathfrak{t}, k_\mathfrak{t}}(\mathbf{r}) e^{i\mathbf{k}\cdot\mathbf{r}} \psi_{n_\mathfrak{b}, k_\mathfrak{b}}(\mathbf{r}). \tag{4.15}$$

Here, $n_\mathfrak{b}(\varepsilon)$ is the Bose-Einstein distribution, and $f(\varepsilon)$ is the Fermi-Dirac distribution. Their only effect in Eq. 4.13 is ensuring that only energetically allowed transitions between an empty and a filled Landau level contribute to the current. Both top and bottom-layer graphene are held at charge neutrality. We see that the inelastic tunneling current still measures the dynamical structure factor

$$\mathcal{S}(\mathbf{k},\omega) = -i \int_0^\infty \mathrm{d}t\, e^{i\omega t} \left\langle [\hat{O}_{\mathbf{k}}(t), \hat{O}_{-\mathbf{k}}(0)] \right\rangle \tag{4.16}$$

but expressed in the Landau level basis. Explicit expressions for the coefficients of Eq. (4.15) are given in Appendix D. The twist angle dependence is implicitly contained in $\mathcal{S}_{n_\mathfrak{t} n_\mathfrak{b}}(\omega)$. In Fig. 4.2, we show the inelastic contribution to the tunneling current for the transition between the zeroth and first Landau level for different magnetic fields, measuring the dynamical spin-structure factor of a CSL. Since the primary objective of this section is to characterize the response of the QTM in an external magnetic field, we assume a fixed $\mathcal{S}(\mathbf{k}, \omega)$ independent of the magnetic field. The typical energy scale of the probe must be much smaller than the cyclotron frequency ω_c, such that different $\mathcal{S}_{n_\mathfrak{t} n_\mathfrak{b}}(\omega)$ give contributions at vastly different bias voltages and can thus be probed independently. We expect that this only holds for the first few Landau levels before their separation becomes smaller than the typical energy scale of the probe. As expected, one can see in Fig. 4.2 that for small magnetic fields, the sharp collective mode of the CSL is still visible with good momentum resolution. As the magnetic field is increased, momentum resolution is lost. Nonetheless, even at a magnetic field of $B = 8$ T, the signal is strongest at the K and K', a remnant of the fact that the collective mode has its minima there. We conclude that the QTM can still provide useful momentum-resolved information about collective modes at finite magnetic fields.

Chapter 5

Quantum anomalous Hall effect

5.1 Integer quantum anomalous Hall state

While the presence of integer quantum anomalous Hall (IQAH) states in TMD heterostructures has been established both theoretically and expeimentally [10, 15–17, 19, 21, 23], their excitation spectra remain largely unexplored. We present both the single-particle and collective spectrum of an IQAH state, modeled by a Kane-Mele model with onsite interactions on a honeycomb lattice, as derived in Sec. 1.4.2

$$H = H_{\mathrm{KM}} + U \sum_i n_{\uparrow i} n_{\downarrow i} \tag{5.1}$$

where H_{KM} is given by Eq. (1.13). We fix the filling at $\nu = 1$ electrons per unit cell, corresponding to an average density of half a particle per site. The spin index refers to the locked spin-valley degree of freedom. We include hopping terms up to the fifth nearest neighbor, ensuring an accurate fit to the band structure from the continuum model Eq. (1.10). If not otherwise specified, we use the following hopping parameters: $(t_1, t_2, t_3, t_4, t_5) = (1.00, 0.26, -0.06, 0.04, -0.02)$ in units of $t_1 \equiv t$. Except for the nearest neighbor hopping, all hopping amplitudes are purely real. The model Eq. (5.1) is symmetric under time reversal, consisting of two copies of the Haldane model, related by time-reversal symmetry. For interaction strengths U smaller than the bandwidth of the lowest-lying band, the spin up ($C = +1$) and spin down ($C = -1$) Chern bands of the Kane-Mele model are degenerate. The two Chern bands with opposite Chern numbers are half-filled each, leading to a topologically trivial metallic state. Once the interaction strength exceeds the bandwidth, the system spontaneously breaks time-reversal symmetry, forming an IQAH state [23]. The strong onsite interaction leads to an effective Zeeman splitting between the spin-up and spin-down band, where the Zeeman gap scales with U. Consequently, we find a spin/valley polarized state, where now only one Chern band is fully filled. Experimentally, an important tuning knob is the application of a displacement field Δ. Since the two sublattices of the honeycomb lattice physically live in two different layers of the TMD bilayer, a displacement field acts as a staggered sublattice potential

$$H_\Delta = \frac{\Delta}{2} \sum_{i\sigma} (c^\dagger_{A\sigma i} c_{A\sigma i} - c^\dagger_{B\sigma i} c_{B\sigma i}). \tag{5.2}$$

By increasing the displacement field Δ for fixed U, the system undergoes a topological phase transition from an IQAH state to a trivial insulator [23, 99]. In the limit of very large displacement fields and interactions strengths $U, \Delta \gg t$, one sublattice effectively gets projected out, and one finds a trivial Mott state on a triangular lattice formed by the remaining sublattice. A mean-field phase diagram is shown in Fig. 5.1b). Consistent with previous mean-field studies [23], we find that the trivial

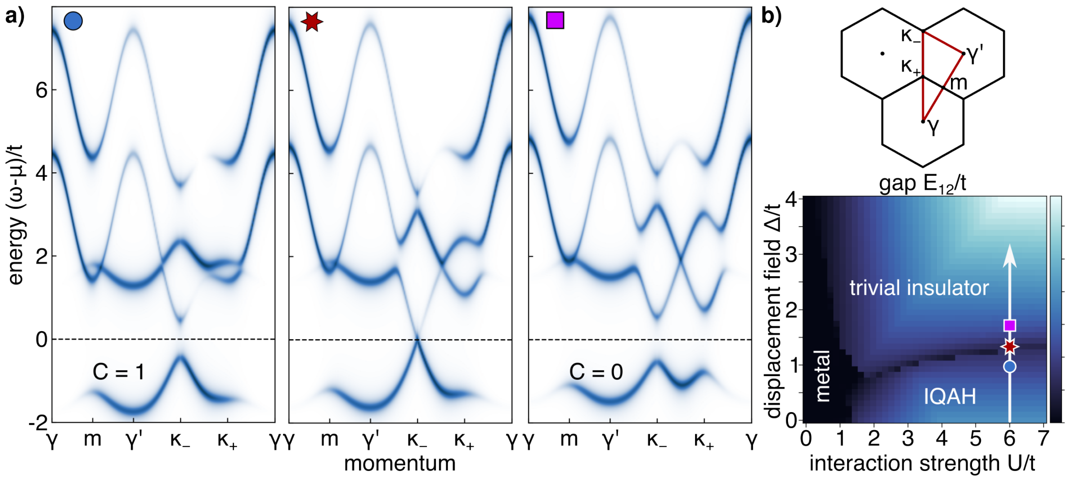

FIGURE 5.1: **Single-particle spectral function across topological phase transition.** **a)** Sufficiently large interaction strength U leads to spontaneous valley polarization and an IQAH state, where the lowest band is completely filled and has Chern number $C = 1$. By increasing the displacement field Δ, the system undergoes a topological phase transition to a trivial insulator. At the critical point, the single-particle gap closes. Left: IQAH phase. Center: critical point. Right: trivial insulator. **b)** Top: Cut through the three inequivalent Brillouin zones. Bottom: Single particle gap as a function of the interaction strength and the displacement field. The three points shown in **a)** are highlighted.

insulator is still ferromagnetic but with an in-plane polarization. Note that the nontrivial next-nearest neighbor hopping in Eq. (1.13) explicitly breaks the spin $\mathrm{SU}(2)$ symmetry down to an $\mathrm{U}(1)$ symmetry, making the distinction between in-plane and out-of-plane polarization physically meaningful.

Using the QTM to measure the single-particle spectral function, one can characterize the topological phase transition induced by a displacement field Δ. In Fig. 5.1a) we show the single-particle spectral function, calculated using self-consistent Hartree-Fock, for three points in the phase diagram. As expected, both the IQAH state and the trivial insulator show a gapped band on the hole side of the spectral function. At the critical point, the gap closes at either the κ_+ or κ_- point in the Brillouin zone, depending on the polarization of the IQAH state. The $\kappa_\pm$ points are defined in Fig. 5.1b).

The QTM should, therefore, provide a direct measurement of the single particle gap, which makes it possible to detect the phase transition induced by increasing the displacement field Δ.

Next, we discuss the collective excitation spectra, which are accessible by inelastic tunneling spectroscopy with the QTM. We calculate the dynamical spin-structure factor of the IQAH state using the RPA formalism discussed in Appendix B. Representative results are shown in Fig. 5.2. The total dynamical spin-structure factor, as shown in Fig. 5.2b), contains both spin and density excitations. We first discuss the spin modes, as shown in the lower panel of Fig. 5.2a). There are three modes: a low-lying magnon branch, with a small gap stemming from the explicit breaking of the $\mathrm{SU}(2)$ spin symmetry of the Kane-Mele model, and a higher-lying branch, whose gap scales with the interaction strength U. Since we have an average electron density of half a particle per site, we cannot map our model in the low-energy regime to a pure spin Hamiltonian. To gain a better understanding of the observed spin modes, we employ the adiabatic approximation [100], where it is assumed that the

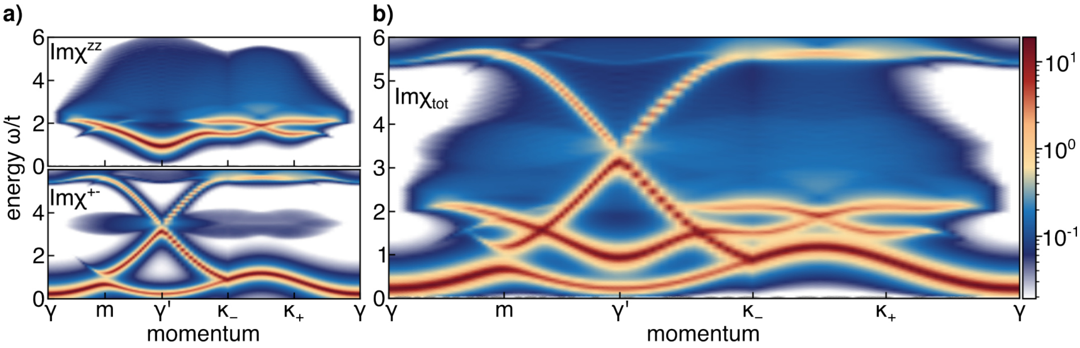

FIGURE 5.2: **Dynamical spin-structure factor in IQAH phase. a)** Top: The density response shows a gapped mode emerging from the continuum with a roton minimum at γ', indicating correlations towards a charge density wave phase. Bottom: Transverse spin response with a low-lying magnon-branch and a higher-lying mode, which we interpret as doublon bound states. **b)** The total dynamical spin-structure factor as measured by the QTM. It contains both the density and spin modes. The shown plots are for $U = 7t$ and $\Delta = 0$

spin physics decouples from the itinerant electron motion, allowing for a description using an effective spin Hamiltonian. The adiabatic approximation is valid if the typical time scale of the spin physics is much larger than the fast-moving electronic motion. Since the Kane-Mele model explicitly breaks SU(2) spin symmetry, we expect the effective spin Hamiltonian governing the low-lying spin excitations to be a ferromagnetic XXZ model

$$H^{\text{eff}}_{\text{XXZ}} = -\sum_{\langle ij\rangle} \left[J_z S_i^z S_j^z + J_\perp (S_i^x S_j^x + S_i^y S_j^y) \right] \tag{5.3}$$

with $J_z > J_\perp > 0$. The linear spin-wave theory of Eq. (5.3) can accurately describe the two lowest-lying magnon modes. The gap of the lowest mode is found to scale with $J_z - J_\perp \sim t_2$, which is expected, as it is the next-nearest neighbor hopping term breaking the SU(2) spin symmetry down to U(1). A more quantitative description of the two lower modes can be obtained using a bosonization approach [101–103], as outlined in Appendix C.2. The nature of the upper mode in the transverse spin response is less clear. Its gap scales with U, which leads us to interpret it as doublon bound states: a spin-flip in combination with hopping to a neighboring site.

The transverse spin response of a topological trivial ferromagnetic metal looks qualitatively similar to the spin response of the IQAH state we have found. Consequently, we do not expect it to be a relevant signature of the IQAH state. The density response, as shown in the upper panel of Fig. 5.2a) is a more distinctive characteristic of the IQAH state. We observe a gapped density mode emerging from the continuum with a roton minimum at the γ' point. As the interaction strength is increased, the minimum becomes more pronounced until the roton mode softens at a critical $U_c \approx 7.78t$. We interpret this as an instability of the IQAH state, possibly towards a charge density wave. We remark on the qualitative similarity between the spin response in the CSL phase discussed in Sec. 3 and the density response in the IQAH phase. This contrasts the density response of topologically trivial competing states: The density response of a topologically trivial itinerant ferromagnet is the usual gapless Lindhard function, while the density response in the Mott insulator for large displacement fields Δ consists of a gapped particle-hole continuum. We conclude that the gapped roton mode is a distinctive feature of the topologically nontrivial IQAH

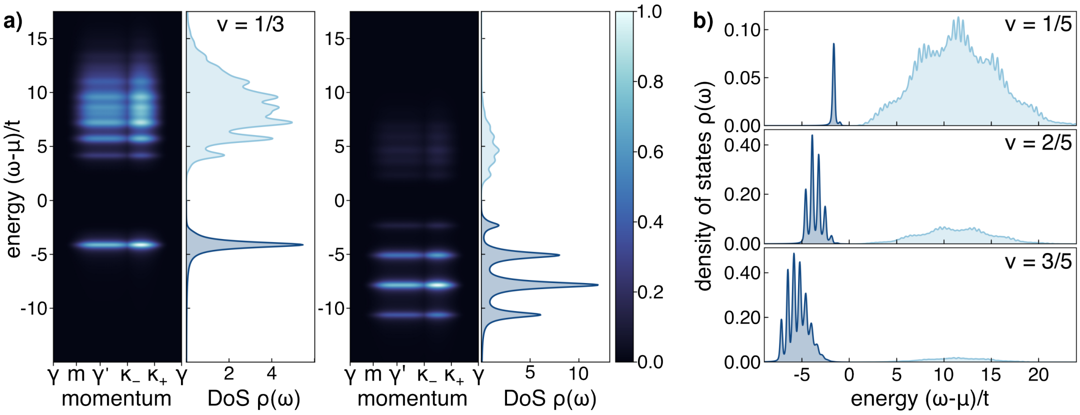

FIGURE 5.3: **Single-particle spectral function of FQAH states. a)** The spectral function and corresponding density of states (DoS) for filling $\nu = 1/3$ ($\nu = 2/3$) on the left (right) shows clear signs of fractionalization. There is a striking difference between the hole and particle side: while there are still sharp peaks visible on the hole side, the particle side consists of a broad continuum with small peaks on top. **b)** Density of states for the fillings $\nu \in \{1/5, 2/5, 3/5\}$. As the filling increases, the spectral weight on the particle side decreases.

state. The QTM measures the complete dynamical spin-structure factor as shown in Fig. 5.2b), where there is an overlap between the spin and density modes. By applying an external magnetic field, the spin modes can be further gapped out to higher energies while the density mode remains unaffected by an external Zeeman field. In that way, the more interesting density response can be probed independently. Note, however, that the external field cannot be too large, as the QTM loses its momentum resolution otherwise, as discussed in Sec. 4.

5.2 Fractional quantum anomalous Hall states

So far, we have focused on a filling of $\nu = 1$ electrons per unit cell, where an IQAH state is realized. While topologically nontrivial, the electron remains a well-defined quasiparticle, and most of the physics can be understood on a single-particle level. Interactions were only necessary to introduce an effective Zeeman splitting, leading to spin/valley polarization. This changes when we go to a fractional filling of the unit cell, where fractional quantum anomalous Hall (FQAH) states, also known as fractional Chern insulators [104, 105], where predicted to occur in TMD heterostructures [34–37, 40, 41]. Similarly to the conventional fractional quantum Hall effect, in an FQAH state, the electron fractionalizes in quasiparticles carrying a fraction of the electron charge and following anyonic exchange statistics [104, 106]. Such a highly correlated state can no longer be understood using a naive mean-field description of the model Eq. (5.1). Instead, we use a parton description to calculate the single-particle spectral function. For simplicity, we neglect the spin degree of freedom, assuming that interactions lead to a spontaneous spin/valley polarization, which a small external magnetic field can further stabilize. Furthermore, we project to the lowest Chern band, which we assume to be sufficiently flat to host FQAH states. The spin-up sector of the single-particle Hamiltonian H_{KM} given by Eq. (1.13), can be written in its eigenbasis

$$H^{\uparrow}_{\mathrm{KM}} = \sum_{\mathbf{k}} \sum_{\lambda \in \{\pm\}} \varepsilon^{\lambda}_{\mathbf{k}} \gamma^{\dagger}_{\lambda \mathbf{k}} \gamma_{\lambda \mathbf{k}} \tag{5.4}$$

with the electron operator on sublattice $a \in \{A, B\}$ given by $c_{a\mathbf{k}} = u_{a+,\mathbf{k}}\gamma_{+,\mathbf{k}} + u_{a-,\mathbf{k}}\gamma_{-,\mathbf{k}}$. The projected electron operator can be written as $\bar{c}_{a\mathbf{k}} = u_{a-,\mathbf{k}}\gamma_{-,\mathbf{k}} \equiv u_{a,\mathbf{k}}\gamma_{\mathbf{k}}$. Focusing on a filling of $\nu = 1/3$, we write the γ operator as a product of three fermionic partons [106, 107]

$$\gamma(\mathbf{r}) = f_1(\mathbf{r})f_2(\mathbf{r})f_3(\mathbf{r}) = \frac{1}{3!}\varepsilon_{\alpha\beta\gamma}f_\alpha(\mathbf{r})f_\beta(\mathbf{r})f_\gamma(\mathbf{r}) \tag{5.5}$$

each carrying an electric charge $e^* = e/3$. This construction introduces a gauge degree of freedom, since Eq. (5.5) is invariant under local SU(3) transformations $f_\alpha(\mathbf{r}) \to G_{\alpha\beta}(\mathbf{r})f_\beta(\mathbf{r})$ with $G(\mathbf{r}) \in \mathrm{SU}(3)$. Furthermore, we have the constraint

$$n_c = n_{f_1} = n_{f_2} = n_{f_3}. \tag{5.6}$$

The additional gauge degree of freedom can be used to construct a gapped state even at fractional filling of the unit cell. To that end, we describe the partons using a mean-field ansatz

$$H_{m=3} = \sum_{i,j}\sum_{\alpha=1}^{3} t_{ij} f_\alpha^\dagger(\mathbf{r}_i) f_\alpha(\mathbf{r}_j) \tag{5.7}$$

where we have assumed that different flavors of partons do not mix. We enforce the constraint Eq. (5.6) on a mean-field level. Our goal is to choose a parton mean-field ansatz whose lowest band is gapped and has a Chern number of $C = +1$. If we then fill up this lowest band for each parton flavor, we end up with the desired Hall conductivity of

$$\sigma_{xy} = 3\frac{(e^*)^2}{2\pi\hbar} = \frac{1}{3}\frac{e^2}{2\pi\hbar}. \tag{5.8}$$

Due to the additional gauge degree of freedom, the parton mean-field ansatz can break the lattice symmetries U, as long as it is invariant under a combination of U and some local gauge transformation $G_{\mathrm{U}}(\mathbf{r})$ [106]. Explicitly, we can insert $2\pi/3$ flux per primitive unit cell to triple the unit cell and construct a parton mean-field state with the desired properties. Additional details and an explicit example for such a parton mean-field ansatz are given in Appendix E. As shown in Appendix E, the projected single-particle spectral function of the FQAH state is given by

$$\begin{aligned}\bar{\mathcal{A}}(\mathbf{k},\omega) = \int \mathrm{d}\mathbf{q}\mathrm{d}\mathbf{p} \int \mathrm{d}\varepsilon\mathrm{d}\varepsilon'\, \mathcal{A}_1(\mathbf{q},\varepsilon)\mathcal{A}_2(\mathbf{p}-\mathbf{q},\varepsilon'-\varepsilon)\mathcal{A}_3(\mathbf{k}-\mathbf{p},\omega-\varepsilon') \\ \times [n_F(\varepsilon) + n_B(\varepsilon-\omega)][n_F(\varepsilon'-\varepsilon) - n_F(\varepsilon'-\omega)]\end{aligned} \tag{5.9}$$

where $\mathcal{A}_\alpha(\mathbf{k},\omega)$ is the spectral function of the parton f_α, $n_F(\varepsilon)$ is the Fermi-Dirac distribution, and $n_B(\varepsilon)$ is the Bose-Einstein distribution. The projected electronic spectral function is not simply the convolution of the parton spectral functions. The additional factors of Fermi-Dirac and Bose-Einstein distributions ensure that the particle and hole part of the spectral function are not mixed. Physically, this can be understood from the fact that in a tunneling process, one always adds or removes a whole electron, meaning that one must either add three or remove three partons. Without the additional factors, one would have contributions to the total spectral function where, for example, a single parton is added and two partons are removed. The full electronic spectral function, as measured in experiments, is

$$\mathcal{A}(\mathbf{k},\omega) = \sum_{ab} e^{-i\mathbf{k}\cdot(\mathbf{r}_a-\mathbf{r}_b)} u_{a,\mathbf{k}} u_{b,\mathbf{k}}^* \bar{\mathcal{A}}(\mathbf{k},\omega) \equiv Z_{\mathbf{k}}\bar{\mathcal{A}}(\mathbf{k},\omega). \tag{5.10}$$

where $\mathbf{r}_a$ is the position of site a within the unit cell. The additional factor $Z_{\mathbf{k}}$ shifts the spectral weight, taking both the projection to the lowest Chern band and the lattice structure into account. Note that the spectral function Eq. (5.10) does not fulfill the sum rule, since we neglect processes involing higher Chern bands. To describe the FQAH state at $\nu = 2/3$ we construct a parton mean-field state where the two lowest bands have Chern number $C = +1$ and fill them up. Analogous constructions can also be carried out at filling $\nu \in \{1/5, 2/5, 3/5\}$, as outlined in Appendix E. In that case, Eq. (5.9) must also be adapted.

We show our results for the single-particle spectral function at various fractional fillings in Fig. 5.3. As a consequence of the momentum convolution in Eq. (5.9), the only momentum dependence of the spectral function is contained in $Z_{\mathbf{k}}$. Consequently, we focus our discussion on the density of states $\rho(\omega) = \sum_{\mathbf{k}} \mathcal{A}(\mathbf{k}, \omega)/N$. We find qualitatively similar results to Refs. [108, 109], in which the density of states for conventional fractional quantum Hall states is calculated, and Ref. [110], where the local density of states of various fractional quantum Hall states is measured. At a filling of $\nu = 1/3$, we see a single sharp peak on the hole side of the spectral function, lying at an energy $E = 3E_0$, where E_0 is the energy of the filled parton band. This can be understood as follows: Since there is only one filled parton band for each flavor, removing three partons from the same band is the only way to add a hole to the system. The response on the particle side is qualitatively different. It consists of a broad continuum with small peaks on top. Since there are many empty parton bands above the one filled band, the many combinations of adding three partons result in a much broader signal. This asymmetry between the particle and hole part of the spectral function is retained at a filling of $\nu = 2/3$. The hole side now hosts four distinct peaks, corresponding to the four independent ways one can remove three partons from the two filled bands, while the particle side consists of a broader continuum. In Fig. 5.3b), we see that the same qualitative behavior applies to FQAH states with five partons. There appears to be a general trend, where the spectral weight on the particle side of the spectral function decreases as we fill up more parton bands. While the quantitative details of our results, presented in Fig. 5.3, depend on the precise mean-field ansatz, the qualitative behavior does not. We have calculated the spectral function for various mean-field parameters, all yielding the same quantized Hall conductivity. They all look qualitatively the same, with Fig. 5.3 being a representative example.

We perform exact diagonalization calculations to verify the validity of the parton description of the FQAH states. Concretely, we project onto a Chern band at $\nu = 1/3$ filling and add nearest neighbor density-density interactions. Such a model has been shown to host FQAH states [104, 105, 111]. The resulting projected spectral function and density of states are in excellent agreement with the results obtained through the parton description. Details of the exact diagonalization calculation are given in Appendix E.1.

We have shown how the QTM can be used to characterize the excitations of FQAH states. The complete lack of dispersing bands and the characteristic particle-hole asymmetry, with only a continuum on the particle side, are distinctive signs of fractionalization. These signatures distinguish FQAH states from competing states, such as Fermi liquids and charge density waves. Furthermore, experimentally observing spectra in agreement with our prediction would verify that the parton description we used accurately captures the fundamental aspects of the FQAH states.

Chapter 6

Conclusions and Outlook

This work demonstrates how the QTM can characterize strongly correlated phases of matter in two dimensions, ranging from ordered (anti-)ferromagnets to quantum spin liquids and quantum anomalous Hall states. In particular, we focus on antiferromagnetic and ferromagnetic generalized Wigner crystals on a triangular moiré lattice. There is also the possibility that the nearest-neighbor effective spin coupling vanishes and the state does not magnetically order. In that case, we expect no well-defined spin-wave modes in the inelastic tunneling spectroscopy signal. For concreteness, we focused on a fractional filling of $\nu = 2/3$ electrons per site, but GWCs have been observed for a wide range of other fillings [2, 3, 5–7]. We expect the QTM to also distinguish between different types of magnetic order in these other cases.

Due to intrinsically strong interactions in atomically thin TMDs, crystalline states can form even in the absence of an induced moiré potential [53, 112]. While such Wigner crystals have a long history, their spin order, as well as their charge order close to the crystallization transition, are still investigated [26–28, 30, 113]. Moreover, first-order crystallization transitions are forbidden in this regime due to long-range interactions and replaced by more exotic intermediate phases [114, 115]. It will be interesting to generalize our analysis to these systems, as the QTM offers a new opportunity to directly probe the exotic properties of melting transitions in the two-dimensional electron gases. We also remark that systems with weak moiré potentials [3] at low fillings may serve as a controlled starting point.

Exotic superconductivity in strongly correlated regimes appears in various two-dimensional heterostructures with and without moiré potential [116–119]. These superconducting states often appear close to ordered states [118, 120]. Data from elastic and inelastic scattering via the QTM may help shed light on the collective modes that drive superconductivity in these systems.

As discussed in Sec. 1.4.2, moiré heterostructures can host topologically non-trivial bands, allowing for the emergence of the interaction-induced integer and fractional quantum anomalous Hall effect [11, 13, 21, 23, 36–38, 40]. We have shown that the single-particle response shows direct signs of electron fractionalization in the fractional quantum anomalous Hall state. Since an external magnetic field stabilizes these anomalous Hall states, the formalism we developed in Sec. 4 to describe the response of the QTM in a perpendicular magnetic field will prove useful. The collective excitation spectrum of fractional quantum anomalous Hall states is still unexplored. We expect it to contain critical insights into the correlations of these states and the critical behavior close to neighboring states, such as charge density waves. It has been proposed that scanning tunneling microscopy can directly image non-Abelian anyons in fractional quantum Hall states in the presence of impurity defects [121]. It will be interesting to explore if this generalizes to fractional quantum anomalous Hall states and if the momentum resolution of the QTM can be used to extract additional information.

Appendix A

Mean-field theory

A.1 Mean-field theory

The matrix $h_{\mathbf{k}}$ in spinor space in Eq. (2.29) is given by

$$[h^{(t)}_{\mathbf{k}}]_{ab,\sigma\sigma'} = -t\gamma^{ab}_{\mathbf{k}}\delta_{\sigma\sigma'} \tag{A.1}$$

$$[h^{(u)}_{\mathbf{k}}]_{ab,\sigma\sigma'} = U\delta_{ab}\chi^{ab}_{\sigma\sigma'}(\delta_{\sigma\sigma'} - \sigma^{x}_{\sigma\sigma'}) \tag{A.2}$$

$$[h^{(v)}_{\mathbf{k}}]_{ab,\sigma\sigma'} = V\big[3(n-n_a)\delta_{ab}\delta_{\sigma\sigma'} - \gamma^{ab}_{\mathbf{k}}\chi^{ba}_{\sigma'\sigma}\big] \tag{A.3}$$

$$[h^{(x)}_{\mathbf{k}}]_{ab,\sigma\sigma'} = X\big[3\big(\chi^{ab}_{\sigma'\sigma} - \sum_c \chi^{cc}_{\sigma'\sigma}\big)\delta_{ab} + \gamma^{ab}_{\mathbf{k}}\delta_{\sigma\sigma'}\sum_\alpha \chi^{ba}_{\alpha\alpha}\big] \tag{A.4}$$

with $n_a = \chi^{aa}_{\uparrow\uparrow} + \chi^{aa}_{\downarrow\downarrow}$ and $n = \sum_a n_a$. For the nearest-neighbor geometric factor $\gamma^{ab}_{\mathbf{k}}$ one finds

$$\gamma^{AB}_{\mathbf{k}} = 1 + e^{i\mathbf{b}_1\cdot\mathbf{k}} + e^{i(\mathbf{b}_1+\mathbf{b}_2)\cdot\mathbf{k}} \tag{A.5}$$

$$\gamma^{AC}_{\mathbf{k}} = 1 + e^{i\mathbf{b}_2\cdot\mathbf{k}} + e^{i(\mathbf{b}_1+\mathbf{b}_2)\cdot\mathbf{k}} \tag{A.6}$$

$$\gamma^{BC}_{\mathbf{k}} = 1 + e^{-i\mathbf{b}_1\cdot\mathbf{k}} + e^{i\mathbf{b}_2\cdot\mathbf{k}} \tag{A.7}$$

and $\gamma^{aa}_{\mathbf{k}} = 0 \ \ \forall\, a \in \{A, B, C\}$, $\gamma^{ba}_{\mathbf{k}} = (\gamma^{ab}_{\mathbf{k}})^*$. The vectors $\mathbf{b}_{1/2}$ span the unit cell and are defined in Fig. 2.1b). The following constant energy shift is obtained

$$\begin{aligned} E_0 = &-UN\sum_a \big(\chi^{aa}_{\uparrow\uparrow}\chi^{aa}_{\downarrow\downarrow} - \chi^{aa}_{\uparrow\downarrow}\chi^{aa}_{\downarrow\uparrow}\big) + \\ &+ \frac{VN}{2}\sum_{ab}\sum_{\sigma\sigma'}\gamma^{ab}_{\mathbf{k}=0}\big(|\chi^{ab}_{\sigma\sigma'}|^2 - \chi^{aa}_{\sigma\sigma}\chi^{bb}_{\sigma'\sigma'}\big) + \\ &+ \frac{XN}{2}\sum_{ab,\sigma}\gamma^{ab}_{\mathbf{k}=0}\big(\chi^{ab}_{\sigma\sigma}\chi^{ba}_{\bar\sigma\bar\sigma} - \chi^{aa}_{\bar\sigma\sigma}\chi^{bb}_{\sigma\bar\sigma}\big). \end{aligned} \tag{A.8}$$

The mean-field result for the retarded single-particle Green's function of Eq. (2.31) is given by

$$\mathcal{G}^{(0)}(\mathbf{k},\omega) = \sum_{\mu=1}^{6}\frac{Z^{\mu}_{\mathbf{k}}}{\omega - \varepsilon^{\mu}_{\mathbf{k}} + i\eta}, \tag{A.9}$$

where $\varepsilon^{\mu}_{\mathbf{k}}$ are the eigenvalues of the mean-field matrix $h_{\mathbf{k}}$ and $Z^{\mu}_{\mathbf{k}}$ is the following function of the eigenvector projections $\alpha^{\mu}_{a\sigma\mathbf{k}}$

$$Z^{\mu}_{\mathbf{k}} = \sum_{\sigma,ab} e^{-i\mathbf{k}\cdot(\mathbf{r}_a-\mathbf{r}_b)}\alpha^{\mu}_{a\sigma\mathbf{k}}(\alpha^{\mu}_{b\sigma\mathbf{k}})^* \tag{A.10}$$

with $\mathbf{r}_a$ describing the position of sublattice a within the unit cell.

A.2 Effective hopping in MF background

In the AFM, the dispersion of both particle bands and the hole band is described as a free particle, with hopping restricted to the initial sublattice it has been placed on since the other two sublattices are inaccessible either due to energy conservation or the Pauli principle.

The effective hopping parameters can be computed using perturbation theory for $U \gg V$ and $X = 0$. For particles hopping on a triangular lattice spanned by the two vectors $\mathbf{b}_{1/2}$, they are given by

$$t_1^{(\text{eff})} = \frac{3t^2}{6V} + \frac{3t^2}{2(3V-U)} + \frac{18t^3}{3V(3V-U)} + \cdots \tag{A.11}$$

$$t_2^{(\text{eff})} = -\frac{3t^2}{2U} - \frac{3t^2}{2(U-3V)} + \frac{18t^3}{U(U-3V)} + \cdots \tag{A.12}$$

$$t_0^{(\text{eff})} = \frac{3t^2}{6V} + \frac{3t^2}{2U} + \frac{6t^3}{UV} + \cdots \tag{A.13}$$

where $t_1^{(\text{eff})}$ and $t_2^{(\text{eff})}$ correspond to the upper and lower particle band respectively and $t_0^{(\text{eff})}$ describes the hole band. For the ferromagnet, the two topmost particle bands and the two hole bands correspond to leading order to free hopping on a hexagonal lattice with hopping parameter t. The remaining two particle bands can be understood as free hopping on a triangular lattice and effective hopping parameters

$$t_1^{(\text{eff})} = -\frac{2t^2}{2V-X} + \frac{4t^3}{(2V-X)^2} + \cdots \tag{A.14}$$

$$t_2^{(\text{eff})} = \frac{6t^2}{2U-6V-3X} + \frac{36t^3}{(2U-6V-3X)^2} + \cdots \tag{A.15}$$

assuming $U \gg V, X$.

Appendix B

Random Phase Approximation

To incorporate quantum fluctuations on top of mean-field states, we use the random phase approximation (RPA) to calculate the spin- and density response functions. We consider a generic interaction Hamiltonian for fermions

$$H_{\text{int}} = \frac{1}{N} \sum_{\mathbf{k},\mathbf{k}',\mathbf{q}} \sum_{\alpha\beta\gamma\delta} V_{\alpha\beta\gamma\delta}(\mathbf{q}) c^\dagger_{\alpha\mathbf{k}+\mathbf{q}} c^\dagger_{\beta\mathbf{k}'-\mathbf{q}} c_{\gamma\mathbf{k}'} c_{\delta\mathbf{k}} \tag{B.1}$$

where Greek indices can be both spin and sublattice and N is the number of unit cells. We calculate the generic response function

$$\chi_{\alpha\beta\gamma\delta}(\mathbf{q}, i\omega_n) = \frac{1}{2} \int_0^\beta \mathrm{d}\tau \, e^{i\omega_n \tau} \sum_{\mathbf{k},\mathbf{k}'} \left\langle \mathcal{T} c^\dagger_{\alpha\mathbf{k}}(\tau) c_{\beta\mathbf{k}+\mathbf{q}}(\tau) c^\dagger_{\gamma\mathbf{k}'}(0) c_{\delta\mathbf{k}'-\mathbf{q}}(0) \right\rangle \tag{B.2}$$

which can be expressed in terms of the single-particle Green's function $\mathcal{G}_{\alpha\beta}(\mathbf{k},\tau) = -\left\langle \mathcal{T} c_{\alpha\mathbf{k}}(\tau) c^\dagger_{\beta\mathbf{k}}(0) \right\rangle$ as

$$\chi_{\alpha\beta\gamma\delta}(\mathbf{q}, i\omega_n) = -\frac{1}{2\beta} \sum_{\mathbf{k}, i\nu_m} \mathcal{G}_{\delta\alpha}(\mathbf{k}, i\nu_m) \mathcal{G}_{\beta\gamma}(\mathbf{k}+\mathbf{q}, i\omega_n + i\nu_m). \tag{B.3}$$

In the RPA formalism, the response function fulfills the Dyson equation

$$\chi_{\alpha\beta\gamma\delta}(\mathbf{q}, i\omega_n) = \sum_{\alpha'\beta'\gamma'\delta'} \chi_{\alpha\beta\alpha'\beta'}(\mathbf{q}, i\omega_n) V_{\alpha'\beta'\gamma'\delta'}(\mathbf{q}) \chi^{(0)}_{\gamma'\delta'\gamma\delta}(\mathbf{q}, i\omega_n) + \chi^{(0)}_{\alpha\beta\gamma\delta}(\mathbf{q}, i\omega_n) \tag{B.4}$$

which has the following solution in matrix form

$$\chi_q = (\mathbb{1} - \chi^{(0)}_q \mathbf{V}_\mathbf{q})^{-1} \chi^{(0)}_q \tag{B.5}$$

where we have introduced a combined energy-momentum label $q = (\mathbf{q}, i\omega_n)$. The bare response function $\chi^{(0)}_q$ is computed on a mean-field level:

$$\chi^{(0)}_{\alpha\beta\gamma\delta}(\mathbf{q}, \omega) = \frac{1}{2N} \sum_{\mathbf{k}} \sum_{\mu\nu} \frac{n^\mu_{\mathbf{k}+\mathbf{q}} - n^\nu_{\mathbf{k}}}{\omega + \varepsilon^\mu_{\mathbf{k}+\mathbf{q}} - \varepsilon^\nu_{\mathbf{k}} + i\eta} (\alpha^\mu_{\alpha,\mathbf{k}+\mathbf{q}})^* \alpha^\nu_{\beta\mathbf{k}} \alpha^\mu_{\delta,\mathbf{k}+\mathbf{q}} (\alpha^\nu_{\gamma\mathbf{k}})^* \tag{B.6}$$

with $\alpha^\mu_{\beta\mathbf{k}}$ being the projection of the eigenstate with eigenvalue $\varepsilon^\mu_{\mathbf{k}}$. Finally, the dynamical spin-structure factor is given by

$$\mathcal{S}^{ij}(\mathbf{k}, \omega) = -\frac{1}{\pi} \operatorname{Im} \sum_{ab} \sum_{\alpha\beta\gamma\delta} e^{-i\mathbf{k}\cdot(\mathbf{r}_a - \mathbf{r}_b)} \chi^{\alpha\beta\gamma\delta}_{aabb}(\mathbf{k}, \omega) \sigma^i_{\alpha\beta} \sigma^j_{\gamma\delta}. \tag{B.7}$$

where we have explicitly introduced sublattice indices a, b. For the spin response in the ordered 120° phase and the antiferromagnetic generalized Wigner crystal, we use an on-site interaction for the RPA calculation. For the chiral spin liquid phase, we work with an antiferromagnetic Heisenberg-Hamiltonian, which can be expressed in terms of Abrikosov fermions as Eq. (3.2). After performing a mean-field decoupling, one gets the free spinon Hamiltonian of Eq. (3.3). We assume a Kalmeyer-Laughlin type of chiral spin liquid [84], which fixes the hoppings J_{ij}^{eff} up to a gauge transformation. Using the free spinon Hamiltonian of Eq. (3.3), we compute the bare response and then apply the above-described RPA formalism, expressing the interaction Hamiltonian Eq. (3.2) in momentum space as

$$H_{\text{int}} = \frac{1}{N} \sum_{\substack{\mathbf{k},\mathbf{k}',\mathbf{q} \\ \alpha\beta}} V(\mathbf{q}) f^{\dagger}_{\alpha\mathbf{k}+\mathbf{q}} f^{\dagger}_{\beta\mathbf{k}'-\mathbf{q}} f_{\alpha\mathbf{k}'} f_{\beta\mathbf{k}} \tag{B.8}$$

with

$$V(\mathbf{q}) = \frac{J}{4} \sum_{n=0}^{5} e^{-i\mathbf{q}\cdot\boldsymbol{\delta}_n} \tag{B.9}$$

where $\boldsymbol{\delta}_n = \mathrm{R}\left(\frac{n\pi}{3}\right) \boldsymbol{\delta}_0$, $\boldsymbol{\delta}_0 = (1, 0)^T$ are the six nearest neighbors in the triangular lattice and $\mathrm{R}(\theta)$ is a rotation matrix.

Appendix C

Linear Spin-wave theory

C.1 Holstein-Primakoff

Consider the $J_1 - J_2$ model on a hexagonal lattice

$$H = J_1 \sum_{\langle ij \rangle} \mathbf{S}_i \cdot \mathbf{S}_j + J_2 \sum_{\langle\langle ij \rangle\rangle} \mathbf{S}_i \cdot \mathbf{S}_j \tag{C.1}$$

with nearest-neighbor spin coupling J_1 and next-nearest-neighbor spin coupling J_2. We assume that $|J_1| \gg |J_2|$ is the dominant energy scale. Explicitly in terms of sublattices

$$H = J_1 \sum_{\mathbf{i}} \sum_{\delta=1}^{3} \mathbf{S}_{A,\mathbf{i}} \cdot \mathbf{S}_{B,\mathbf{i}+\delta} + J_2 \sum_{\mathbf{i}} \sum_{\delta'=1}^{3} (\mathbf{S}_{A,\mathbf{i}} \cdot \mathbf{S}_{A,\mathbf{i}+\delta'} + \mathbf{S}_{B,\mathbf{i}} \cdot \mathbf{S}_{B,\mathbf{i}+\delta'}) \tag{C.2}$$

where $\mathbf{S}_{a,\mathbf{i}}$ is the spin operator on sublattice $a \in \{A, B\}$ and site $\mathbf{i} \equiv \mathbf{x}_i$. The nearest-neighbor vectors δ and δ' are chosen as follows

$$\delta_1 = 0, \quad \delta_2 = -\mathbf{b}_1, \quad \delta_3 = -\mathbf{b}_1 - \mathbf{b}_2 \tag{C.3}$$

$$\delta'_1 = \mathbf{b}_1, \quad \delta'_2 = \mathbf{b}_2, \quad \delta'_3 = \mathbf{b}_1 + \mathbf{b}_2 \tag{C.4}$$

with $\mathbf{b}_{1/2}$ defined in Fig. 2.1b).

We consider the ferromagnetic case $J_1 < 0$. Here the Holstein-Primakoff transformation for sublattice A and B is equivalent:

$$S^x_{a,\mathbf{i}} = S - a^\dagger_{\mathbf{i}} a_{\mathbf{i}} \tag{C.5}$$

$$S^+_{a,\mathbf{i}} = \sqrt{2S} \sqrt{1 - \frac{a^\dagger_{\mathbf{i}} a_{\mathbf{i}}}{2S}}\, a_{\mathbf{i}} \tag{C.6}$$

$$S^-_{a,\mathbf{i}} = \sqrt{2S} a^\dagger_{\mathbf{i}} \sqrt{1 - \frac{a^\dagger_{\mathbf{i}} a_{\mathbf{i}}}{2S}} \tag{C.7}$$

with $S^\pm = S^y \pm i S^z$. The bosonic creation and annihilation operators describe spin excitations around the ordered ground state, defined by $a_{\mathbf{i}} |0\rangle = 0$. We expand in the total spin $S \gg 1$, even though we are eventually interested in the $S = 1/2$ case. The resulting quadratic spin-wave Hamiltonian is given in momentum space by

$$H = -3 J_1 S \sum_{\mathbf{k}} (a^\dagger_{\mathbf{k}}, b^\dagger_{\mathbf{k}}) H(\mathbf{k}) \begin{pmatrix} a_{\mathbf{k}} \\ b_{\mathbf{k}} \end{pmatrix} \tag{C.8}$$

$$H(\mathbf{k}) = \begin{pmatrix} 1 - \frac{2J_2}{J_1}(1 - \xi_{\mathbf{k}}) & -\gamma_{\mathbf{k}} \\ -\gamma^*_{\mathbf{k}} & 1 - \frac{2J_2}{J_1}(1 - \xi_{\mathbf{k}}) \end{pmatrix} \tag{C.9}$$

with $\xi_{\mathbf{k}} = 1/3 \sum_{\delta'} \cos(\mathbf{k} \cdot \delta')$ and $\gamma_{\mathbf{k}} = 1/3 \sum_{\delta} e^{-i\mathbf{k}\cdot\delta}$. Diagonalizing $H(\mathbf{k})$ yields the spin-wave dispersion

$$\varepsilon^{\pm}_{\mathbf{k}} = 3J_1 S\big[1 - \frac{2J_2}{J_1}(1 - \xi_{\mathbf{k}}) \pm |\gamma_{\mathbf{k}}|\big]. \tag{C.10}$$

The lower branch is gapless at $\mathbf{k} = 0$ and the K and K' points of the Brillouin zone, whereas the upper branch is gapped in the long-wavelength limit. The gap between the two branches closes at finite energy at the corners κ of the reduced Brillouin zone, forming bosonic Dirac cones [81]. For $J_2 = 0$, the two bands have the same bandwidth. For antiferromagnetic $J_2 < 0$, the bandwidth of the lower branch increases, while the bandwidth of the upper branch decreases. For ferromagnetic $J_2 > 0$, the opposite is the case. Consequently, the main effect of a finite next-nearest-neighbor spin coupling is to break the symmetry between the two branches by renormalizing the energies differently. In the basis that diagonalizes the Hamiltonian of Eq. (C.9), the magnon operators can be written as

$$a_{\mathbf{k}} = \sum_{\lambda \in \{\pm\}} u^{a}_{\lambda\mathbf{k}} f_{\lambda\mathbf{k}}. \tag{C.11}$$

In terms of the coefficients $u^{a}_{\lambda\mathbf{k}}$, the spin-spin response

$$\chi^{\mu\nu}_{ab}(\mathbf{k}, \omega) = -\frac{i}{N} \int_0^{\infty} \mathrm{d}t \, e^{i\omega t} \left\langle [S^{\mu}_{a,\mathbf{k}}(t), S^{\nu}_{b,-\mathbf{k}}(0)] \right\rangle \tag{C.12}$$

is given by

$$\chi^{xx}_{ab}(\mathbf{k}, \omega) = 0 \tag{C.13}$$

$$\chi^{yy}_{ab}(\mathbf{k}, \omega) = \chi^{zz}_{ab}(\mathbf{k}, \omega) = \frac{S}{2} \sum_{\lambda \in \{\pm\}} \left[\frac{u^{a}_{\lambda,-\mathbf{k}}(u^{b}_{\lambda,-\mathbf{k}})^*}{\omega - \varepsilon^{\lambda}_{\mathbf{k}} + i\eta} - \frac{(u^{a}_{\lambda,\mathbf{k}})^* u^{b}_{\lambda,\mathbf{k}}}{\omega + \varepsilon^{\lambda}_{\mathbf{k}} + i\eta} \right] \tag{C.14}$$

$$\chi^{yz}_{ab}(\mathbf{k}, \omega) = -\chi^{yz}_{ab}(\mathbf{k}, \omega) = -i\frac{S}{2} \sum_{\lambda \in \{\pm\}} \left[\frac{u^{a}_{\lambda,-\mathbf{k}}(u^{b}_{\lambda,-\mathbf{k}})^*}{\omega - \varepsilon^{\lambda}_{\mathbf{k}} + i\eta} + \frac{(u^{a}_{\lambda,\mathbf{k}})^* u^{b}_{\lambda,\mathbf{k}}}{\omega + \varepsilon^{\lambda}_{\mathbf{k}} + i\eta} \right]. \tag{C.15}$$

The total spin-structure factor is

$$\mathcal{S}(\mathbf{k}, \omega) = -\frac{1}{\pi} \operatorname{Im} \sum_{\mu} \sum_{ab} e^{-i\mathbf{k}\cdot(\mathbf{r}_a - \mathbf{r}_b)} \chi^{\mu\mu}_{ab}(\mathbf{k}, \omega). \tag{C.16}$$

C.2 Bosonization in topological flat band

We outline a bosonization approach to describe spin excitations in topological flat bands, developed in Refs. [101–103]. Our derivation closely follows Ref. [102]. Consider a generic single-particle Hamiltonian hosting flat Chern bands

$$H_{\mathbf{k}} = \begin{pmatrix} h^{\uparrow}_{\mathbf{k}} & 0 \\ 0 & h^{\downarrow}_{\mathbf{k}} \end{pmatrix} \tag{C.17}$$

with $h^{\uparrow}_{\mathbf{k}} = B_{0,\mathbf{k}}\tau^0 + \mathbf{B}_{\mathbf{k}} \cdot \boldsymbol{\tau}$. Here, τ^{μ} are Pauli matrices acting on a sublattice degree of freedom, and $h^{\downarrow}_{\mathbf{k}}$ is the time-reversed copy of $h^{\uparrow}_{\mathbf{k}}$. Expressing Eq. (C.17) in its eigenbasis yields $\tilde{H}_{\mathbf{k}} = \mathrm{diag}(\tilde{h}_{\mathbf{k}}, \tilde{h}^*_{-\mathbf{k}})$ with $\tilde{h}_{\mathbf{k}} = \mathrm{diag}(\omega^{+}_{\mathbf{k}}, \omega^{-}_{\mathbf{k}})$, where the basis transformation is given by

$$\begin{pmatrix} c^\dagger_{A\sigma\mathbf{k}} \\ c^\dagger_{B\sigma\mathbf{k}} \end{pmatrix} = \begin{pmatrix} u_\mathbf{k} & v^*_\mathbf{k} \\ v_\mathbf{k} & -u^*_\mathbf{k} \end{pmatrix} \begin{pmatrix} \gamma^\dagger_{+\sigma\mathbf{k}} \\ \gamma^\dagger_{-\sigma\mathbf{k}} \end{pmatrix}. \tag{C.18}$$

Next, we assume that the γ_+ bands are separated by a large gap Δ_+ from the γ_- bands and that interactions lead to spontaneous spin polarization. The corresponding ferromagnetic ground state is

$$|FM\rangle = \prod_\mathbf{k} \gamma^\dagger_{-\uparrow\mathbf{k}} |0\rangle . \tag{C.19}$$

There are three relevant energy scales: the gap Δ_+, the interaction strength U, which induces a Zeeman splitting of the γ_- bands, and the bandwidth W_- of the γ_- bands. We work in the limit $\Delta_+ \gg U \gg W_-$, such that we can safely project onto the two γ_- bands. In the following, all band indices ± are dropped. The projected spin operators are given by

$$\bar{S}^+_{a\mathbf{k}} = \sum_\mathbf{p} G_a(\mathbf{p},\mathbf{k}) \gamma^\dagger_{\uparrow\mathbf{p}-\mathbf{k}} \gamma_{\downarrow\mathbf{p}} \tag{C.20}$$

$$\bar{S}^-_{a\mathbf{k}} = \sum_\mathbf{p} G_a(\mathbf{p},\mathbf{k}) \gamma^\dagger_{\downarrow\mathbf{p}-\mathbf{k}} \gamma_{\uparrow\mathbf{p}} \tag{C.21}$$

with $G_A(\mathbf{p},\mathbf{k}) = v^*_{\mathbf{p}-\mathbf{k}} v_\mathbf{p}$ and $G_B(\mathbf{p},\mathbf{k}) = u^*_{\mathbf{p}-\mathbf{k}} u_\mathbf{p}$. It is useful to introduce the following linear combination of projected spin operators:

$$\bar{S}^\lambda_{\alpha\mathbf{k}} = \bar{S}^\lambda_{A\mathbf{k}} + (-1)^\alpha \bar{S}^\lambda_{B\mathbf{k}} \tag{C.22}$$

with $\alpha \in \{0,1\}$. They obey the commutator relation

$$[\bar{S}^+_{\alpha\mathbf{q}}, \bar{S}^-_{\beta\mathbf{k}}] = \sum_\mathbf{p} \Big(g_\alpha(\mathbf{p}-\mathbf{k},\mathbf{q}) g_\beta(\mathbf{p},\mathbf{k}) \gamma^\dagger_{\uparrow\mathbf{p}-\mathbf{k}-\mathbf{q}} \gamma_{\uparrow\mathbf{p}} - g_\alpha(\mathbf{p},\mathbf{q}) g_\beta(\mathbf{p}-\mathbf{q},\mathbf{k}) \gamma^\dagger_{\downarrow\mathbf{p}-\mathbf{k}-\mathbf{q}} \gamma_{\downarrow\mathbf{p}} \Big) \tag{C.23}$$

with $g_\alpha(\mathbf{p},\mathbf{k}) = G_A(\mathbf{p},\mathbf{k}) + (-1)^\alpha G_B(\mathbf{p},\mathbf{k})$. Generically, this is not a closed algebra. Assuming that the ferromagnetic ground state is stable against spin excitation, we can approximate the operators on the right-hand-side of Eq. (C.23) with their ground state expectation value

$$\gamma^\dagger_{\uparrow\mathbf{p}-\mathbf{q}} \gamma_{\uparrow\mathbf{p}} \approx \langle FM | \gamma^\dagger_{\uparrow\mathbf{p}-\mathbf{q}} \gamma_{\uparrow\mathbf{p}} | FM \rangle = \delta_{\mathbf{q},0} \tag{C.24}$$

$$\gamma^\dagger_{\downarrow\mathbf{p}-\mathbf{q}} \gamma_{\downarrow\mathbf{p}} \approx \langle FM | \gamma^\dagger_{\downarrow\mathbf{p}-\mathbf{q}} \gamma_{\downarrow\mathbf{p}} | FM \rangle = 0. \tag{C.25}$$

Under this approximation, the commutator Eq. (C.23) reduces to

$$[\bar{S}^+_{\alpha\mathbf{q}}, \bar{S}^-_{\beta\mathbf{k}}] = \delta_{\mathbf{q},-\mathbf{k}} \sum_\mathbf{p} g_\alpha(\mathbf{p}+\mathbf{q},-\mathbf{q}) g_\beta(\mathbf{p},-\mathbf{q}) \tag{C.26}$$

which, up to a constant rescaling, corresponds to the Bose algebra. It can be shown that the sum on the right-hand-side of Eq. (C.26) is proportional to $\delta_{\alpha\beta}$ [102]. We introduce the boson operators

$$b^\dagger_{\alpha\mathbf{q}} = \frac{1}{F_{\alpha\mathbf{q}}} \bar{S}^-_{\alpha,\mathbf{q}} \tag{C.27}$$

$$b_{\alpha\mathbf{q}} = \frac{1}{F_{\alpha\mathbf{q}}} \bar{S}^+_{\alpha,-\mathbf{q}} \tag{C.28}$$

which create and destroy spin excitations on top of the ferromagnetic ground state. We have defined the normalization factor $F^2_{\alpha\mathbf{q}}\delta_{\alpha\beta} := \sum_{\mathbf{p}} g_\alpha(\mathbf{p}+\mathbf{q},-\mathbf{q})g_\beta(\mathbf{p},-\mathbf{q})$. Our goal is to project the Hamiltonian

$$H = H_0 + H_U = H_0 + \frac{U}{N}\sum_{a\mathbf{k}} \rho_{a\uparrow,-\mathbf{k}}\rho_{a\downarrow,\mathbf{k}} \tag{C.29}$$

onto the lower two Chern bands and express all operators as a function of the boson operators b and $b^\dagger$. Using the relation

$$\gamma^\dagger_{\downarrow\mathbf{p}-\mathbf{k}}\gamma_{\uparrow\mathbf{p}} \equiv \sum_\beta \frac{g_\beta(\mathbf{p}-\mathbf{k},-\mathbf{k})}{F_{\beta\mathbf{k}}} b^\dagger_{\beta\mathbf{k}} \tag{C.30}$$

one can express the projected density operators as

$$\bar{\rho}_{a\sigma\mathbf{k}} = \frac{N}{2}\delta_{\sigma\uparrow}\delta_{\mathbf{k},0} + \sum_{\alpha\beta}\sum_{\mathbf{q}} \mathcal{G}_{\alpha\beta a\sigma}(\mathbf{k},\mathbf{q}) b^\dagger_{\beta\mathbf{k}+\mathbf{q}} b_{\alpha\mathbf{q}} \tag{C.31}$$

with

$$\begin{aligned}\mathcal{G}_{\alpha\beta a\downarrow} &= \frac{1}{F_{\alpha\mathbf{q}}F_{\beta\mathbf{k}+\mathbf{q}}}\sum_{\mathbf{p}} G_a(\mathbf{p}-\mathbf{q},\mathbf{k})g_\alpha(\mathbf{p},\mathbf{q})g_\beta(\mathbf{p}-\mathbf{k}-\mathbf{q},-\mathbf{k}-\mathbf{q}) \\ &= -\mathcal{G}^*_{\alpha\beta a\uparrow}(-\mathbf{k},-\mathbf{q}).\end{aligned} \tag{C.32}$$

In the flat-band limit $U \gg W_-$, the kinetic term H_0 only gives a constant contribution to the energy. The spin-wave dispersion can be obtained by expressing the projected interaction Hamiltonian $\bar{H}_U$ in terms of the boson operators

$$\bar{H}_U = \sum_{\alpha\beta}\sum_{\mathbf{p}} \varepsilon^{\alpha\beta}_{\mathbf{p}} b^\dagger_{\beta\mathbf{p}} b_{\alpha\mathbf{p}} + \frac{1}{N}\sum_{\alpha\beta\alpha'\beta'}\sum_{\mathbf{k}\mathbf{q}\mathbf{q}'} V^{\alpha\beta\alpha'\beta'}_{\mathbf{k}\mathbf{q}\mathbf{q}'} b^\dagger_{\beta'\mathbf{q}'+\mathbf{k}} b^\dagger_{\beta\mathbf{q}-\mathbf{k}} b_{\alpha\mathbf{q}} b_{\alpha'\mathbf{q}'} \tag{C.33}$$

with

$$\varepsilon^{\alpha\beta}_{\mathbf{p}} = \frac{U}{2}\sum \mathcal{G}_{\alpha\beta a\downarrow}(0,\mathbf{p}) + \frac{U}{N}\sum_{a,\alpha,\mathbf{q}} \mathcal{G}_{\alpha'\beta a\uparrow}(\mathbf{p}-\mathbf{q},\mathbf{q})\mathcal{G}_{\alpha'\alpha a\downarrow}(\mathbf{q}-\mathbf{p},\mathbf{p}) \tag{C.34}$$

$$V^{\alpha\beta\alpha'\beta'}_{\mathbf{k}\mathbf{q}\mathbf{q}'} = U\sum_a \mathcal{G}_{\alpha\beta a\uparrow}(-\mathbf{k},\mathbf{q})\mathcal{G}_{\alpha'\beta' a\downarrow}(\mathbf{k},\mathbf{q}'). \tag{C.35}$$

The linear spin-waves dispersion follows from diagonalizing the quadratic part of Eq. (C.33).

Appendix D

Tunneling in a magnetic field

In this appendix, we provide explicit expressions for Eq. (4.12) and Eq. (4.15). For that purpose, it is useful to consider the following integral

$$I_{\mathbf{q}}(n,m) := \int_{-\infty}^{\infty} \mathrm{d}x \; e^{iq_x x} (\phi_n^{(\mathfrak{t})}(x))^* \phi_m^{(\mathfrak{b})}(x) \tag{D.1}$$

with $\phi_n^{(\ell)}(x)$ defined in Eq. (4.5). To make progress, we first introduce another integral:

$$F_{nm}(b,c) := \int_{-\infty}^{\infty} \mathrm{d}z \; e^{z^2+bz-c^2/2} H_n(z) H_m(z-c). \tag{D.2}$$

In terms of F_{nm}, the integral Eq. (D.1) can be expressed as

$$I_{\mathbf{q}}(n,m) = \frac{e^{iq_x X_{\mathfrak{t}}}}{\sqrt{2^{n+m}\pi n! m!}} F_{nm}\big(b = \ell_B[\Delta K_y - q_y + i(\Delta K_x + q_x)],\; c = \ell_B[\Delta K_y - q_y]\big) \tag{D.3}$$

with $X_\ell = \ell_B^2(k_y + \ell \Delta K_y)$ and $\Delta \mathbf{K} = (\mathrm{R}(\theta) - \mathbb{1})\mathbf{K}$. Here $\mathrm{R}(\theta)$ is a rotation matrix. Using standard properties of Hermite polynomials, F_{nm} can be computed to be

$$F_{nm}(b,c) = \sqrt{\pi} e^{b^2/4 - c^2/2} \sum_{j=0}^{m} \sum_{i=0}^{\min(n,j)} (-c)^{m-j} b^{n+j-2i} \frac{2^{m+i-j} n! m!}{(m-j)!(n-i)!(j-i)! i!} \tag{D.4}$$

$$= \sqrt{\pi} e^{b^2/4 - c^2/2} \sum_{j=0}^{m} \begin{pmatrix} m \\ j \end{pmatrix} (-2c)^{m-j} b^{j-n} U(-n, 1-n+j, -b^2/2) \tag{D.5}$$

where $U(a,b,z)$ is the Tricomi confluent hypergeometric function [122]. For Eq. (4.15), we find

$$\begin{aligned} \Psi_{\mathbf{q}}^{n_{\mathfrak{t}}k_{\mathfrak{t}},n_{\mathfrak{b}}k_{\mathfrak{b}}} = C_{n_{\mathfrak{t}}} C_{n_{\mathfrak{b}}} \delta(k_{\mathfrak{t}} - k_{\mathfrak{b}} - q_y) \big[& I_{\mathbf{q}}(|n_{\mathfrak{t}}|, |n_{\mathfrak{b}}|) \\ & + \mathrm{sgn}(n_{\mathfrak{t}}) \mathrm{sgn}(n_{\mathfrak{b}}) I_{\mathbf{q}}(|n_{\mathfrak{t}}| - 1, |n_{\mathfrak{b}}| - 1) \\ & - i\, \mathrm{sgn}(n_{\mathfrak{b}}) I_{\mathbf{q}}(|n_{\mathfrak{t}}|, |n_{\mathfrak{b}}| - 1) + i\, \mathrm{sgn}(n_{\mathfrak{t}}) I_{\mathbf{q}}(|n_{\mathfrak{t}}| - 1, |n_{\mathfrak{b}}|) \big] \end{aligned} \tag{D.6}$$

with $C_n = \sqrt{(1+\delta_{n,0})/2}$. For the tunneling amplitudes Eq. (4.12) one obtains

$$W(n_{\mathfrak{t}}, n_{\mathfrak{b}}) = \frac{L^4}{(2\pi)^2} \int \mathrm{d}k_{\mathfrak{t}} \mathrm{d}k_{\mathfrak{b}} \; |\Psi_{\mathbf{q}=0}^{n_{\mathfrak{t}}k_{\mathfrak{t}},n_{\mathfrak{b}}k_{\mathfrak{b}}}|^2. \tag{D.7}$$

Appendix E

Parton construction

We work in the lowest Chern band of the spin-polarized single-particle Hamiltonian $H^{\uparrow}_{\text{KM}}$ given by Eq. (1.13). In its eigenbasis, it can be written as

$$H^{\uparrow}_{\text{KM}} = \sum_{\mathbf{k}} \sum_{\lambda \in \{\pm\}} \varepsilon^{\lambda}_{\mathbf{k}} \gamma^{\dagger}_{\lambda\mathbf{k}} \gamma_{\lambda\mathbf{k}} \tag{E.1}$$

with the electron operator on sublattice $a \in \{A, B\}$ given by $c_{a\mathbf{k}} = u_{a+,\mathbf{k}}\gamma_{+,\mathbf{k}} + u_{a-,\mathbf{k}}\gamma_{-,\mathbf{k}}$. The projected electron operator is given by $\bar{c}_{a\mathbf{k}} = u_{a-,\mathbf{k}}\gamma_{-,\mathbf{k}} \equiv u_{a,\mathbf{k}}\gamma_{\mathbf{k}}$. We describe fractional anomalous Hall states at fillings $\nu = p/m$ with a parton construction [106, 107], where the γ operator fractionalizes into m fermionic partons

$$\gamma(\mathbf{r}) = \prod_{\alpha=1}^{m} f_{\alpha}(\mathbf{r}) \tag{E.2}$$

where m is an odd integer and $m > p \in \mathbb{N}$. Each parton carries an electric charge $e^* = e/m$. This construction introduces a gauge degree of freedom, since Eq. (E.2) is invariant under local SU(m) transformations $f_{\alpha}(\mathbf{r}) \to G_{\alpha\beta}(\mathbf{r}) f_{\beta}(\mathbf{r})$ with $G(\mathbf{r}) \in$ SU(m). We describe the partons using a mean-field ansatz

$$H_m = \sum_{i,j} \sum_{\alpha=1}^{m} t_{ij} f^{\dagger}_{\alpha}(\mathbf{r}_i) f_{\alpha}(\mathbf{r}_j) \tag{E.3}$$

where we have assumed that different flavors of partons do not mix. Our goal is to choose a mean-field ansatz whose lowest p bands are gapped and have a Chern number of $+1$ each. If we then fill up these lowest p bands, we end up with the

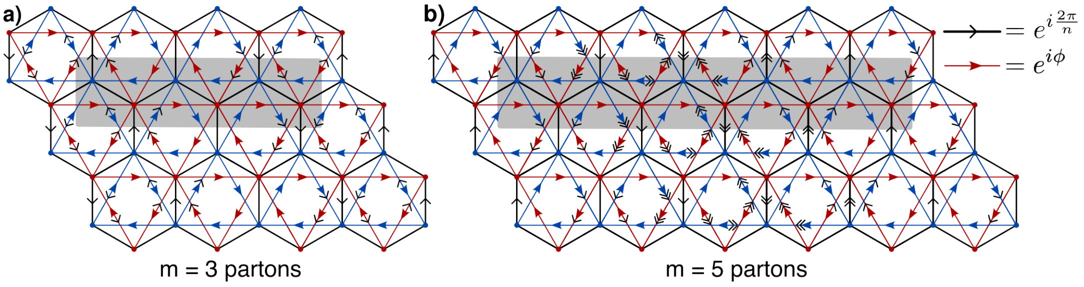

FIGURE E.1: **Gauge choice for parton flux pattern. a)** $m = 3$ partons **b)** $m = 5$ partons. The enlarged unit cell is highlighted in gray. Hopping along a blue or red arrow adds a phase $e^{i\phi}$, while a single black arrows yield a phase $e^{i2\pi/m}$, and two black arrows yield $e^{i\pi/m}$. Translation symmetry is broken on the parton level by adding a flux of $2\pi/m$ per primitive unit cell.

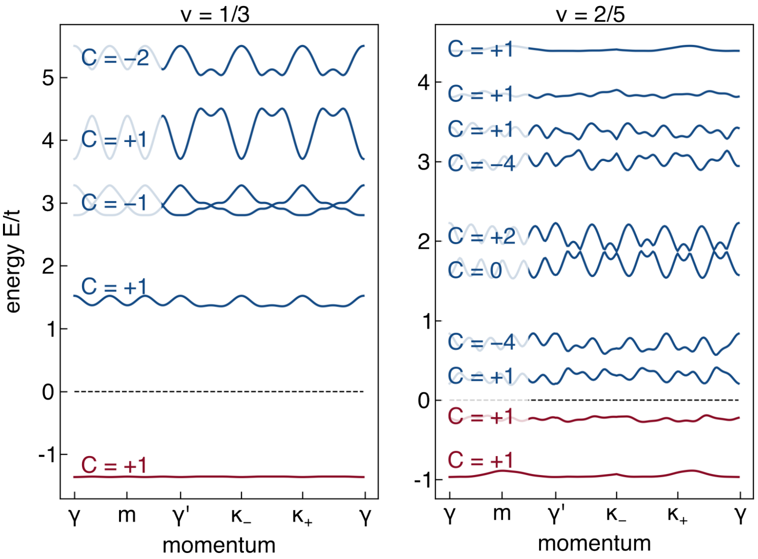

FIGURE E.2: **Parton band structure.** Bandstructure of the parton mean-field ansatz for $\nu = 1/3$ on the left and $\nu = 2/5$ on the right. We use a six-site unit cell for the parton construction with $m = 3$ partons, resulting in six parton bands. For $m = 5$, a ten-site unit cell is used. The Chern number for each gapped band is shown.

desired Hall conductivity of

$$\sigma_{xy} = mp\frac{(e^*)^2}{2\pi\hbar} = \frac{p}{m}\frac{e^2}{2\pi\hbar}. \tag{E.4}$$

Due to the additional gauge degree of freedom, the parton mean-field ansatz can break the lattice symmetries U, as long as it is invariant under a combination of U and some local gauge transformation $G_{\mathrm{U}}(\mathbf{r})$. Explicitly, we can insert $2\pi/m$ flux per primitive unit cell to construct a parton mean-field state with the desired properties. Note that the corresponding electron state still preserves all lattice symmetries U. In Fig. E.1, we show the flux pattern we have chosen for the $m = 3$ and $m = 5$ states. The $m = 3$ state was adpoted from [106]. In the sublattice basis $\Psi_{\mathbf{k}} = (f_{A_1\mathbf{k}}, f_{B_1\mathbf{k}}, f_{A_2\mathbf{k}}, f_{B_2\mathbf{k}}, f_{A_3\mathbf{k}}, f_{B_3\mathbf{k}})$ the $m = 3$ parton Hamiltonian is given by

$$h^{(1)}_{\mathbf{k}} = \begin{bmatrix} 0 & e^{i\varphi}e^{i\mathbf{k}\cdot\delta_4} + e^{i\mathbf{k}\cdot\delta_2} & 0 & e^{i\mathbf{k}\cdot\delta_0} & 0 & 0 \\ 0 & 0 & 0 & 0 & 0 & 0 \\ 0 & 0 & 0 & e^{i\mathbf{k}\cdot\delta_4} + e^{i\mathbf{k}\cdot\delta_2} & 0 & e^{i\mathbf{k}\cdot\delta_0} \\ 0 & 0 & 0 & 0 & 0 & 0 \\ 0 & e^{i\mathbf{k}\cdot\delta_0} & 0 & 0 & 0 & e^{-i\varphi}e^{i\mathbf{k}\cdot\delta_4} + e^{i\mathbf{k}\cdot\delta_2} \\ 0 & 0 & 0 & 0 & 0 & 0 \end{bmatrix} \tag{E.5}$$

$$h^{(2)}_{\mathbf{k}} = \begin{bmatrix} e^{i\varphi}e^{i\mathbf{k}\cdot\mathbf{a}_3} & 0 & e^{i\mathbf{k}\cdot\mathbf{a}_1} & 0 & e^{i\mathbf{k}\cdot\mathbf{a}_2} & 0 \\ 0 & e^{-i\varphi}e^{-i\mathbf{k}\cdot\mathbf{a}_3} & 0 & e^{-i\mathbf{k}\cdot\mathbf{a}_2} & 0 & e^{-i\varphi}e^{-i\mathbf{k}\cdot\mathbf{a}_1} \\ e^{i\mathbf{k}\cdot\mathbf{a}_2} & 0 & e^{i\mathbf{k}\cdot\mathbf{a}_3} & 0 & e^{i\varphi}e^{i\mathbf{k}\cdot\mathbf{a}_1} & 0 \\ 0 & e^{i\varphi}e^{-i\mathbf{k}\cdot\mathbf{a}_1} & 0 & e^{-i\mathbf{k}\cdot\mathbf{a}_3} & 0 & e^{-i\mathbf{k}\cdot\mathbf{a}_2} \\ e^{-i\varphi}e^{i\mathbf{k}\cdot\mathbf{a}_1} & 0 & e^{i\mathbf{k}\cdot\mathbf{a}_2} & 0 & e^{-i\varphi}e^{i\mathbf{k}\cdot\mathbf{a}_3} & 0 \\ 0 & e^{-i\mathbf{k}\cdot\mathbf{a}_2} & 0 & e^{-i\mathbf{k}\cdot\mathbf{a}_1} & 0 & e^{i\varphi}e^{-i\mathbf{k}\cdot\mathbf{a}_3} \end{bmatrix} \tag{E.6}$$

$$H_{m=3} = -\sum_{\mathbf{k}} \Psi^\dagger_{\mathbf{k}} \left(t h^{(1)}_{\mathbf{k}} + t' e^{i\phi} h^{(2)}_{\mathbf{k}} + \text{h.c}\right) \Psi_{\mathbf{k}} \tag{E.7}$$

with $\varphi = \pm 2\pi/3$. The basis lattice vectors are given by $\mathbf{a}_{1/2} = a_M(\pm\sqrt{3}, 1)/2$ and $\mathbf{a}_3 = -(\mathbf{a}_1 + \mathbf{a}_2)$, while the nearest neighbor vectors are $\delta_n = \mathrm{R}_{\pi n/3}\delta_0$ with $\delta_0 = (\mathbf{a}_1 - \mathbf{a}_2)/3$. We have suppressed the parton-flavor index since we assume the mean-field ansatz is the same for all three flavors.

Next, we calculate the electronic single-particle spectral function for the case $m = 3$. The spectral function is obtained through the retarded Green's function

$$\begin{aligned}\mathcal{G}(\mathbf{k}, \omega) &= -i\int_0^\infty \mathrm{d}t\, e^{i\omega t}\langle\{c_{\mathbf{k}}(t), c^\dagger_{\mathbf{k}}(0)\}\rangle \\ &= -i\int_0^\infty \mathrm{d}t\, e^{i\omega t}\sum_{ab} e^{-i\mathbf{k}\cdot(\mathbf{r}_a - \mathbf{r}_b)}\langle\{c_{a\mathbf{k}}(t), c^\dagger_{b\mathbf{k}}(0)\}\rangle \end{aligned} \tag{E.8}$$

where $\mathbf{r}_a$ is the position of site a within the unit cell. If we restrict ourselves to the lowest Chern band, Eq.(E.8) can be written as

$$\mathcal{G}(\mathbf{k}, \omega) = Z_{\mathbf{k}}\bar{\mathcal{G}}(\mathbf{k}, \omega) \tag{E.9}$$

with

$$Z_{\mathbf{k}} = \sum_{ab} e^{-i\mathbf{k}\cdot(\mathbf{r}_a - \mathbf{r}_b)} u_{a,\mathbf{k}} u^*_{b,\mathbf{k}} \tag{E.10}$$

and

$$\bar{\mathcal{G}}(\mathbf{k}, \omega) = -i\int_0^\infty \mathrm{d}t\, e^{i\omega t}\langle\{\gamma_{\mathbf{k}}(t), \gamma^\dagger_{\mathbf{k}}(0)\}\rangle. \tag{E.11}$$

Since, on a mean-field level, the three parton flavors are independent of each other, the single-particle Green's function in real space is the product of the three parton Green's functions:

$$\begin{aligned}\bar{\mathcal{G}}(\mathbf{r}, \tau) &= -\langle\mathcal{T}\gamma(\mathbf{r}, \tau)\gamma^\dagger(0, 0)\rangle \\ &= -\langle\mathcal{T} f_1(\mathbf{r}, \tau) f_2(\mathbf{r}, \tau) f_3(\mathbf{r}, \tau) f_3^\dagger(0, 0) f_2^\dagger(0, 0) f_1^\dagger(0, 0)\rangle \\ &= -\langle\mathcal{T} f_1(\mathbf{r}, \tau) f_1^\dagger(0, 0)\rangle\langle\mathcal{T} f_2(\mathbf{r}, \tau) f_2^\dagger(0, 0)\rangle\langle\mathcal{T} f_3(\mathbf{r}, \tau) f_3^\dagger(0, 0)\rangle \\ &= \mathcal{G}_1(\mathbf{r}, \tau)\mathcal{G}_2(\mathbf{r}, \tau)\mathcal{G}_3(\mathbf{r}, \tau)\end{aligned} \tag{E.12}$$

In Fourier space, this yields the following convolution

$$\bar{\mathcal{G}}(\mathbf{k}, i\omega_n) = \int \mathrm{d}\mathbf{q}\mathrm{d}\mathbf{p}\sum_{\nu_m\nu_l} G_1(\mathbf{q}, i\nu_m) G_2(\mathbf{p} - \mathbf{q}, i\nu_l - i\nu_m) G_3(\mathbf{k} - \mathbf{p}, i\omega_n - i\nu_l) \tag{E.13}$$

where $i\omega_n$ is a fermionic Matsubara frequency and $i\nu_{m/l}$ are bosonic Matsubara frequencies. The spectral function $\bar{A}(\mathbf{k}, \omega) = -\operatorname{Im}\bar{\mathcal{G}}(\mathbf{k}, \omega + i0^+)/\pi$ can be obtained by inserting the Lehman representation

$$\mathcal{G}_\alpha(\mathbf{k}, i\omega_n) = \int_{-\infty}^{\infty} \mathrm{d}\varepsilon\, \frac{\mathcal{A}_\alpha(\mathbf{k}, \varepsilon)}{i\omega_n - \varepsilon} \tag{E.14}$$

into Eq. (E.13). The Matsubara sums can be explicitly calculated using

$$S_b = \frac{1}{\beta}\sum_{i\nu_l}\frac{1}{i\omega_n - i\nu_l - \varepsilon}\frac{1}{i\nu_l - i\omega_m - \varepsilon'} = \frac{n_F(\varepsilon') - n_F(-\varepsilon)}{i\omega_n - i\omega_m - \varepsilon - \varepsilon'} \tag{E.15}$$

$$S_f = \frac{1}{\beta}\sum_{i\omega_l}\frac{1}{i\omega_l - \varepsilon}\frac{1}{i\omega_n - i\omega_l - \varepsilon'} = \frac{n_F(\varepsilon) + n_B(-\varepsilon')}{i\omega_n - \varepsilon - \varepsilon'} \tag{E.16}$$

where $n_F(\varepsilon)$ is the Fermi-Dirac distribution and $n_B(\varepsilon)$ is the Bose-Einstein distribution. After calculating the Matsubara sums and performing the analytical continuation $i\omega_n \to \omega + i0^+$, one can take the imaginary part of the retarded Green's function to get the spectral function

$$\bar{\mathcal{A}}(\mathbf{k},\omega) = \int \mathrm{d}\mathbf{q}\mathrm{d}\mathbf{p} \int \mathrm{d}\varepsilon \mathrm{d}\varepsilon' \, \mathcal{A}_1(\mathbf{q},\varepsilon)\mathcal{A}_2(\mathbf{p}-\mathbf{q},\varepsilon'-\varepsilon)\mathcal{A}_3(\mathbf{k}-\mathbf{p},\omega-\varepsilon') \\ \times [n_F(\varepsilon)+n_B(\varepsilon-\omega)][n_F(\varepsilon'-\varepsilon)-n_F(\varepsilon'-\omega)]. \quad \text{(E.17)}$$

The projected spectral function is not simply the convolution of the parton spectral functions. There are additional factors of Fermi-Dirac and Bose-Einstein distributions, which ensure that the particle and hole part of the spectral function do not get mixed. Physically, this can be understood from the fact that in a tunneling process, one always adds or removes a whole electron, meaning that one must either add three or remove three partons. Without the additional factors, one would have contributions to the total spectral function where, for example, a single parton is added and two partons are removed. An analogous calculation for the case $m = 5$ yields

$$\begin{aligned}\bar{\mathcal{A}}(\mathbf{k},\Omega) = \int &\mathrm{d}\mathbf{q}\mathrm{d}\mathbf{p}\mathrm{d}\mathbf{q}'\mathrm{d}\mathbf{p}' \int \mathrm{d}\varepsilon\mathrm{d}\varepsilon'\mathrm{d}\omega\mathrm{d}\omega' \Big\{ \mathcal{A}_1(\mathbf{q},\varepsilon)\mathcal{A}_2(\mathbf{p}-\mathbf{q},\omega-\varepsilon) \\ &\times \mathcal{A}_3(\mathbf{q}'-\mathbf{p},\varepsilon'-\omega)\mathcal{A}_4(\mathbf{p}'-\mathbf{q}',\omega'-\varepsilon')\mathcal{A}_5(\mathbf{k}-\mathbf{p}',\Omega-\omega') \\ &\times [n_F(\varepsilon)+n_B(\varepsilon-\Omega)][n_F(\omega-\varepsilon)-n_F(\omega-\Omega)] \\ &\times [n_F(\varepsilon'-\omega)+n_B(\varepsilon'-\Omega)][n_F(\omega'-\varepsilon')-n_F(\omega'-\Omega)]\Big\}. \end{aligned} \quad \text{(E.18)}$$

We postulate that, for general odd $m \geq 3$, one has

$$\begin{aligned}\bar{\mathcal{A}}(\mathbf{k},\Omega) = &\int \prod_{\beta=1}^{m-1} \mathrm{d}\mathbf{q}_\beta \mathrm{d}\varepsilon_\beta \prod_{\alpha=1}^{m} \mathcal{A}(\mathbf{q}_\alpha - \mathbf{q}_{\alpha-1}, \varepsilon_\alpha - \varepsilon_{\alpha-1}) \\ &\times \prod_{j=1}^{(m-1)/2} [n_F(\varepsilon_{2j-1}-\varepsilon_{2j-2})+n_B(\varepsilon_{2j-1}-\varepsilon_m)][n_F(\varepsilon_{2j}-\varepsilon_{2j-1})-n_F(\varepsilon_{2j}-\varepsilon_m)]\end{aligned} \quad \text{(E.19)}$$

with $\mathbf{q}_0 \equiv 0$, $\mathbf{q}_m \equiv \mathbf{k}$, $\varepsilon_0 \equiv 0$ and $\varepsilon_m \equiv \Omega$.

E.1 Exact diagonalization

To verify the validity of the parton ansatz, we performed exact diagonalization calculations. We consider a fully spin-polarized single-particle Hamiltonian of the form

$$H_0 = \sum_{\mathbf{k}} (c^\dagger_{A\mathbf{k}}, c^\dagger_{B\mathbf{k}}) h_{\mathbf{k}} \begin{pmatrix} c_{A\mathbf{k}} \\ c_{B\mathbf{k}} \end{pmatrix} \quad \text{(E.20)}$$

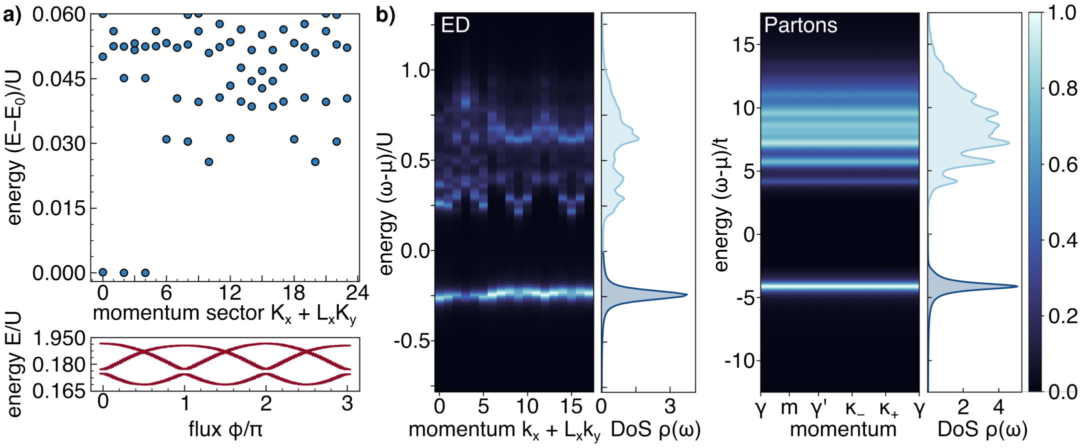

FIGURE E.3: **Exact diagonalization. a)** Top: Energies in different total momentum sectors for the Haldane model with nearest-neighbor interactions at $\nu = 1/3$ filling. The ground state is three-fold degenerate and separated from the first excited states by a clear gap. We work with a system size of $L_x \times L_y = 6 \times 4$. Bottom: Under flux insertion, the three groundstates flow into each other. Model parameters were adopted from Ref. [111]. The gap to the first excited state remains finite for all fluxes. **b)** Comparison of the projected spectral function $\bar{\mathcal{A}}(\mathbf{k}, \omega)$ and the density of states in the $\nu = 1/3$ FQAH state computed with exact diagonalization (left) and the parton ansatz (right). The two approaches agree qualitatively very well, indicating that the parton ansatz captured the essential aspects of the FQAH states.

where $h_{\mathbf{k}} = \mathbf{B}_{\mathbf{k}} \cdot \sigma$ acts on a sublattice degree of freedom and is chosen so that H_0 hosts two bands with nontrivial Chern numbers. Concretely, we work with the Haldane model

$$\begin{aligned} B_x &= t_1\big(1 + \cos(k_1) + \cos(k_1 + k_2)\big) \\ B_y &= -t_1\big(\sin(k_1) + \sin(k_1 + k_2)\big) \\ B_z &= 2t_2 \sin\phi\big(\sin(k_1) + \sin(k_2) - \sin(k_1 + k_2)\big) \end{aligned} \tag{E.21}$$

where the unit cell is spanned by $\mathbf{b}_1 = (\sqrt{3}, 0)$, $\mathbf{b}_2 = -(\sqrt{3}/2, 1/2)$ and the momenta are defined as $(k_1, k_2) = (\mathbf{k} \cdot \mathbf{b}_1, \mathbf{k} \cdot \mathbf{b}_2)$. We also consider the checkerboard lattice model [123, 124], given by

$$\begin{aligned} B_x &= t_1 \,\mathrm{Re}\left[e^{i\phi}(1 + e^{i(k_2 - k_1)}) + e^{-i\phi}(e^{ik_2} + e^{-ik_1})\right] \\ B_y &= -t_1 \,\mathrm{Im}\left[e^{i\phi}(1 + e^{i(k_2 - k_1)}) + e^{-i\phi}(e^{ik_2} + e^{-ik_1})\right] \\ B_z &= 2t_2\big(\cos(k_1) - \cos(k_2)\big) \end{aligned} \tag{E.22}$$

where the unit cell is spanned by $\mathbf{b}_1 = (1, 0)$, $\mathbf{b}_2 = (0, 1)$ and the momenta are defined as $(k_1, k_2) = (\mathbf{k} \cdot \mathbf{b}_1, \mathbf{k} \cdot \mathbf{b}_2)$. Both the checkerboard model and the Haldane model have been shown to host FQAH states at a filling of $\nu = 1/3$ [104, 111]. In both models, t_1 (t_2) is the (next-)nearest-neighbor hopping amplitude and ϕ is some phase. We switch to the eigenbasis of the single-particle Hamiltonian

$$H_0 = \sum_{\mathbf{k}} \sum_{\lambda \in \{\pm\}} \varepsilon^{\lambda}_{\mathbf{k}} \gamma^{\dagger}_{\lambda\mathbf{k}} \gamma_{\lambda\mathbf{k}} \tag{E.23}$$

with $c_{a\mathbf{k}} = u_{a+,\mathbf{k}}\gamma_{+,\mathbf{k}} + u_{a-,\mathbf{k}}\gamma_{-,\mathbf{k}}$. For the lower band, the coefficients are given by $(u_{A-,\mathbf{k}}, u_{B-,\mathbf{k}}) = (-e^{-i\varphi/2}\sin(\theta/2), e^{i\varphi/2}\cos(\theta/2))$, where $\cos(\theta) = B_z/|\mathbf{B}|$ and

$\tan(\varphi) = B_y/B_x$. The fractional quantum Hall effect is intrinsically due to interactions. Consequently, we add nearest-neighbor density-density interactions

$$H_U = U \sum_{\langle i,j \rangle} n_i n_j. \tag{E.24}$$

The FQAH states are most stable in a flat band with uniform Berry curvature, mimicking the lowest Landau level. To minimize the effects of the dispersing single-particle bands, we take the flat-band limit $\varepsilon^{\pm}_{\mathbf{k}} \to \varepsilon^{\pm}_{0} = \text{const.}$ and send $\varepsilon^{+}_{0} \to \infty$, effectively projecting to the lower Chern band. In the following, we drop all band indices $\lambda \in \{\pm\}$ since we projected to the lower band γ_-. The projected interaction Hamiltonian in the basis of the lower Chern band is

$$\bar{H}_U = \frac{U}{L_x L_y} \sum_{\mathbf{q}\mathbf{k}\mathbf{k}'} U(\mathbf{q}, \mathbf{k}, \mathbf{k}') \gamma^{\dagger}_{\mathbf{k}+\mathbf{q}} \gamma^{\dagger}_{\mathbf{k}'-\mathbf{q}} \gamma_{\mathbf{k}'} \gamma_{\mathbf{k}} \tag{E.25}$$

with $U(\mathbf{q}, \mathbf{k}, \mathbf{k}') = V_{\mathbf{q}} u^*_{A\mathbf{k}+\mathbf{q}} u^*_{B\mathbf{k}'-\mathbf{q}} u_{B\mathbf{k}'} u_{A\mathbf{k}}$ and $V_{\mathbf{q}} = 1 + e^{iq_2} + e^{i(q_1+q_2)}$ for the Haldane model and $V_{\mathbf{q}} = (1 + e^{iq_2})(1 + e^{-iq_1})$ for the checkerboard model. Since we work in the flat band limit, the only energy scale of the system is the interaction energy U. To obtain a $\nu = 1/3$ FAQH state, the total system size $N_{\text{tot}} = L_x L_y$ must be a multiple of 3. The largest system size we can get numerically is $L_x \times L_y = 6 \times 4$ with $N = 8$ particles. Since the system has a discrete translation symmetry, the total lattice momentum is conserved, and we block diagonalize the Hamiltonian for each total momentum sector. In Fig. E.3a) we show the lowest eigenvalues for the Haldane model with parameters adapted from Ref. [111]. As expected for a $\nu = 1/3$ FQAH state, the ground state is threefold degenerate, and a clear gap to the first excited states is visible. It was argued in Refs. [104, 111] that the gap survives in the thermodynamic limit. Under the insertion of flux, which can be achieved by shifting the single-particle momentum $k_i \to k_i + \phi/L_i$, the three ground states flow into each other, while the gap to the excited states remains for all ϕ. These are clear signatures of a $\nu = 1/3$ FAQH state. We compare the projected spectral function $\bar{A}(\mathbf{k}, \omega)$ and the density of states calculated using exact diagonalization with the corresponding results from the parton ansatz in Fig. E.3b). Qualitatively, the two approaches agree excellently, supporting the parton description of the FQAH state.

Bibliography

[1] F. Pichler, W. Kadow, C. Kuhlenkamp, and M. Knap, “Probing magnetism in moiré heterostructures with quantum twisting microscopes”, arXiv:2402.04311 (2024).

[2] E. C. Regan, D. Wang, C. Jin, M. I. Bakti Utama, B. Gao, X. Wei, S. Zhao, W. Zhao, Z. Zhang, K. Yumigeta, M. Blei, J. D. Carlström, K. Watanabe, T. Taniguchi, S. Tongay, M. Crommie, A. Zettl, and F. Wang, “Mott and generalized Wigner crystal states in WSe_2/WS_2 moiré superlattices”, Nature **579**, 359–363 (2020).

[3] Y. Shimazaki, I. Schwartz, K. Watanabe, T. Taniguchi, M. Kroner, and A. Imamoğlu, “Strongly correlated electrons and hybrid excitons in a moiré heterostructure”, Nature **580**, 472–477 (2020).

[4] L. Wang, E.-M. Shih, A. Ghiotto, L. Xian, D. A. Rhodes, C. Tan, M. Claassen, D. M. Kennes, Y. Bai, B. Kim, K. Watanabe, T. Taniguchi, X. Zhu, J. Hone, A. Rubio, A. N. Pasupathy, and C. R. Dean, “Correlated electronic phases in twisted bilayer transition metal dichalcogenides”, Nat. Mater. **19**, 861–866 (2020).

[5] Y. Xu, S. Liu, D. A. Rhodes, K. Watanabe, T. Taniguchi, J. Hone, V. Elser, K. F. Mak, and J. Shan, “Correlated insulating states at fractional fillings of moiré superlattices”, Nature **587**, 214–218 (2020).

[6] X. Huang, T. Wang, S. Miao, C. Wang, Z. Li, Z. Lian, T. Taniguchi, K. Watanabe, S. Okamoto, D. Xiao, S.-F. Shi, and Y.-T. Cui, “Correlated insulating states at fractional fillings of the WSe_2/WS_2 moiré lattice”, Nat. Phys. **17**, 715–719 (2021).

[7] C. Jin, Z. Tao, T. Li, Y. Xu, Y. Tang, J. Zhu, S. Liu, K. Watanabe, T. Taniguchi, J. C. Hone, L. Fu, J. Shan, and K. F. Mak, “Stripe phases in WSe_2/WS_2 moiré superlattices”, Nat. Mater. **20**, 940–944 (2021).

[8] H. Li, S. Li, E. C. Regan, D. Wang, W. Zhao, S. Kahn, K. Yumigeta, M. Blei, T. Taniguchi, K. Watanabe, S. Tongay, A. Zettl, M. F. Crommie, and F. Wang, “Imaging two-dimensional generalized Wigner crystals”, Nature **597**, 650–654 (2021).

[9] Y. Tang, K. Su, L. Li, Y. Xu, S. Liu, K. Watanabe, T. Taniguchi, J. Hone, C.-M. Jian, C. Xu, K. F. Mak, and J. Shan, “Evidence of frustrated magnetic interactions in a Wigner–Mott insulator”, Nat. Nanotechnol. **18**, 233–237 (2023).

[10] T. Li, S. Jiang, B. Shen, Y. Zhang, L. Li, Z. Tao, T. Devakul, K. Watanabe, T. Taniguchi, L. Fu, J. Shan, and K. F. Mak, “Quantum anomalous Hall effect from intertwined moiré bands”, Nature **600**, 641–646 (2021).

[11] J. Cai, E. Anderson, C. Wang, X. Zhang, X. Liu, W. Holtzmann, Y. Zhang, F. Fan, T. Taniguchi, K. Watanabe, Y. Ran, T. Cao, L. Fu, D. Xiao, W. Yao, and X. Xu, “Signatures of fractional quantum anomalous Hall states in twisted MoTe2”, Nature **622**, 63–68 (2023).

[12] Y. Zeng, Z. Xia, K. Kang, J. Zhu, P. Knüppel, C. Vaswani, K. Watanabe, T. Taniguchi, K. F. Mak, and J. Shan, “Thermodynamic evidence of fractional Chern insulator in moiré $MoTe_2$”, Nature **622**, 69–73 (2023).

[13]H. Park, J. Cai, E. Anderson, Y. Zhang, J. Zhu, X. Liu, C. Wang, W. Holtzmann, C. Hu, Z. Liu, T. Taniguchi, K. Watanabe, J.-H. Chu, T. Cao, L. Fu, W. Yao, C.-Z. Chang, D. Cobden, D. Xiao, and X. Xu, "Observation of fractionally quantized anomalous Hall effect", Nature **622**, 74–79 (2023).

[14]F. Xu, Z. Sun, T. Jia, C. Liu, C. Xu, C. Li, Y. Gu, K. Watanabe, T. Taniguchi, B. Tong, J. Jia, Z. Shi, S. Jiang, Y. Zhang, X. Liu, and T. Li, "Observation of Integer and Fractional Quantum Anomalous Hall Effects in Twisted Bilayer $MoTe_2$", Physical Review X **13**, 031037 (2023).

[15]B. A. Foutty, C. R. Kometter, T. Devakul, A. P. Reddy, K. Watanabe, T. Taniguchi, L. Fu, and B. E. Feldman, "Mapping twist-tuned multi-band topology in bilayer WSe_2", arXiv:2304.09808 (2023).

[16]W. Zhao, K. Kang, Y. Zhang, P. Knüppel, Z. Tao, L. Li, C. L. Tschirhart, E. Redekop, K. Watanabe, T. Taniguchi, A. F. Young, J. Shan, and K. F. Mak, "Realization of the Haldane Chern insulator in a moiré lattice", Nature Physics **20**, 275–280 (2024).

[17]Z. Tao, B. Shen, S. Jiang, T. Li, L. Li, L. Ma, W. Zhao, J. Hu, K. Pistunova, K. Watanabe, T. Taniguchi, T. F. Heinz, K. F. Mak, and J. Shan, "Valley-Coherent Quantum Anomalous Hall State in AB-Stacked $MoTe_2/WSe_2$ Bilayers", Physical Review X **14**, 011004 (2024).

[18]F. Wu, T. Lovorn, E. Tutuc, and A. H. MacDonald, "Hubbard model physics in transition metal dichalcogenide moiré bands", Phys. Rev. Lett. **121**, 026402 (2018).

[19]F. Wu, T. Lovorn, E. Tutuc, I. Martin, and A. H. MacDonald, "Topological insulators in twisted transition metal dichalcogenide homobilayers", Phys. Rev. Lett. **122**, 086402 (2019).

[20]Y. Tang, L. Li, T. Li, Y. Xu, S. Liu, K. Barmak, K. Watanabe, T. Taniguchi, A. H. MacDonald, J. Shan, and K. F. Mak, "Simulation of hubbard model physics in $WSe_2/WS2_2$ moiré superlattices", Nature **579**, 353–358 (2020).

[21]H. Pan, F. Wu, and S. D. Sarma, "Band topology, Hubbard model, Heisenberg model, and Dzyaloshinskii-Moriya interaction in twisted bilayer WSe_2", Phys. Rev. Research **2**, 033087 (2020).

[22]H. Pan, F. Wu, and S. D. Sarma, "Quantum Phase Diagram of a Moiré-Hubbard Model", Phys. Rev. B **102**, 201104(R) (2020).

[23]T. Devakul, V. Crépel, Y. Zhang, and L. Fu, "Magic in twisted transition metal dichalcogenide bilayers", Nature Communications **12**, 6730 (2021).

[24]V. Crépel and A. Millis, "Bridging the small and large in twisted transition metal dicalcogenide homobilayers: a tight binding model capturing orbital interference and topology across a wide range of twist angles", arXiv:2403.15546 (2024).

[25]N. Morales-Durán, N. C. Hu, P. Potasz, and A. H. MacDonald, "Non-local interactions in moiré Hubbard systems", Phys. Rev. Lett. **128**, 217202 (2022).

[26]M. Roger, "Multiple exchange in ^{3}He and in the Wigner solid", Physical Review B **30**, 6432–6457 (1984).

[27]B. Tanatar and D. M. Ceperley, "Ground state of the two-dimensional electron gas", Physical Review B **39**, 5005–5016 (1989).

[28]X. Zhu and S. G. Louie, "Variational quantum Monte Carlo study of two-dimensional Wigner crystals: Exchange, correlation, and magnetic-field effects", Physical Review B **52**, 5863–5884 (1995).

[29]N. C. Hu and A. H. MacDonald, "Competing magnetic states in transition metal dichalcogenide moiré materials", Phys. Rev. B **104**, 214403 (2021).

[30]K.-S. Kim, C. Murthy, A. Pandey, and S. A. Kivelson, "Interstitial-Induced Ferromagnetism in a Two-Dimensional Wigner Crystal", Physical Review Letters **129**, 227202 (2022).

[31]N. Morales-Durán, P. Potasz, and A. H. MacDonald, "Magnetism and Quantum Melting in Moiré-Material Wigner Crystals", Phys. Rev. B **107**, 235131 (2023).

[32]L. Ciorciaro, T. Smolenski, I. Morera, N. Kiper, S. Hiestand, M. Kroner, Y. Zhang, K. Watanabe, T. Taniguchi, E. Demler, and A. Imamoglu, "Kinetic Magnetism in Triangular Moiré Materials", Nature **623**, 509–513 (2023).

[33]D. J. Thouless, M. Kohmoto, M. P. Nightingale, and M. den Nijs, "Quantized hall conductance in a two-dimensional periodic potential", Phys. Rev. Lett. **49**, 405–408 (1982).

[34]H. Li, U. Kumar, K. Sun, and S.-Z. Lin, "Spontaneous fractional Chern insulators in transition metal dichalcogenide moiré superlattices", Physical Review Research **3**, L032070 (2021).

[35]A. P. Reddy, F. F. Alsallom, Y. Zhang, T. Devakul, and L. Fu, "Fractional quantum anomalous Hall states in twisted bilayer MoTe_2 and WSe_2", Physical Review B **108**, 085117 (2023).

[36]V. Crépel and L. Fu, "Anomalous Hall metal and fractional Chern insulator in twisted transition metal dichalcogenides", Physical Review B **107**, L201109 (2023).

[37]W.-X. Qiu, B. Li, X.-J. Luo, and F. Wu, "Interaction-Driven Topological Phase Diagram of Twisted Bilayer MoTe_2", Physical Review X **13**, 041026 (2023).

[38]J. Dong, J. Wang, P. J. Ledwith, A. Vishwanath, and D. E. Parker, "Composite Fermi Liquid at Zero Magnetic Field in Twisted MoTe_2", Physical Review Letters **131**, 136502 (2023).

[39]H. Goldman, A. P. Reddy, N. Paul, and L. Fu, "Zero-field composite Fermi liquid in twisted semiconductor bilayers", Physical Review Letters **131**, 136501 (2023).

[40]J. Yu, J. Herzog-Arbeitman, M. Wang, O. Vafek, B. A. Bernevig, and N. Regnault, "Fractional Chern insulators versus nonmagnetic states in twisted bilayer MoTe_2", Physical Review B **109**, 045147 (2024).

[41]N. Morales-Durán, N. Wei, J. Shi, and A. H. MacDonald, "Magic Angles and Fractional Chern Insulators in Twisted Homobilayer TMDs", arXiv:2308.03143 (2023).

[42]E. M. Spanton, A. A. Zibrov, H. Zhou, T. Taniguchi, K. Watanabe, M. P. Zaletel, and A. F. Young, "Observation of fractional Chern insulators in a van der Waals heterostructure", Science **360**, 62–66 (2018).

[43]Y. Xie, A. T. Pierce, J. M. Park, D. E. Parker, E. Khalaf, P. Ledwith, Y. Cao, S. H. Lee, S. Chen, P. R. Forrester, K. Watanabe, T. Taniguchi, A. Vishwanath, P. Jarillo-Herrero, and A. Yacoby, "Fractional Chern insulators in magic-angle twisted bilayer graphene", Nature **600**, 439–443 (2021).

[44]J. Dong, T. Wang, T. Wang, T. Soejima, M. P. Zaletel, A. Vishwanath, and D. E. Parker, "Anomalous Hall Crystals in Rhombohedral Multilayer Graphene I: Interaction-Driven Chern Bands and Fractional Quantum Hall States at Zero Magnetic Field", arXiv:2311.05568 (2023).

[45]Z. Lu, T. Han, Y. Yao, A. P. Reddy, J. Yang, J. Seo, K. Watanabe, T. Taniguchi, L. Fu, and L. Ju, "Fractional quantum anomalous Hall effect in multilayer graphene", Nature **626**, 759–764 (2024).

[46] K. Kang, B. Shen, Y. Qiu, K. Watanabe, T. Taniguchi, J. Shan, and K. F. Mak, "Observation of the fractional quantum spin Hall effect in moiré $MoTe_2$", arXiv:2402.03294 (2024).

[47] K. Kang, Y. Qiu, K. Watanabe, T. Taniguchi, J. Shan, and K. F. Mak, "Observation of the double quantum spin Hall phase in moiré WSe_2", arXiv:2402.04196 (2024).

[48] Y.-H. Zhang, "Non-Abelian and Abelian descendants of vortex spin liquid: fractional quantum spin Hall effect in twisted $MoTe_2$", arXiv:2403.12126 (2024).

[49] I. S. Villadiego, "Halperin States of Particles and Holes in Ideal Time Reversal Invariant Pairs of Chern Bands and The Fractional Quantum Spin Hall Effect in Moiré $MoTe_2$", arXiv:2403.12185 (2024).

[50] A. G. Salvador, C. Kuhlenkamp, L. Ciorciaro, M. Knap, and A. İmamoğlu, "Optical signatures of periodic magnetization: the moiré Zeeman effect", Phys. Rev. Lett. **128**, 237401 (2022).

[51] A. Julku, S. Ding, and G. M. Bruun, "An exciton interacting with a moire lattice – polarons, strings, and optical probing of spin correlations", arXiv:2311.03482 (2023).

[52] Y. Shimazaki, C. Kuhlenkamp, I. Schwartz, T. Smoleński, K. Watanabe, T. Taniguchi, M. Kroner, R. Schmidt, M. Knap, and A. Imamoğlu, "Optical Signatures of Periodic Charge Distribution in a Mott-like Correlated Insulator State", Phys. Rev. X **11**, 021027 (2021).

[53] T. Smoleński, P. E. Dolgirev, C. Kuhlenkamp, A. Popert, Y. Shimazaki, P. Back, M. Kroner, K. Watanabe, T. Taniguchi, I. Esterlis, E. Demler, and A. Imamoğlu, "Observation of Wigner crystal of electrons in a monolayer semiconductor", Nature **595**, 53–57 (2021).

[54] S. Chatterjee, J. F. Rodriguez-Nieva, and E. Demler, "Diagnosing phases of magnetic insulators via noise magnetometry with spin qubits", Phys. Rev. B **99**, 104425 (2019).

[55] J. Feldmeier, W. Natori, M. Knap, and J. Knolle, "Local Probes for Charge-Neutral Edge States in Two-Dimensional Quantum Magnets", Phys. Rev. B **102**, 134423 (2020).

[56] E. J. König, M. T. Randeria, and B. Jäck, "Tunneling Spectroscopy of Quantum Spin Liquids", Phys. Rev. Lett. **125**, 267206 (2020).

[57] A. Inbar, J. Birkbeck, J. Xiao, T. Taniguchi, K. Watanabe, B. Yan, Y. Oreg, A. Stern, E. Berg, and S. Ilani, "The quantum twisting microscope", Nature **614**, 682–687 (2023).

[58] V. Peri, S. Ilani, P. A. Lee, and G. Refael, "Probing quantum spin liquids with a quantum twisting microscope", Phys. Rev. B **109**, 035127 (2024).

[59] M. Carrega, I. J. Vera-Marun, and A. Principi, "Tunneling spectroscopy as a probe of fractionalization in 2D magnetic heterostructures", Phys. Rev. B **102**, 085412 (2020).

[60] D. Xiao, G.-B. Liu, W. Feng, X. Xu, and W. Yao, "Coupled spin and valley physics in monolayers of MoS_2 and other group-VI dichalcogenides", Phys. Rev. Lett. **108**, 196802 (2012).

[61] L. Rademaker, "Spin-orbit coupling in transition metal dichalcogenide heterobilayer flat bands", Physical Review B **105**, 195428 (2022).

[62] R. Bistritzer and A. H. MacDonald, “Moire bands in twisted double-layer graphene”, Proc. Natl. Acad. Sci. U.S.A. **108**, 12233–12237 (2011).

[63] G. D. Mahan, “Dc Conductivities”, in *Many-Particle Physics*, edited by G. D. Mahan, Physics of Solids and Liquids (Springer US, Boston, MA, 2000), pp. 499–577.

[64] J. Fernández-Rossier, “Theory of Single-Spin Inelastic Tunneling Spectroscopy”, Phys. Rev. Lett. **102**, 256802 (2009).

[65] J. Fransson, O. Eriksson, and A. V. Balatsky, “Theory of spin-polarized scanning tunneling microscopy applied to local spins”, Phys. Rev. B **81**, 115454 (2010).

[66] R. Bistritzer and A. H. MacDonald, “Transport Between Twisted Graphene Layers”, Phys. Rev. B **81**, 245412 (2010).

[67] H. Watanabe and M. Ogata, “Charge order and superconductivity in a two-dimensional triangular lattice at n=2/3”, J. Phys. Soc. Jpn. **74**, 2901–2904 (2005).

[68] L. F. Tocchio, C. Gros, X.-F. Zhang, and S. Eggert, “Phase diagram of the triangular extended Hubbard model”, Phys. Rev. Lett. **113**, 246405 (2014).

[69] B. Padhi, R. Chitra, and P. W. Phillips, “Generalized Wigner crystallization in moiré materials”, Phys. Rev. B **103**, 125146 (2021).

[70] J. Zang, J. Wang, J. Cano, and A. J. Millis, “Hartree-Fock study of the moiré Hubbard model for twisted bilayer transition metal dichalcogenides”, Phys. Rev. B **104**, 075150 (2021).

[71] M. Qin, “Effect of hole doping on the 120 degree order in the triangular lattice Hubbard model: A Hartree-Fock revisit”, J. Phys.: Condens. Matter **34**, 235603 (2022).

[72] N. Morales-Durán, A. H. MacDonald, and P. Potasz, “Metal-insulator transition in transition metal dichalcogenide heterobilayer moiré superlattices”, Phys. Rev. B **103**, L241110 (2021).

[73] W. Kadow, L. Vanderstraeten, and M. Knap, “Hole Spectral Function of a Chiral Spin Liquid in the Triangular Lattice Hubbard Model”, Phys. Rev. B **106**, 094417 (2022).

[74] A. Singh and Z. Tešanović, “Quantum spin fluctuations in an itinerant antiferromagnet”, Phys. Rev. B **41**, 11457–11465 (1990).

[75] A. Singh, “Finite-U induced competing interactions, frustration, and quantum phase transition in a triangular-lattice antiferromagnet”, Phys. Rev. B **71**, 214406 (2005).

[76] J. Knolle, I. Eremin, A. V. Chubukov, and R. Moessner, “Theory of itinerant magnetic excitations in the spin-density-wave phase of iron-based superconductors”, Phys. Rev. B **81**, 140506(R) (2010).

[77] J. Willsher, H.-K. Jin, and J. Knolle, “Magnetic excitations, phase diagram and order-by-disorder in the extended triangular-lattice Hubbard model”, Phys. Rev. B **107**, 064425 (2023).

[78] M. Mourigal, W. T. Fuhrman, A. L. Chernyshev, and M. E. Zhitomirsky, “Dynamical structure factor of the triangular-lattice antiferromagnet”, Phys. Rev. B **88**, 094407 (2013).

[79] A. L. Chernyshev and M. E. Zhitomirsky, “Magnon Decay in Noncollinear Quantum Antiferromagnets”, Phys. Rev. Lett. **97**, 207202 (2006).

[80] A. L. Chernyshev and M. E. Zhitomirsky, “Spin waves in a triangular lattice antiferromagnet: Decays, spectrum renormalization, and singularities”, Phys. Rev. B **79**, 144416 (2009).

[81] S. S. Pershoguba, S. Banerjee, J. Lashley, J. Park, H. Ågren, G. Aeppli, and A. V. Balatsky, “Dirac Magnons in Honeycomb Ferromagnets”, Phys. Rev. X **8**, 011010 (2018).

[82] A. Szasz, J. Motruk, M. P. Zaletel, and J. E. Moore, “Chiral Spin Liquid Phase of the Triangular Lattice Hubbard Model: A Density Matrix Renormalization Group Study”, Phys. Rev. X **10**, 021042 (2020).

[83] T. Cookmeyer, J. Motruk, and J. E. Moore, “Four-Spin Terms and the Origin of the Chiral Spin Liquid in Mott Insulators on the Triangular Lattice”, Phys. Rev. Lett. **127**, 087201 (2021).

[84] V. Kalmeyer and R. B. Laughlin, “Equivalence of the resonating-valence-bond and fractional quantum Hall states”, Phys. Rev. Lett. **59**, 2095–2098 (1987).

[85] B.-B. Chen, Z. Chen, S.-S. Gong, D. N. Sheng, W. Li, and A. Weichselbaum, “Quantum spin liquid with emergent chiral order in the triangular-lattice Hubbard model”, Phys. Rev. B **106**, 094420 (2022).

[86] C. Kuhlenkamp, W. Kadow, A. Imamoglu, and M. Knap, “Tunable topological order of pseudo spins in semiconductor heterostructures”, arXiv:2209.05506 (2022).

[87] T. Senthil, “Theory of a continuous Mott transition in two dimensions”, Phys. Rev. B **78**, 045109 (2008).

[88] X.-Y. Song, C. Wang, A. Vishwanath, and Y.-C. He, “Unifying description of competing orders in two-dimensional quantum magnets”, Nat Commun **10**, 4254 (2019).

[89] X.-Y. Song, A. Vishwanath, and Y.-H. Zhang, “Doping the chiral spin liquid: Topological superconductor or chiral metal”, Phys. Rev. B **103**, 165138 (2021).

[90] E. A. Ghioldi, M. G. Gonzalez, S.-S. Zhang, Y. Kamiya, L. O. Manuel, A. E. Trumper, and C. D. Batista, “Dynamical structure factor of the triangular antiferromagnet: Schwinger boson theory beyond mean field”, Phys. Rev. B **98**, 184403 (2018).

[91] S.-S. Zhang, E. A. Ghioldi, Y. Kamiya, L. O. Manuel, A. E. Trumper, and C. D. Batista, “Large-S limit of the large-N theory for the triangular antiferromagnet”, Phys. Rev. B **100**, 104431 (2019).

[92] C. Zhang and T. Li, “Resonating valence bond theory of anomalous spin dynamics of spin-$\frac{1}{2}$ triangular lattice Heisenberg antiferromagnet and its application to $Ba_3CoSb_2O_9$”, Phys. Rev. B **102**, 075108 (2020).

[93] A. O. Scheie, E. A. Ghioldi, J. Xing, J. a. M. Paddison, N. E. Sherman, M. Dupont, L. D. Sanjeewa, S. Lee, A. J. Woods, D. Abernathy, D. M. Pajerowski, T. J. Williams, S.-S. Zhang, L. O. Manuel, A. E. Trumper, C. D. Pemmaraju, A. S. Sefat, D. S. Parker, T. P. Devereaux, R. Movshovich, J. E. Moore, C. D. Batista, and D. A. Tennant, “Proximate spin liquid and fractionalization in the triangular antiferromagnet $KYbSe_2$”, Nat. Phys. **20**, 74–81 (2024).

[94] F. Ferrari and F. Becca, “Dynamical Structure Factor of the $J_1 - J_2$ Heisenberg Model on the Triangular Lattice: Magnons, Spinons, and Gauge Fields”, Phys. Rev. X **9**, 031026 (2019).

[95] T. Li, S. Jiang, L. Li, Y. Zhang, K. Kang, J. Zhu, K. Watanabe, T. Taniguchi, D. Chowdhury, L. Fu, J. Shan, and K. F. Mak, “Continuous Mott transition in semiconductor moiré superlattices”, Nature **597**, 350–354 (2021).

[96] A. Ghiotto, E.-M. Shih, G. S. S. G. Pereira, D. A. Rhodes, B. Kim, J. Zang, A. J. Millis, K. Watanabe, T. Taniguchi, J. C. Hone, L. Wang, C. R. Dean, and A. N. Pasupathy, "Quantum criticality in twisted transition metal dichalcogenides", Nature **597**, 345–349 (2021).

[97] M. O. Goerbig, "Electronic Properties of Graphene in a Strong Magnetic Field", Reviews of Modern Physics **83**, 1193–1243 (2011).

[98] M. T. Greenaway, E. E. Vdovin, A. Mishchenko, O. Makarovsky, A. Patanè, J. R. Wallbank, Y. Cao, A. V. Kretinin, M. J. Zhu, S. V. Morozov, V. I. Fal′ko, K. S. Novoselov, A. K. Geim, T. M. Fromhold, and L. Eaves, "Resonant tunnelling between the chiral Landau states of twisted graphene lattices", Nature Physics **11**, 1057–1062 (2015).

[99] F. D. M. Haldane, "Model for a quantum hall effect without landau levels: condensed-matter realization of the "parity anomaly"", Phys. Rev. Lett. **61**, 2015–2018 (1988).

[100] K. Zakeri, "Elementary spin excitations in ultrathin itinerant magnets", Physics Reports, Elementary Spin Excitations in Ultrathin Itinerant Magnets **545**, 47–93 (2014).

[101] R. L. Doretto, A. O. Caldeira, and S. M. Girvin, "Lowest Landau level bosonization", Physical Review B **71**, 045339 (2005).

[102] R. L. Doretto and M. O. Goerbig, "Flat-band ferromagnetism and spin waves in topological Hubbard models", Physical Review B **92**, 245124 (2015).

[103] L. S. G. Leite and R. L. Doretto, "Flat-band ferromagnetism and spin waves in the Haldane-Hubbard model", Physical Review B **104**, 155129 (2021).

[104] N. Regnault and B. A. Bernevig, "Fractional Chern Insulator", Physical Review X **1**, 021014 (2011).

[105] D. N. Sheng, Z.-C. Gu, K. Sun, and L. Sheng, "Fractional quantum Hall effect in the absence of Landau levels", Nature Communications **2**, 389 (2011).

[106] Y.-M. Lu and Y. Ran, "Symmetry-protected fractional Chern insulators and fractional topological insulators", Physical Review B **85**, 165134 (2012).

[107] J. McGreevy, B. Swingle, and K.-A. Tran, "Wave functions for fractional Chern insulators", Physical Review B **85**, 125105 (2012).

[108] M. Gattu, G. J. Sreejith, and J. K. Jain, "STM in the fractional quantum Hall effect: Spectroscopy of composite-fermion bound states", arXiv:2312.07114 (2023).

[109] S. Pu, A. C. Balram, Y. Hu, Y.-C. Tsui, M. He, N. Regnault, M. P. Zaletel, A. Yazdani, and Z. Papić, "Fingerprints of Composite Fermion Lambda Levels in Scanning Tunneling Microscopy", arXiv:2312.06779 (2023).

[110] Y. Hu, Y.-C. Tsui, M. He, U. Kamber, T. Wang, K. Watanabe, T. Taniguchi, Z. Papic, and M. P. Zaletel, "High-Resolution Tunneling Spectroscopy of Fractional Quantum Hall States", arXiv:2308.05789, `10.48550/arXiv.2308.05789` (2024).

[111] Y.-L. Wu, B. A. Bernevig, and N. Regnault, "Zoology of fractional Chern insulators", Physical Review B **85**, 075116 (2012).

[112] Y. Zhou, J. Sung, E. Brutschea, I. Esterlis, Y. Wang, G. Scuri, R. J. Gelly, H. Heo, T. Taniguchi, K. Watanabe, G. Zaránd, M. D. Lukin, P. Kim, E. Demler, and H. Park, "Bilayer Wigner crystals in a transition metal dichalcogenide heterostructure", Nature **595**, 48–52 (2021).

[113] B. Spivak, S. V. Kravchenko, S. A. Kivelson, and X. P. A. Gao, "Colloquium: Transport in strongly correlated two dimensional electron fluids", Rev. Mod. Phys. **82**, 1743–1766 (2010).

[114] B. Spivak and S. Kivelson, "Intermediate phases of the two dimensional electron fluid between the Fermi liquid and the Wigner crystal", arXiv:2310.10720 (2004).

[115] J. Sung, J. Wang, I. Esterlis, P. A. Volkov, G. Scuri, Y. Zhou, E. Brutschea, T. Taniguchi, K. Watanabe, Y. Yang, M. A. Morales, S. Zhang, A. J. Millis, M. D. Lukin, P. Kim, E. Demler, and H. Park, "Observation of an electronic microemulsion phase emerging from a quantum crystal-to-liquid transition", arXiv:2310.10720 (2023).

[116] Y. Cao, V. Fatemi, S. Fang, K. Watanabe, T. Taniguchi, E. Kaxiras, and P. Jarillo-Herrero, "Unconventional superconductivity in magic-angle graphene superlattices", Nature **556**, 43–50 (2018).

[117] X. Lu, P. Stepanov, W. Yang, M. Xie, M. A. Aamir, I. Das, C. Urgell, K. Watanabe, T. Taniguchi, G. Zhang, A. Bachtold, A. H. MacDonald, and D. K. Efetov, "Superconductors, orbital magnets and correlated states in magic-angle bilayer graphene", Nature **574**, 653–657 (2019).

[118] H. Zhou, L. Holleis, Y. Saito, L. Cohen, W. Huynh, C. L. Patterson, F. Yang, T. Taniguchi, K. Watanabe, and A. F. Young, "Isospin magnetism and spin-polarized superconductivity in Bernal bilayer graphene", Science **375**, 774–778 (2022).

[119] C. Zerba, C. Kuhlenkamp, A. Imamoğlu, and M. Knap, "Realizing Topological Superconductivity in Tunable Bose-Fermi Mixtures with Transition Metal Dichalcogenide Heterostructures", arXiv:2310.10720 (2023).

[120] K. P. Nuckolls, R. L. Lee, M. Oh, D. Wong, T. Soejima, J. P. Hong, D. Călugăru, J. Herzog-Arbeitman, B. A. Bernevig, K. Watanabe, T. Taniguchi, N. Regnault, M. P. Zaletel, and A. Yazdani, "Quantum textures of the many-body wavefunctions in magic-angle graphene", Nature **620**, 525–532 (2023).

[121] Z. Papić, R. S. K. Mong, A. Yazdani, and M. P. Zaletel, "Imaging Anyons with Scanning Tunneling Microscopy", Physical Review X **8**, 011037 (2018).

[122] M. Abramowitz and I. Stegun, "Handbook of Mathematical Functions with Formulas, Graphs, and Mathematical Tables", in (United States Department of Commerce, National Bureau of Standards, 1964) Chap. 13. Confluent Hypergeometric Functions, p. 504.

[123] K. Sun, Z. Gu, H. Katsura, and S. Das Sarma, "Nearly Flatbands with Nontrivial Topology", Physical Review Letters **106**, 236803 (2011).

[124] Y.-F. Wang, H. Yao, C.-D. Gong, and D. N. Sheng, "Fractional quantum Hall effect in topological flat bands with Chern number two", Physical Review B **86**, 201101 (2012).